ADVANCES IN EXPERIMENTAL METHODS FOR CHARACTERISATION OF POROUS SOLIDS

Karen Shu San Manley

A dissertation submitted to Imperial College London

in fulfilment of the requirements for the degree of

Doctor of Philosophy

and the Diploma of Membership of Imperial College London

Department of Chemical Engineering

Imperial College London

November 2009

ABSTRACT

This thesis describes work on the development of new integrated methods for the characterisation of porous media. Porous media are of wide importance in a variety of applications including oil and gas production, tissue engineering, filtration and separation and ground water hydrology. Such porous media are characterised by the fraction of their volume occupied by pores (the *porosity*) and by parameters characterising the ease of flow and diffusion through the medium (the *permeability* and the *diffusivity*). However, the flow processes are very complex, reflecting the complex nature of the pore structure.

The objective of the work described in this thesis was to develop and apply two new integrated pieces of apparatus which were aimed at elucidating several aspects of the complex flow processes. The first integrated apparatus was aimed at the study of gaseous transport and the second at the study of mercury penetration, flow and electrical conduction, in the pores of selected media. Thin-section imaging was also applied to obtain supplementary information.

The integrated gaseous transport apparatus was designed not only to measure permeability (by the pressure rise technique), but also to study both steady state and (importantly) transient diffusion of oxygen in nitrogen in the pores of the selected media. The system was capable of operating with media with a wide range of permeabilities and yielded accurate values of the viscous permeability and the slip flow coefficient. In addition, experiments

were carried out in the partially turbulent flow region. The diffusion measurements yielded information on the ratio (r_D) of the diffusion coefficient in the media to that in free space; this ratio is also a specific property of the medium. Combining the steady state and transient diffusion measurements, it was possible to deduce the effective porosity and the pore length.

The second integrated apparatus was for the study of porous media subjected to mercury penetration under pressure. This apparatus allowed conventional *mercury porosimetry* measurements to be performed (i.e. measurements of the pore volume occupied as a function of pore size penetrated) but, crucially, it also allowed measurements of the permeability to mercury and of the conductivity with mercury to be made simultaneously. The permeability to mercury approaches the gaseous value when complete saturation of the medium is achieved; however the manner in which mercury permeability varies with pore size gives a striking indication of the role of the various pores in the flow process. In the conductivity experiments, the ratio (r_{Cp}) of the conductivity of the medium penetrated with mercury at pressure p to the conductivity of pure mercury is determined as a function of p. At high penetration pressures, the value of r_{Cp} approaches that of r_D reflecting the analogy between conduction and diffusion when the medium is saturated with mercury. However, the variation of r_{Cp} with pore size penetrated gives a remarkable indication of the significance of the pores in given size ranges in the diffusion process (analogous to the information yielded by the mercury permeability measurements relating to the overall permeability).

CONTENTS

ABSTRACT ..... **I**

LIST OF FIGURES AND TABLES ..... **IX**

NOMENCLATURE ..... **XVI**

ACKNOWLEDGEMENTS ..... **XIX**

1 INTRODUCTION **1**

1.1 POROUS SOLIDS 1

1.2 PROJECT AIM 8

1.3 THESIS STRUCTURE 9

2 BACKGROUND **11**

2.1 CHARACTERISATION OF POROUS SOLIDS 11

2.1.1 Total porosity 12

2.1.2 Pore size distribution 13

2.1.3 Liquid permeability 14

2.1.4 Relative permeability 18

2.1.5 Structural analysis and permeability predictions from stereological image analysis 19

2.1.6 X-ray tomography 22

2.1.7 Electron microscopy for imaging porous solids 23

2.1.8 Liquid metal penetration and solidification 24

2.2 GASEOUS TRANSPORT IN POROUS SOLIDS 25

2.2.1 Background to gaseous transport in porous media 25

2.2.2 Investigation of turbulent flow through porous media 29

2.2.3 Steady-state diffusion through porous solids 30

2.2.4 Transient diffusion through porous solids 34

2.2.5 Measurement of gas permeability 34

2.2.6 Diffusion measurements 39

2.3 MERCURY PENETRATION OF POROUS SOLIDS 40

2.3.1 Mercury porosimetry 41

2.3.2 Mercury permeability 44

2.3.3 Mercury conductivity 48

2.3.4 Mercury penetration techniques: Overall assessment 51

3 DEVELOPMENT OF AN INTEGTRATED APPARATUS FOR GAS PERMEABILITY AND DIFFUSION MEASUREMENTS 53

3.1 PREPARATION OF SAMPLES 54

3.2 PROTOTYPE APPARATUS FOR THE MEASUREMENT OF GAS PERMEABILITY - DESIGN DETAIL 56

3.2.1 Preliminary results of permeability measurements with the prototype apparatus 60

3.3 INTEGRATED APPARATUS FOR THE MEASUREMENT OF GAS PERMEABILITY AND DIFFUSIVITY – DESIGN DETAIL 64

3.3.1 Set-up for permeability measurements 66

3.3.2 Diffusivity set-up and measurements 68

3.3.3 Steady state diffusion of oxygen through nitrogen filled pores 69

3.3.4 Transient diffusion of oxygen through nitrogen filled pores. 71

3.4 OVERVIEW 72

4 DEVELOPMENT OF AN INTEGTRATED APPARATUS FOR MERCURY PENETRATION PERMEABILITY AND CONDUCTANCE 73

4.1 INTRODUCTION TO THE MERCURY INTEGRATED METHOD 74

4.1.1 The mercury porosimetry technique 76

4.1.2 The mercury permeability measurement technique 78

4.1.3 Electrical conductivity measurements of mercury in the pores of a porous solid 78

4.2 INTEGRATED MERCURY APPARATUS DESCRIPTION AND OPERATION 80

4.2.1 Design description 80

4.2.2 Preparation of samples 82

4.2.3 Mercury intrusion porosimetry (MIP) 83

4.2.4 Mercury permeability distribution and total permeability 85

4.2.5 Electrical conductivity of mercury in the pores of a porous solid 91

4.3 OVERVIEW 93

5 APPLICATION OF INTEGRATED METHODS TO THE STUDY OF POROUS MATERIALS 94

I: POROUS SANDSTONES 94

5.1 MATERIALS 95

5.1.1 Berea sandstone sample details 95

5.2 PERMEABILITY OF SANDSTONE - RESULTS 97
5.2.1 Sandstone permeability - data reproducibility 97
5.2.2 Viscous permeability (k) and slip flow coefficients (K_0) of sandstone samples 98
5.2.3 Investigation of permeability at low mean pressures 101
5.2.4 Results for turbulent flows 102
5.3 DIFFUSIVITY OF SANDSTONE – RESULTS 105
5.3.1 Diffusivity of oxygen through nitrogen filled sandstone samples - data reproducibility 105
5.3.2 Steady state and transient gas diffusivity of sandstone samples 108
5.4 PORE SIZE DISTRIBUTION, PERMEABILITY AND ELECTRICAL CONDUCTIVITY MEASUREMENTS 110
5.5 IMAGE ANALYSIS OF THIN-SECTIONS OF SANDSTONE SAMPLES 123
5.5.1 Structural interpretation of porous solids 123
5.6 DISCUSSION OF THE RESULTS OBTAINED USING THE INTEGRATED METHODS AND IMAGE ANALYSIS 125
5.6.1 Permeability results 125
5.6.2 K_0 the slip coefficient 127
5.6.3 Turbulent effects on gas permeability 128
5.6.4 Permeability and pore size distribution 128
5.6.5 Effective diffusion coefficient and electrical conductivity 129
5.7 SUMMARY OF THE INTEGRATED METHODS AND THEIR APPLICATION TO POROUS SANDSTONE 130

6 APPLICATION OF INTEGRATED METHODS TO THE STUDY OF POROUS MATERIALS 132

II: POLYMER FOAMS 132

6.1 INTRODUCTION TO POLYMER FOAMS 133

6.2 EXPERIMENTAL 135

6.2.1 Porous polymer foams and the method used for their production 135

6.2.2 Preparation of polymer foams by polymerisation of the continuous phase of emulsion templates 136

6.3 CHARACTERISATION METHODS 138

6.3.1 Scanning electron microscopy (SEM) 138

6.3.2 Material and foam density measurements of porous polymers 138

6.3.3 Mechanical testing of porous polymers 139

6.4 RESULTS AND DISCUSSION OF STRUCTURAL AND PERMEABILITY INVESTIGATIONS OF POLYMER FOAMS 139

6.5 SUMMARY OF THE INTEGRATED METHODS AND THEIR APPLICATION TO POROUS POLYMER FOAMS 155

7 CONCLUSIONS AND FURTHER WORK 157

7.1 CONCLUSIONS 157

7.1.1 Development of the combination methods 157

7.1.2 Integrated gas permeability and diffusivity apparatus 158

7.1.3 Integrated mercury porosity, permeability and electrical conductivity apparatus 159

7.1.4 General conclusions 160

7.1.5 Limitations of the current study 161

7.2 RECOMMENDATIONS FOR FURTHER WORK 162

Integrated gas permeability and diffusivity: 162

Integrated mercury porosimetry, permeability and electrical conductivity: 163

REFERENCE LIST 164

APPENDIX I - OPERATING PROCEDURE FOR THE PROTOTYPE GAS PERMEABILITY APPARATUS 173

APPENDIX II - OPERATING PROCEDURES FOR THE INTEGRATED GAS PERMEABILITY AND DIFFUSIVITY APPARATUS – GAS PERMEABILITY 175

APPENDIX III - OPERATING PROCEDURES FOR THE INTEGRATED GAS PERMEABILITY AND DIFFUSIVITY APPARATUS - GAS DIFFUSIVITY 179

APPENDIX IV – CALCULATION OF TRANSIENT DIFFUSION 184

APPENDIX V - OPERATING PROCEDURE FOR THE INTEGRATED MERCURY APPARATUS 186

APPENDIX VI – GRAPHICAL REPRESENTATIONS OF TURBULENT RESULTS 190

APPENDIX VII – THIN-SECTION IMAGES 195

LIST OF FIGURES AND TABLES

Figure 1-1: Illustration of pores and pore throats that exist between sand grains in sandstone 2

Figure 1-2a: SEM image of a porous polymer foam and b: SEM image of sponge (A. Mannelin) 3

Figure 1-3: SEM image of sandstone illustrating the pores present between grains 6

Figure 1-4: Illustration of the effective length L_{eff} of a pore compared with the length of the sample L 7

Figure 2-1: Schematic diagram of the extrapolation of the Knudsen diffusion coefficient from the linear viscous permeability 28

Figure 2-2: Schematic representation of the mercury porosimetry method showing the increase of mercury penetration of the pores as the applied pressure is increased 42

Figure 2-3: Diagram of mercury flow apparatus used by Hewitt (1967) 45

Figure 2-4: Diagram of the mercury conductivity cell used by Hewitt (1967) 50

Figure 3-1: Dimensions of the sample mould for sealing porous solid samples 55

Figure 3-2: Dimensions of coated sample 56

Figure 3-3: Photograph of primary gas permeability apparatus 57

Figure 3-4: Schematic diagram of the test cell (around sample) and connections 59

Figure 3-5: Permeability coefficient plot for sandstone permeability measurement in the prototype pressure-rise cell 61

Figure 3-6: Permeability results from measurements obtained using the Hassler cell method 62

Figure 3-7: Photograph of the integrated gas permeability and diffusivity apparatus 65

Figure 3-8: Detailed diagram of the sample cell of the gas permeability and diffusivity apparatus showing inlet and outlet points (not to scale) 66

Figure 3-9: Schematic of the pressure-rise gas permeability measurement apparatus 67

Figure 3-10: Schematic of the diffusivity measurement apparatus 69

Figure 3-11: Rate of oxygen diffusion through pores of Sample R1 70

Figure 3-12: Plot of experimental transient diffusion data fitted to theoretical data at $F = 0.5$ for Sample R1 71

Figure 4-1: Illustration of the mercury permeability and conductivity apparatus 75

Figure 4-2: Schematic of the porosity/permeability/conductivity apparatus 81

Figure 4-3: Detail of the sample cell 82

Figure 4-4: Pore volume distribution as a function of the applied pressure for sandstone Sample R1 84

Figure 4-5: Schematic procedure used for mercury permeability measurements 86

Figure 4-6: Permeability distribution for sandstone Sample R1 89

Figure 4-7: Relative permeability curve for sandstone R1 90

Figure 4-8: Conductance as a function of saturation for Sample R1 92

Figure 4-9: Tortuosity τ_p as a function of pore volume occupied for sandstone Sample R1 .. 93

Figure 5-1: Permeability coefficient K at various mean pressures for sandstone Samples R4 and R5 used to demonstrate the reproducibility of data collected using the integrated gas permeability cell 98

Figure 5-2: Permeability coefficient at various mean pressures for sandstone Samples S1 – S4 99

Figure 5-3: Permeability coefficient at various mean pressures for sandstone Samples S5 – S8 100

Figure 5-4: Results of gas permeability tests on sandstone Samples S9 and S10 from the investigation of low mean pressure..... 102

Figure 5-5: Linear plot of C vs. $V\left(\frac{dp_2}{dt}\right)$ for sandstone Sample S1..... 103

Figure 5-6: Oxygen concentration in the nitrogen purge stream as function of time for sandstone R4 106

Figure 5-7: Oxygen concentration in the nitrogen purge stream as function of time for Sample R5..... 107

Figure 5-8: Pore volume distributions for sandstone samples S2, S3, S5 and S6 110

Figure 5-9: Pore size distributions of sandstone samples S2, S3, S5 and S6 111

Figure 5-10: Applied pressure as a function of the mercury saturation..... 112

Figure 5-11a – d: Permeability distribution of SamplesS2, S3, S5 and S6. 107

Figure 5-12: Permeability as a function of pore volume occupied for Sample S5 115

Figure 5-13: Relative permeability as a function of mercury saturation for Sample S5 116

Figure 5-14: Pore size and permeability distribution of Sample S2 117

Figure 5-15: Pore size and permeability distribution of Sample S3 118

Figure 5-16: Pore size and permeability distribution of Sample S5 119

Figure 5-17: Pore size and permeability distribution of Sample S6 120

Figure 5-18: Plot of conductivity ratio r_{Cp} as a function of applied pressure for Sample S2 121

Figure 5-19: Relative conductivity r_{Cp} as a function of pore size penetrated for Sample S5 122

Figure 5-20: Relative conductivity r_{Cp} as a function of pore size penetrated for Sample S6 123

Figure 5-21a and b: Microscope images of sandstone Sample S1 124

Figure 5-22: Permeability measurements obtained from gas and mercury techniques and predictions from image analysis and turbulent effects 127

Figure 6-1: Illustration of the dispersion of the internal phase in the continuous monomer phase to form an emulsion template 133

Figure 6-2a to d: SEM images of polyHIPEs to polyMIPEs 1 to 4 140

Figure 6-3a to d: SEM images of polyMIPEs to polyLIPEs 5 to 8 141

Figure 6-4: Mechanical test results - variation of the mechanical properties with internal phase volume of emulsions 143

Figure 6-5: Gas permeability analysis: variation of the permeability coefficient with mean pressure for Set 1 and Set 2 samples 145

Figure 6-6: Mercury permeability distribution analysis of Samples 3to 8: permeability as a function of applied pressure for Set 1 and Set 2 samples 147

Figure 6-7: Comparison of the pore throat diameter determined from SEM analysis and mercury intrusion for the flow limiting pore throat diameter 148

Figure 6-8: Permeability distribution (square points) and pore size distribution (dotted line) of polyMIPE 3 150

Figure 6-9: Permeability distribution (square points) and pore size distribution (dotted line) of polyMIPE 4 151

Figure 6-10: Permeability distribution (square points) and pore size distribution (dotted line) of polyMIPE 5 152

Figure 6-11: Permeability distribution (square points) and pore size distribution (dotted line) of polyMIPE 6 153

Figure 6-12: Permeability distribution (square points) and pore size distribution (dotted line) of polyMIPE 7 153

Figure 6-13: Permeability distribution (square points) and pore size distribution (dotted line) of polyLIPE 8 154

Figure A-1: Gas permeability cell set-up 175

Figure A-2: Diffusivity cell set-up 179

Figure A-3: Plot of oxygen concentration variation with time 182

Figure A-4: Plot of theoretical data fitted to experimental transient diffusion data 183

Figure A-5: *C* vs. $V(dp_2/dt)$ obtained by analysis of turbulence for sandstone Sample S1 .. 190

Figure A-6: *C* vs. $V(dp_2/dt)$ obtained by analysis of turbulence for sandstone Sample S2 .. 191

Figure A-7: *C* vs. $V(dp_2/dt)$ obtained by analysis of turbulence for sandstone Sample S3 .. 191

Figure A-8: *C* vs. $V(dp_2/dt)$ obtained by analysis of turbulence for sandstone Sample S4 .. 192

Figure A-9: *C* vs. $V(dp_2/dt)$ obtained by analysis of turbulence for sandstone Sample S5 .. 192

Figure A-10: *C* vs. $V(dp_2/dt)$ obtained by analysis of turbulence for sandstone Sample S6 193

Figure A-11: *C* vs. $V(dp_2/dt)$ obtained by analysis of turbulence for sandstone Sample S7 193

Figure A-12: *C* vs. $V(dp_2/dt)$ obtained by analysis of turbulence for sandstone Sample S8 194

Figure A-13a and b: Microscope images of sandstone Sample S2 195

Figure A-14a and b: Microscope images of sandstone Sample S3 195

Figure A-15a and b: Microscope images of sandstone Sample S4 196

Figure A-16a and b: Microscope images of sandstone Sample S5 196

Figure A-17a and b: Microscope images of sandstone Sample S6 196

Figure A-18a a and b: - Microscope images of sandstone Sample S7 197

Table 3-1: Results of permeability measurements 63

Table 4-1: Summary of the results obtained using the mercury porosimetry technique for sample R1 85

Table 4-2: Summary of the results obtained using mercury permeability and conductivity techniques on Sample R1 92

Table 5-1: Sample codes, density and porosity values of the sandstone samples used in this study 96

Table 5-2: Standard deviations of the results obtained from reproducibility experiments 97

Table 5-3: Porosity and permeability results 101

Table 5-4: Reproducibility of steady state and transient diffusion results for sandstone Samples R4 and R5 108

Table 5-5: Summary of diffusivity results 109

Table 5-6: Summary of the results of porosity, specific surface, pore diameter and permeability obtained from analysis of thin-section microscopic images 125

Table 5-7: A summary of the permeability measurements and predictions of sandstone Samples S1 – S8. k_{gas} = permeability measured using gas, k_{Hg} = permeability measured using mercury, k_{turb} = permeability predicted from turbulent analysis, k_{image} = permeability predictions from image analysis and K_0 = Knudsen diffusion coefficient 126

Table 5-8: Comparison of values of r_D and r_{Cp} obtained from diffusion and from conductivity at high applied pressure respectively 130

Table 6-1: Summary of the polymer foams produced and the naming system 137

Table 6-2: Summary of the measured properties of the polymer foams 144

Table A-1: Theoretically calculated values of F (in the matrix of the table) as a function of $\left(\frac{D_{AB}t}{L_{eff}^{\ 2}}\right)$ (in bold). 185

NOMENCLATURE

Symbol	Parameter	Units
A	Cross sectional area of sample	m^2
A_1	Cross sectional area of manometer tubes	m^2
A_2	Cross sectional area of sample	m^2
A_p	Cross sectional area of pore	m^2
a	Viscous flow coefficient	Dimensionless
b	Inertial effect coefficient	Dimensionless
C	Turbulent factor	Dimensionless
c	Carman-Kozeny constant	Dimensionless
c_O	Concentration of oxygen	ppm v/v
D_{AB}	Diffusion coefficient of gas A in gas B	$m^2\ s^{-1}$
D_{eff}	Effective diffusion coefficient	$m^2\ s^{-1}$
d	Pore diameter	m
E	Electrical potential difference	Volt
F	Oxygen concentration as a fraction of its value at infinite	Dimensionless
$\dot{G}$	Mass flux	$kg\ s^{-1}$
g	Acceleration due to gravity	$m\ s^{-2}$
h	Height of mercury in manometer tubes	m
I	Electrical current	A
K	Permeability coefficient	$m^2\ s^{-1}$
K_0	Slip coefficient	m^2
k	Viscous permeability	m^2

k_l	Liquid permeability	m^2
K_P	Hagen-Poiseuille permeability	m^2
L	Sample length	m
L_{eff}	Effective sample length	m
M	Molecular weight of gas	g mol^{-1}
N_O	Concentration of oxygen	mol m^{-3}
n_o	Molar transport rate of oxygen	mol s^{-1}
p	Applied pressure	Pa
p_0	Initial pressure	Pa
P_{1O}	Partial pressure of oxygen	Pa
p_1	Upstream pressure	Pa
p_2	Downstream pressure	Pa
p_m	Mean pressure	Pa
Q	Volumetric flowrate	m^3 s^{-1}
Q_2	Volumetric flowrate downstream of sample	m^3 s^{-1}
Q_N	Volumetric flowrate nitrogen	m^3 s^{-1}
R	Gas constant	J K^{-1} mol^{-1}
Re	Reynolds number	Dimensionless
R_s	Resistance of sample	Ω
r	Radius of pore	m
r_C	Conductivity ratio	Dimensionless
r_{CP}	Conductivity ratio at applied pressure	Dimensionless
r_D	Diffusivity ratio	Dimensionless
S_c	Specific pore circumference	m

S_s	Specific surface area	$m^2\ m^{-3}$
T	Temperature	K
t	Time	s
u	Superficial velocity	$m\ s^{-1}$
u_{1o}	Superficial velocity of oxygen	$m\ s^{-1}$
V	Volume	m^3
V_b	Bulk volume	m^3
V_l	Volume of liquid	m^3
V_s	Volume of pore space	m^3
γ	Mercury surface tension	N m
ε	Porosity	%
ε_{eff}	Effective porosity	%
θ	Contact angle between mercury and sample	◦
μ	Fluid viscosity	Pa.s
ρ	Fluid density	$kg\ m^{-3}$
ρ_{abs}	Absolute density	$kg\ m^{-3}$
ρ_b	Bulk density	$kg\ m^{-3}$
ρ_s	Envelope (apparent) density	$kg\ m^{-3}$
τ	Tortuosity	Dimensionless
τ_p	Tortuosity at applied pressure *p*	Dimensionless
σ	Electrical conductivity of saturated medium	$\Omega^{-1}\ m^{-1}$
σ_o	Electrical conductivity of mercury	$\Omega^{-1}\ m^{-1}$
σ_p	Electrical conductivity of saturated medium at pressure *p*	$\Omega^{-1}\ m^{-1}$
$\bar{v}$	Mean molecular velocity of diffusing gas	$m\ s^{-1}$

ACKNOWLEDGEMENTS

I would like to express gratitude to my supervisors Professor Alexander Bismarck and Professor Geoffrey Hewitt for the guidance and advice they have provided throughout the course of this work. I acknowledge my industrial supervisor Dr. Ian Robb at Halliburton Energy Services for his input and advice and would also like to acknowledge my collaborating academic Dr. Frantisek Stepanek.

I would like to thank Professor Martin Blunt and Professor Ken Sorbie for serving on my examination panel.

I am pleased to thank Mr Jonny Johnson at Halliburton Energy Services, for the production of the gas permeability/diffusivity sample cell. Thanks also to Mr Richard Wallington who advised and oversaw the production of the prototype gas permeability and for much valued advice about the construction of the mercury apparatus. Thanks to Mr Paul Hands at Birmingham University for the production of thin-sections of samples.

I thankfully acknowledge Dr. Angelika Menner and Dr. Zdenek Grof for their collaboration with polyHIPE work and Ms Nadine Graeber for preparation and measurements of polyHIPE samples. My thanks to my friends and colleagues in the PaCE group at Imperial College, London.

For funding, I gratefully acknowledge the EPSRC and Halliburton Energy Services.

Sincere thanks to Ms Anita and Mr Terence Ngai, for providing me with a space to work on this thesis. My dearest friend Ms Dolapo Shobanjo, who has been a much valued source of encouragement, must also be thanked for her help with SEM images and thin-section transportation.

My parents Dr. Berwick and Mrs Ban Hwa Manley and my sisters, Misses Hui Lan and Hui Yang Manley, I thank for provision of unconditional support and inspiration. I also thankfully acknowledge Miss Hui Lan Manley's artistic contribution to many of the drawings presented in this thesis. Finally, I thank Mr Ross Gordon for his love, encouragement and much appreciated editing efforts.

This thesis is dedicated to my parents

CHAPTER 1

INTRODUCTION

The focus of the work described in this thesis is on the determination of characteristics of the transport of gases and liquids in porous media, both by flow though the media under the influence of a pressure gradient and by diffusional processes which occurs in the absence of a pressure gradient. Measurement and understanding of these transport processes is not only important in itself, but also throws light on many structural aspects of the porous material.

In what follows, a general introduction to porous media is presented in *Section 1.1* and *Section 1.2* presents the aims of this project. The major objective of the project has been the development of new **integrated methods** for characterisation of porous solids and the strategy for achieving this objective is summarised in *Section 1.3.*

1.1 Porous solids

A porous material is generally defined as a solid that contains holes or pores which are distributed throughout the material. In general, granular porous materials can be envisaged as a structure formed by the collection of small grains or particles that are closely packed together (Collins, 1961). Since the particles usually vary in shape and size, there exist cavities or voids between them.

Figure 1-1 is an illustration showing the presence of pores between grains; this simplified schematic of a granular porous material also shows the pore throats that connect the pores. The pore throats are circled in the diagram.

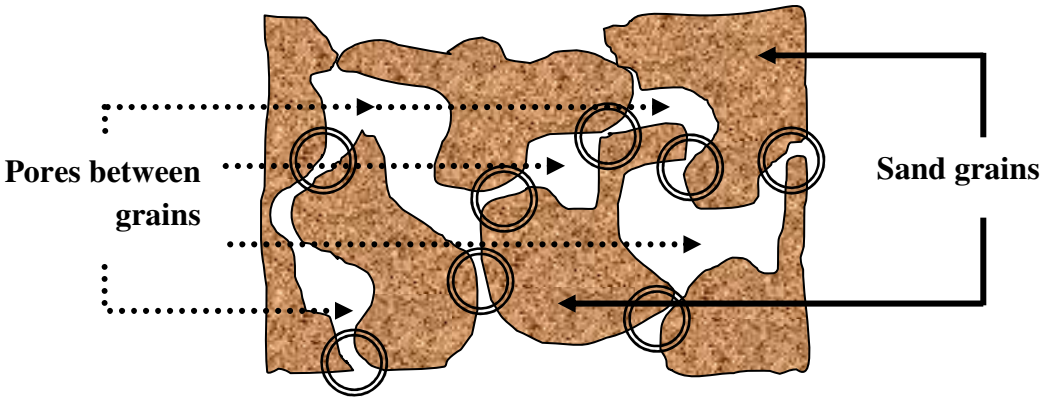


Figure 1-1: Illustration of pores and pore throats that exist between sand grains in sandstone

Porous solids such as porous polymer foams have a different structure to granular porous solids as the materials are not formed from grains. An SEM (Scanning Electron Microscope) image of a typical polymer foam synthesised by the polymerisation of emulsion templates is shown in Figure 1-2a. The structure is governed by the formation of a skeleton of organic material which surrounds pore spaces. The pores are still connected however via pore throats in a similar way to granular material. An example of a naturally occurring skeletal porous material is sponge; an SEM image of a typical sponge is given in Figure 1-2b.

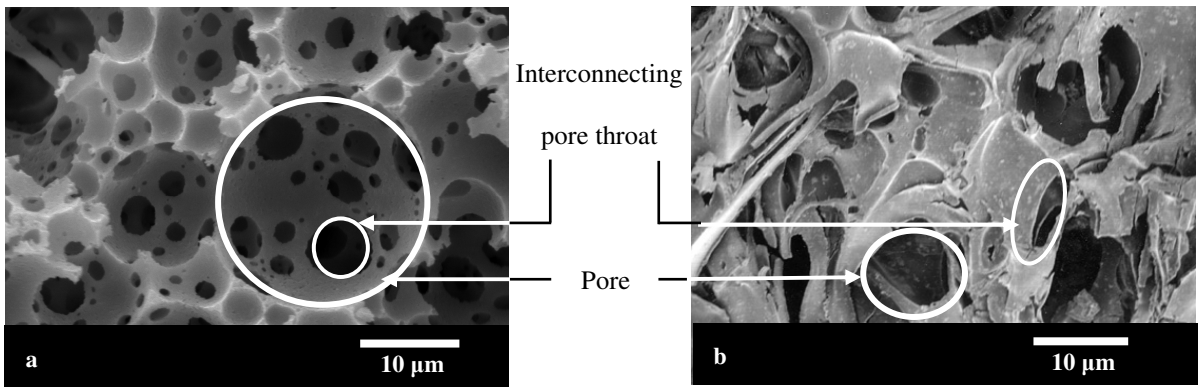


Figure 1-2a: SEM image of a porous polymer foam and b: SEM image of sponge (A. Mannelin)

The flow of fluids in porous solids is determined by the nature of the pores and pore throats. Pores can either be interconnected (by pore throats) or non-interconnected; fluid can only flow through a porous solid if (at least) some of the pores are interconnected (Collins, 1961). Interconnected pores therefore form a network that allows fluid flow within the system. Understanding the pore size distribution and structure of this network is a very important step in understanding the characteristics of fluid flow through the porous medium. Similarly, mass transfer by diffusion of species through the pores of the medium in the absence of flow is also affected (though in a different way) by the pore structure. There is therefore a need to understand, in as much detail as possible, not only the pore sizes within a material but also the pore structure.

The challenges associated with the characterisation of porous solids have been of interest to engineers and scientists for many decades and this is recognised in reviews by Collins (1961), Dullien (1979) and Muskat (1937). In recent years, interest in porous media characterisation has increased considerably, in particular due to issues associated with oil

production in petroleum engineering (Baas *et al*., 2007 and Berkowitz, 2002). Porous media occur widely in nature and in technologically significant materials and play an important role in other fields such as:

- **Tissue engineering** – the structure of scaffolds used for tissue engineering and cell cultures is important as it affects the flow of nutrients and metabolic waste products necessary for cell growth.
- **Porous polymers** – the use of polymers including biological and inorganic membranes and ion-exchange modules is dependent on the porous structure of the material.
- **Heterogeneous catalysis** – the dynamics of diffusion of gases and flow of liquid reactants are dependent on the catalyst pore structure. Similarly, impregnation of porous catalysts with catalyst precursors and the distribution of molten catalyst are processes that depend on pore structure.
- **Separation processes** – the effectiveness of processes including gel permeation chromatography, membrane separation and filtration is dependent on the structure of the porous separation medium.
- **Contaminant transport** – understanding the extent of transport of hazardous waste or pollution through contaminated land can impact on waste disposal and on property redevelopment.
- **Soil mechanics** – analysis of soil porosity, permeability and consolidation is important when assessing potential site conditions.

- **Hydrology** – measurement of water movement in earth and sand structures is fundamental in assessing water resources and understanding the processes involved in the hydrologic cycle.
- **Petroleum engineering** – this sector is concerned with petroleum and natural gas production, exploration and well drilling. The study of the structure and flow properties of oil-bearing formations is important when optimising the production of oil wells. Sandstones are of particular interest in the context of this project due to the predominance of sandstone reservoirs; the diversity of the sediment properties of sandstone reservoir material has led to the development of a range of experiments to investigate a large range of properties with a focus on porosity and permeability.

Sandstone is an example of a granular porous solid and is formed by the cementing of grains of sand under the action of high pressures and temperatures on accumulations of sediment. Due to its formation process by pressure compaction and the wide variety of the binding cements, there exists a structurally diverse range of sandstones. An SEM image representative of a typical sandstone sample is presented in Figure 1-3 and illustrates the pore spaces that are present between the sand grains.

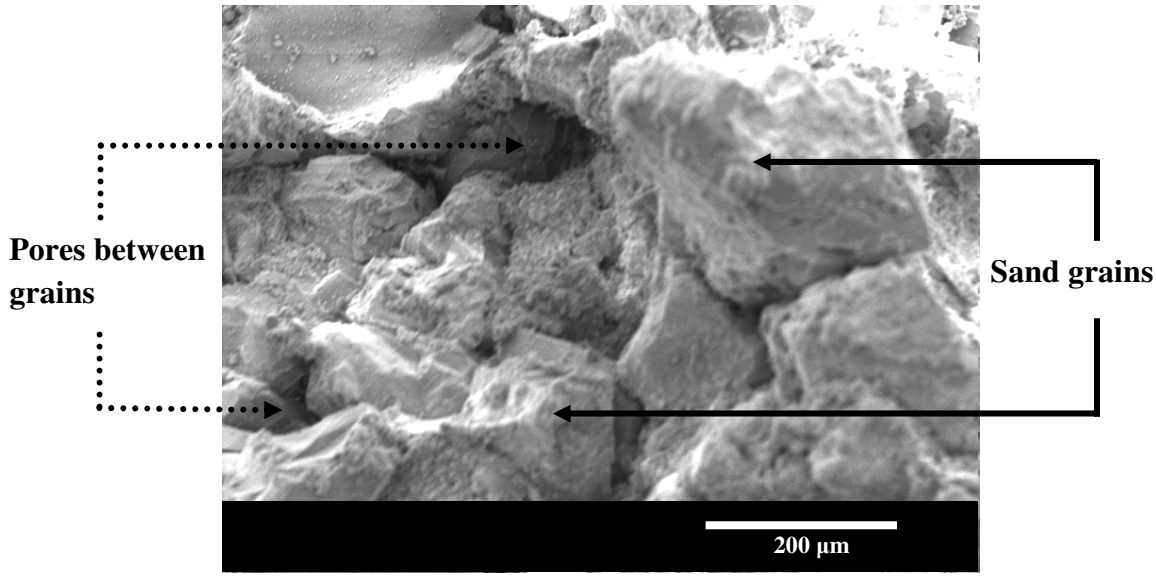


Figure 1-3: SEM image of sandstone illustrating the pores present between grains [1]

The most significant properties of porous solids that affect fluid flow are porosity, permeability and pore tortuosity (Le Coq, 2008) and are of particular interest in this work**.** Porosity is a measure of the ratio between the volume of pore space in a sample and the total bulk volume of the sample. The porosity determines the fluid capacity of the medium. Muskat (1937) defines permeability as a measure of the ease of fluid flow traversing the medium under the influence of a driving pressure. Similarly, tortuosity will affect the fluid flow, as it is likely that the path taken by the fluid flow will be much longer than the actual sample length. The ratio of the effective pore length to the actual length of the sample is defined as the tortuosity as illustrated in Figure 1-4.

[1] SEM image taken by Ms Dolapo Shobanjo from the Department of Chemical Engineering, Birmingham University.

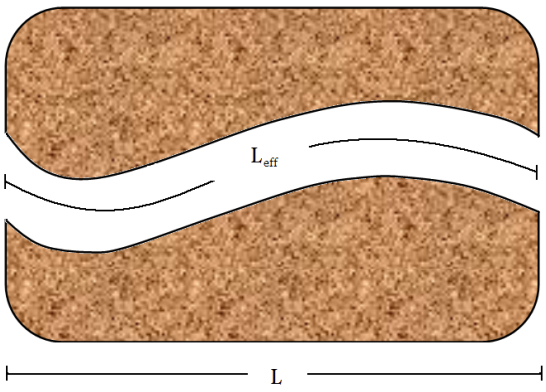


Figure 1-4: Illustration of the effective length L_{eff} of a pore compared with the length of the sample L

Extensive work has been carried out on many types of porous media to try and gain an understanding of the structures of the materials and how fluid flow is affected by these structures (see for instance Botset *et al.,* 1933, Lafhaj *et al*., 2002, Baraka-Lokmane, 2002, Biloe & Mauran, 2003, Kallel, 2004 and Raharjo *et al.,* 2007). The complexity and variety of porous materials has led to the application of many experimental techniques for their characterisation**.** Attention has been focused on properties that have direct and significant effects on the flow of fluids through the material, most prominently porosity and permeability. Early methods for the characterisation of porous media are reviewed by Collins (1961), Carman (1956) and Dullien (1979). More recent reviews are those by Sing (2004) and Dietrich (2005).

The focus of the work described in this thesis is on gaseous transport (permeability and diffusion) and on mercury penetration (porosity, permeability and conductance) methods. However, it should be recognised that a whole range of other techniques have been deployed in characterising porous media; these have included:

- Pore size distribution
- Structural analysis and permeability predictions from stereological image analysis
- Liquid permeability
- Structural analysis and permeability predictions from stereological image analysis
- X-ray tomography
- Electron microscopy for imaging porous solids

These methods are briefly reviewed and are discussed in Chapter 2 of this thesis. However, the main focus in Chapter 2 is on discussing the bases for the *integrated* methods for gaseous transport and mercury penetration which are presented in Chapters 3 and 4, respectively. Integrated methods consist of a single piece of apparatus which encompasses several characterisation techniques and can be used to measure multiple independent properties simultaneously. Integrated methods can significantly improve the efficiency of characterisation of flow properties.

1.2 Project aim

The aim of this project was to identify and develop new integrated techniques to experimentally determine fluid transport properties of porous solids. The overall aims and research objectives were as follows:

- Develop an integrated method for characterisation of gaseous transport in porous solids; specifically gas permeability and diffusivity.

- Develop an integrated method for characterisation of porous solids using mercury penetration techniques, specifically to characterise pore size distribution, permeability distribution and electrical conductivity.
- Compare the values obtained for (a) gas permeability and mercury permeability, and (b) gas diffusivity and mercury conductivity.
- Investigate the significance of the techniques by comparisons to predictions of properties from image analysis.

In order to achieve these aims, work was carried out in the following stages:

- Construction of prototype gas permeability measurement apparatus.
- Development of integrated gas permeability and diffusivity apparatus.
- Commissioning of mercury intrusion apparatus.
- Study of pore structures using mercury penetration.
- Study of the comparisons of porosity, permeability and tortuosity results obtained using gas and mercury apparatus.
- Study of porosity, effective pore length and pore size from image analysis.

1.3 Thesis structure

This thesis presents work on the development of integrated methods for gas transport and for mercury penetration, transport and conductance in porous media and on the application of these methods to the study of two classes of media, namely porous sandstones and polymer foams. Chapter 2 reviews the background literature; the main focus is reviews of the bases of

gaseous transport in porous media (*Section 2.2*) and methods of characterisation using mercury penetration (*Section 2.3*). However, a brief review is also presented of alternative methods of characterisation (*Section 2.1*). In Chapter 3, a new integrated apparatus for gaseous permeability and diffusion measurement is described and in Chapter 4, a new integrated apparatus is described which allows porosity, permeability and conductivity measurements to be made as a function of mercury penetration. The application of these new experimental systems to the study of two classes of porous media (porous sandstones and polymer foams) is described in Chapters 5 and 6 respectively. Finally, Chapter 7 draws overall conclusions from the study and makes suggestions for future work.

CHAPTER 2

BACKGROUND

The focus of the work described in this thesis was on the development of integrated methods for the measurement of gaseous transport in porous solids and for the applications of mercury penetration techniques. The background literature in these two areas is reviewed in *Sections 2.2* and *2.3* respectively. However, it should be recognised that, reflecting the great technological importance of porous solids, a whole range of other characterisation methods have been developed. For completeness, some of these methods are summarised briefly in *Section 2.1*. Extensive reviews of early work on characterisation methods for porous media have been given by Collins (1961), Dullien (1979) and Carman (1956); more recent reviews in this area are those of Sing (2004) and Dietrich (2005).

2.1 Characterisation of porous solids

In addition to the gaseous transport and mercury penetration techniques which are the main focus of the present study (and for which the background is given in *Sections 2.2* and *2.3*), a variety of other measurements are used to characterise porous media and some of the main ones in this category are summarised below.

2.1.1 Total porosity

Porosity is defined as the ratio of the void space volume V_s to the bulk volume V_B of a porous material. This property is important in terms of porous media characterisation as it gives an indication of the total volume available for the storage of fluids within the medium. Tiab & Donaldson (1996) show that factors governing the magnitude of the porosity are, in the case of sedimentary material, the uniformity of the grain size and the degree of sedimentation or consolidation of the material. Other important factors regarding the nature of porosity include the types of void spaces present and whether the pores are closed or interconnected. A number of methods have been used to estimate porosity; amongst these are optical methods, mercury intrusion methods (as reviewed in *Section 2.3*) and gas expansion methods (Dullien, 1979). Perhaps the most commonly used is the density method which initially requires the measurement of the bulk volume by means of gas saturation. The technique enables the measurement of the apparent and bulk density of porous materials by means of fluid displacement. The apparent (or envelope) density ρ_S of a solid can be found using helium pycnometry and is defined by Subcommittee on Characterisation of Porous Solids (1994), as the ratio of the sample mass to the volume V_S of the envelope of fluid that surrounds the solid. Helium flows into the pores of a sample with a known mass, and the volume of gas that saturates the sample is measured, subsequently allowing the deduction of the envelope density. The material mass $m = \rho_S V_S = \rho_B V_B$, where $\rho_{\mathbf{B}}$ and V_B are the bulk density and bulk volume of the medium. It follows that Equation 2.1 may be used to give a value of for the total porosity ε.

$$\varepsilon = \left(1 - \frac{V_S}{V_B}\right) \times 100 \qquad 2.1$$

Density and porosity measurements provide a basic representation of the sample structure which can be used as a basis for the comparison of physical properties. A more direct method for determining the porosity is to measure the bulk volume of the sample, then compact it removing all pore spaces and re-measure the volume. This method is commonly used for bricks and ceramics as described by Collins (1961).

2.1.2 Pore size distribution

Collins (1961) defines the pore size distribution as the probability density function giving the distribution of pore volume by a characteristic pore size. The most common methods of determining the pore size distribution are either by mercury porosimetry for large pores or gas adsorption for the determination of the pore size distribution of microstructures or by liquid displacement. The mercury porosimetry method is described in detail in *Section 2.3* and is the most widely applied. However, there are some alternative methods which are mentioned here. The pore size distribution may be determined by the gas-liquid displacement method. In this method a wetting liquid is used to saturate the pores and pore throats of a sample. A flow of dry air is applied underneath the sample, flowing upwards. A saturated sample will pass air when the applied air pressure exceeds the capillary attraction of the fluid in the pores. As the pressure is increased, the flowrate and pressures above and below the sample are measured. Smaller pores are opened with increasing air pressure. Averages of the

measurements are taken and are related to the pore sizes that are evacuated at certain pressures. A gas-liquid capillary pressure curve can be used to obtain a distribution of the average pore entry radii of the sample. Tiab & Donaldson (1996) show that this gives an overview of the pore size distribution. However, this method is affected by leakages of gas around the edges of sample. This may lead to inaccurate readings so, typically, the sample is sealed to eliminate any cross-flow.

2.1.3 Liquid permeability

Permeability is arguably the most important property of a porous medium. It is a measure of the ease by which a fluid is able to flow through a material by the application of a pressure gradient, (Muskat, 1937, Collins, 1961). Permeability is defined by Botset *et al*. (1933) as the volume of a fluid of unit viscosity passing in unit time through a unit cross section of the porous medium under the influence of a unit pressure gradient and is independent of the absolute pressures or velocities within the flow system or the nature of the fluid and is characteristic of only the medium. Permeability is approximately a measure of the mean square pore diameter in the material (Collins, 1961). Measurements of this property can provide information about the pore structure and the tortuosity of interconnected pores within a sample (Ishizaki *et al.*, 1998). Permeability is related to the structure of the medium, in particular to the porosity, pore shape, pore size and size distribution (Miguel & Serrenho, 2007).

At low fluid flowrates the flow is described by Hatfield (1939) as viscous and the permeability is calculated from Darcy's Law (Equation 2.2).

$$k = \frac{Q\mu}{A(\Delta p / L)} \qquad 2.2$$

where k is the permeability, Q is the volumetric flowrate, μ is the fluid viscosity, A is the cross-sectional area of the sample, Δp is the pressure difference across medium and L is the sample length. The SI unit for permeability is m^2 but it is more common oil industry practice to state permeability in Darcys[2] or milliDarcys (1 Darcy = 10^{-12} m^2).

Darcy's Law applies if the fluid is a single-phase medium and the flow is laminar (Lafhaj *et al.,* 2002). If the fluid velocity is increased past a critical value the flow becomes turbulent and is characterised by eddies that cause mixing of the fluid. The type of flow and the transitional velocity of the fluid are dependent on the pore sizes and shapes and also on properties of the fluid, such as the viscosity and density. Lafhaj *et al.* (2002) state that the Reynolds number *Re* should be less than 1000 when the flow is laminar. The Reynolds number is calculated using Equation 2.3:

[2] A unit of permeability, equivalent to the passage of 1 cubic centimetre of fluid of 1 centipoise viscosity flowing in 1 second under a pressure of 1 atmosphere through a porous medium having a cross sectional area of 1 square centimetre and a length of 1 centimetre.

$$\mathrm{Re} = \frac{\rho u d}{\mu} \qquad 2.3$$

where ρ is the fluid density, u is the fluid velocity and d is the pore diameter. Numerous techniques have been developed to try and relate the permeability of a medium to other characteristics which are perhaps easier to measure, such as the porosity and electrical conductivity in work carried out by Katz & Thompson (1986). Relating the transport properties of a porous medium to the pore structure has been a long term goal of researchers in the fields of petroleum engineering, hydrology, earth science and chemical engineering (Lock *et al.,* 2002).

The permeability of a wetting liquid (which completely fills the pore structure), such as water, through a porous sample can be measured simply by applying a continuous flow of liquid through the sample with a constant pressure at one end and atmospheric pressure at the other (Lafhaj *et al.,* 2002). The volume of liquid that flows through the sample is measured at specific time intervals which can be used to calculate the volumetric flowrate. Such measurements have been carried out by many researchers including, Baraka-Lokmane (2002), Botset *et al.* (1933), Lafhaj *et al.* (2002) and Despois & Mortensen (2005) on a range of porous media.

A "Ruska Type" liquid permeameter used by Tiab & Donaldson (1996) can be used to make liquid permeability measurements by determination of the time taken for a fixed volume of

liquid at a constant temperature to pass through a sample at a specific pressure gradient. The relationship given in Equation 2.4 can be applied to determine the liquid permeability:

$$k_l = \frac{\mu V_l L}{A \Delta p t} \qquad 2.4$$

where k_l is the liquid permeability, V_l is the volume of liquid flowing over time t and Δp is the pressure difference across sample.

A method used by Baraka-Lokmane *et al.* (2008) required the use of a Hoek cell, usually used for rock deformation tests, to mount the sample cores. For liquid permeability measurements, the cores were mounted vertically, the cell provided a means of applying confining pressure to the sample. Brine was pumped into the top side of the cell and fluid flowed through the core and was collected in a reservoir mounted on a balance. The weight measurements were used to calculate flowrates.

An alternative method of beam bending for determining permeability of was originally developed for gels and later extended to more rigid materials by Scherer *et al*. (2007). When a beam of test material (usually porous glass or cement) is saturated with fluid and is bent, the top half is compressed and the bottom half is stretched. A pressure gradient is created across the material and liquid flows from the top to the bottom within the beam. The liquid also flows out of the top into a surrounding bath and into the bottom from the bath. As the pore pressure equilibrates, the force required to sustain a fixed deflection decreases, and the

kinetics of relaxation of the force can be analysed to obtain the permeability; additionally, it is possible to obtain the elastic modulus and the viscoelastic stress relaxation function of the solid phase.

2.1.4 Relative permeability

In systems which contain two or more immiscible fluids, permeability is measured in terms of the reduction of the ability of flow due to the fluid interactions. This is called the relative permeability and is defined as the ratio of the effective permeability to the absolute permeability of the material. Relative permeability is used to describe the simultaneous transport of the immiscible phases through a porous medium assuming that each fluid remains continuous through the material and that the flow is one-dimensional (Heaviside, 1983). It is a function of porous material and fluid chemical and physical properties, (Donaldson & Tiab, 1996). Relative permeability is thought to be affected by pore geometry, wettability, fluid distribution and saturation, the characterisation of such properties should give valuable information regarding the fluid flow, (Harvey *et al.* 1986). Relative permeability of a porous solid-fluid system can be determined by either dynamic displacement tests or a steady-state flow method (Heaviside, 1983). In steady-state methods for the measurement of relative permeability, two fluids are made to flow into a sample at steady flowrates at various saturations, (Donaldson & Tiab, 1996). An example of a steady-state method is the Hassler technique, where a sample of predetermined saturation is placed in a Hassler sleeve and flows of both fluids are applied to face of the sample. The flowrates are measured and when the outlet flowrates match the inlet flowrates, is assumed to be at

steady state, the sample saturation is then determined from the sample mass, pore volume and densities of the two fluids. The relative permeability values are computed using an extended Darcy's law for two-phase flow in porous media under steady state conditions and can be written as shown in Equation 2.4a (Muskat, 1937 and Dullien, 1979):

$$q_i = \frac{k_{ri} k A}{\mu_i} \frac{\partial p_i}{\partial x} \qquad 2.4a$$

where q_i is the volumetric flowrate, μ_i is the viscosity of fluid *i,* k_{ri} is the effective permeability of fluid *i* and is a function if the liquid saturation and k is the absolute permeability which is an intrinsic property of the pore structure.

2.1.5 Structural analysis and permeability predictions from stereological image analysis

The term s*tereology* was developed to describe methodologies that allow access to 3-dimensional information about geometrical structures based upon observations made on 2-dimensional sections (Garcia *et al.,* 2007). Stereological investigations give an insight into the physical form and structure of a material and are readily performed using imaging techniques. Stereological parameters such as pore and pore throat diameter and perimeter as well as the effective pore length and surface area can be deduced from techniques such as X-ray microtomography *(see Section 2.1.5)*, SEM (*see Section 2.1.6*) and thin-section image analysis and can be used to predict flow properties of a porous material.

The prediction of permeability is complex and often it is assumed that all the pores are cylindrical in shape and that they are all interconnected, the liquid flow can be represented by Hagen-Poiseuille flow, and the Hagen-Poiseuille permeability K_p can be derived using Equation 2.5:

$$K_p = \frac{\Delta p_0 d^2}{32\tau^2} \qquad 2.5$$

where Δp_0 is the pressure difference across medium, d is the pore diameter and τ is the tortuosity.

The prediction of the permeability of sandstone was attempted from a stereological study of the pore space by Koplik *et al.* (1984). The method involved the analysis of SEM images in terms of the path length, path distances and geometrical factors. The method is of limited use for reliable permeability predictions since the results can differ by an order of magnitude from those obtained experimentally. It is difficult to determine whether a pore space may become a channel or a dead end from a 2-dimensional image. It must also be kept in mind that many naturally occurring porous media are heterogeneous and anisotropic, which are properties that cannot be identified from a 2-dimensional image.

Wu *et al.* (2006) used a method of modelling thin-sections of material to form a 3-dimensional structure from which predictions of single phase permeability were derived. The method involved creating reconstructions of a heterogeneous porous medium using a Markov

Chain Monte Carlo (MCMC) simulation. The reconstructed pore scale models were used as direct input for flow simulations, which allowed computation of transport properties, such as permeability using a Lattice–Botlzmann method. Okabe & Blunt (2004) used thin-section images of sandstone to provide multiple-point statistics, which described the statistical relation between multiple spatial locations and use the probability of occurrence of particular patterns. Assuming that the medium was isotropic, a 3-dimensional image could be generated that preserved typical patterns of the void space seen in the thin-sections. The permeabilities of the statistical representations of porous medium were computed using the Lattice-Boltzmann method. The calculated permeabilities were similar to the measured values. Solymar & Fabriciu (1999), Xu & Yu, (2008) and Pape *et al.* (2000) used the Carman-Kozeny relationship for estimating the bulk permeability from porosity and specific surface determined from image analysis. The Carman-Kozeny equation is based on a capillary bundle model which relates permeability to porosity, tortuosity, and the pore radius. Permeability can be modelled using the Kozeny Equation 2.6:

$$k = \frac{1}{c}\frac{(1-\varepsilon)^3}{S_s} \qquad 2.6$$

where k is the permeability, c is the Carman-Kozeny constant (noting that Heijs & Lowe (1995) give c=5), ε is the porosity and S_s the specific surface area. The specific surface areas of the samples were calculated using a relationship presented by Wong *et al.* (2006):

$$S_s = \frac{4}{\pi}\frac{\Sigma S_c}{\Sigma A_p} \qquad 2.7$$

where S_c is the measured pore perimeter of each image and A_p is the measured pore area. The equivalent spherical pore diameter d could also be predicted using Equation 2.8 (Solymar & Fabriciu, 1999):

$$d = \frac{6}{S_s} = \frac{3\pi}{2S_c} \qquad 2.8$$

2.1.6 X-ray tomography

X-ray computed tomography can be used to obtain non-destructive high resolution 3-dimensional images of the interior of objects. 3-dimensional images are obtained by reconstructing cross sections of an object by measuring the attenuation of X-rays that pass through it (University of Adelaide, 2005). X-ray computed tomography uses a series of 2-dimensional images to generate a 3-dimensional tomographic image of the structural density within the material of interest and uses multiple radiographic images to distinguish variations in 3-dimensional structural density. If a series of 2-dimensional radiographs are recorded as the sample rotates, with the use of an appropriate transform, a computer can process the radiographs to generate a 3-dimensional image of the material. Each data point within these 3-dimensional images is called a "voxel" (Ribia *et al.* 2008). The sample is stepped through a narrow X-ray beam and X-ray attenuation is recorded at each step. The sample is rotated slightly and the process is repeated. A 2-dimensional X-ray attenuation map from the

attenuation data is then acquired. The technique is useful for characterisation of porous solids as it offers visual information about the effective pore lengths and it is possible to see the extent of the tortuosity of the samples. X-ray microtomographs have been extensively studied to determine the pore space morphology and give estimations of flow properties by Altman *et al.* (2005), Auzerais *et al.* (1996), Coker & Torquato (1996), Coles *et al.* (1998), Schwartza *et al.* (1994) and Bentz *et al*. (2000).

2.1.7 Electron microscopy for imaging porous solids

Electron microscopy techniques provide a considerably higher resolution image than optical microscopy and allow a greater depth of focus. For this reason the electron microscope can produce images that are good representations of a 3-dimensional sample. There are two types of electron microscopes: scanning and transmission. Scanning electron microscopy (SEM) is capable of high resolution imaging of surfaces. It is possible to acquire images of good resolution using back scatter detector of an SEM. Solymar & Fabriciu (1999) show that observation of a simple distinction between solid particles and pores at macro and micro scale are possible using SEM. The method works in the following way: An incident beam of electrons is passed over the surface of a sample in a scanning beam. Electrons are reflected off the sample surface which has been previously coated with a metal or carbon if the sample is not electrically conducting. The electron reflection beams are focused on a screen and form an image of the sample surface. This technique can give detailed images of all materials that are stable in high vacuum. The main advantages of SEM are the large depth of focus, which creates images of irregular surfaces, and the large magnification range. Transmission electron

microscopy (TEM) is similar to SEM but instead of monitoring the reflected high energy electrons, the image is formed from electrons which have been transmitted through the sample. TEM is mainly used to show structures inside an object and requires that the sample is extremely thin to allow the transmission of the electrons so its use for characterising porous solids is limited.

2.1.8 Liquid metal penetration and solidification

In a manner similar to that used in mercury porosimetry (see *Section 2.3.1* below), a molten metal can be forced under pressure into the pores of a porous medium. However, in this case and in contrast to the mercury porosimetry technique, the metal solidifies *in situ* in the pores and the pore structure can be visualised using X-radiography. This gives a clear image of the accessible pores and the method is therefore complementary to methods such as SEM as described in the previous *Section.* Application of this methodology to the study of the pore structure of nuclear graphite is described by Hewitt & Sharratt (1962) and Hewitt (1967); in this work, it was found possible to obtain 3-dimensional images of the pore structure by taking X-radiographs at two different angles.

2.2 Gaseous transport in porous solids

2.2.1 Background to gaseous transport in porous media

Permeability is governed by Darcy's Law (Equation 2.2) which is valid if the fluid flow takes place by laminar flow (Lafhaj *et al.,* 2002) and if the flowing fluid is a single-phase medium. The rate of fluid flow through the a porous medium is directly proportional to the applied pressure gradient. Gas flow in porous media differs from liquid flow in two important respects. The first difference is that a gaseous phase must be treated as compressible which means that, though Darcy's law can be applied locally to relate fluid velocity and pressure gradient, the velocity will actually change along the flow path and this must be taken into account. The other factor which needs to be taken into account (particularly for low pressures) is that of "slip" between the wall and the flowing gas stream. The theory of slip was derived in the classical work of Millikan (1923) and the application of this theory to porous media is discussed, for example, by Hewitt (1967) (see also Hawtin *et al.,* 1967). More recent work in this area includes that of Biloe & Mauran, (2003) and others. The difference between permeabilities to gas and liquid because of the slip effects was recognised in early work by Klinkenberg (1951) and the phenomenon is often known as the "Klinkenberg effect". Slip is necssary to achieve the rate of transport of momentum to the wall (i.e. the wall shear sress) which is dictated by the pressure gradient. For gases, this term is significant and must often be included in the equations for gaseous transport. It is instructive to consider first the case of a single capillary of diameter d. Here, the mean gas velocity u at a position along the tube where the local pressure is p is given by (Hewitt, 1964, 1967):

$$u = -\frac{\pi d}{16}\frac{\bar{v}}{p}\frac{dp}{dz} - \frac{d^2}{32\mu}\frac{dp}{dz} \qquad 2.9$$

where $\bar{v}$ is the mean molecular velocity of the gas which is given by:

$$\bar{v} = \sqrt{\frac{8RT}{M}} \qquad 2.10$$

where R is the universal gas constant, T the absolute temperature and M the molecular weight of the transporting species. In Equation 2.9, the first term represents the effect of slip and the second term represents the viscous flow; when the slip is negligible (as is usually the case for liquid flows) then Equation 2.9 reduces to the Hagen-Poiseuille equation (Equation 2.5 above). The value of u changes as the gas density changes with changes of pressure as the gas flows through the medium. However, the *mass flux* of the gas which is the product of velocity u and density ρ remains constant. Since the temperature is assumed constant, and density is proportional to pressure, the product up is constant and it follows from Equation 2.9 that:

$$up = -\left(\frac{d^2}{32\mu} + \frac{\pi d}{16}\bar{v}\right)\frac{dp}{dz} = constant \qquad 2.11$$

Integrating Equation 2.11 with the limits $p = p_1$ at $z = 0$ and $p = p_2$ at $z = L$ gives:

$$u_1 p_1 L = \frac{d^2}{32\mu}\frac{(p_2^2 - p_1^2)}{2} + \frac{\pi d}{16}\bar{v}(p_2 - p_1) \qquad 2.12$$

Substituing $(p_2 + p_1)/2 = p_m$ and $(p_2 - p_1) = \Delta p$ Equation 2.12 reduces to:

$$\frac{u_1 p_1 L}{\Delta p} = \frac{d^2}{32\mu} p_m + \frac{\pi d}{16}\bar{v} \qquad 2.13$$

An equation analogous to Equation 2.9 is given for porous media by Carman (1956) as follows:

$$K = \frac{Q p_0 L}{\Delta p A} = \frac{k}{\mu} p_m + \frac{4}{3} K_0 \sqrt{\frac{8RT}{\pi M}} \qquad 2.14$$

where K is the permeability coefficient, Q is the volumetric flowrate, p_0 is the pressure at which Q is measured, Δp is the pressure difference across the sample, k is the viscous permeability (analogous to $d^2/32$ for the single capillary case – see Equation 2.13), μ is the gas viscosity, $4K_0/3$ = slip coefficient (analogous to $\pi d/16$ for the single capillary case – see Equation 2.13. The origin of the use of the factor 4/3 is obscure but this factor is retained here for consistency with other publications). The relationship between K and p_m is linear

with gradient $\frac{k}{\mu}$ and intercept $\frac{4}{3} K_0 \sqrt{\frac{8RT}{\pi M}}$, as is illustrated in Figure 2-1.

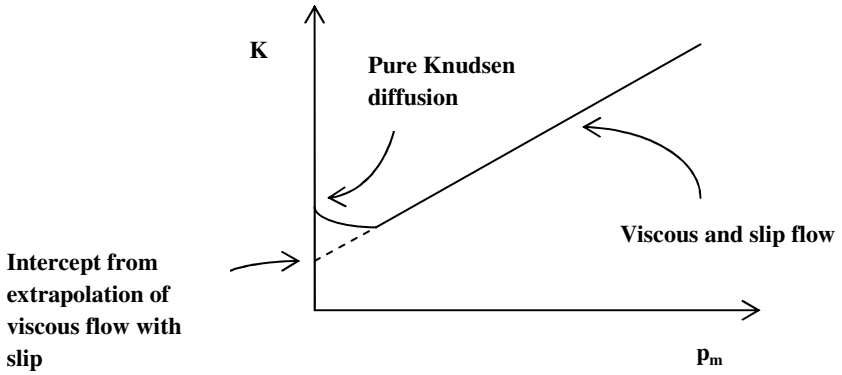


Figure 2-1: Schematic diagram of the extrapolation of the Knudsen diffusion coefficient from the linear viscous permeability

At very low pressures, the mean free path of the gas molecules becomes greater than the pore diameter. In this case, viscosity no longer influences the flow since gas molecules no longer collide with each other, only with the pore walls. In this region, the transport mechanism is known as *free molecule flow* or *Knudsen diffusion* (Evans & Watson, 1961, Adzumi, 1937 and Dees *et al.*, 1980). At very low mean pressures, where flow occurs purely by Knudsen diffusion, the permeability coefficient may be higher than the extrapolated slip coefficient value as shown in Figure 2.1.

2.2.2 Investigation of turbulent flow through porous media

In the flow of a fluid in a pipe, if the flowrate is increased above a certain transition point, the flow becomes unstable as randomly distributed local eddies are formed; this condition is described as 'turbulent'. Eddies dissipate kinetic energy from the fluid motion in the form of heat and as a result, increase the resistance to flow. In porous solids with curved pores, the onset of eddy formation occurs at fluid velocities well below that required for turbulent flow in straight cylindrical pores. The inertial resistance due to eddy formation is dependent on the kinetic energy per unit volume of the fluid and therefore proportional to (ρu^2) and assuming that the turbulent resistance can be superimposed on the resistance due to viscosity and that the effect of slip can be ignored, the pressure drop per unit length is given by Equation 2.15 and 2.16, as follows:

$$\frac{dp}{dz} = au + b\rho u^2 \qquad 2.15$$

$$\frac{1}{u}\frac{dp}{dz} = \frac{\mu}{k} + b\rho u \qquad 2.16$$

where $a = \frac{\mu}{k}$, k is the viscous permeability coefficient, u is the superficial velocity, b is the turbulent term and ρ is the fluid density. For the isothermal flow of gases the superficial velocity $u = \frac{G}{\rho}$, where G is the mass flux or "mass velocity". Since, from the gas law,

$\rho = pM / RT$ then Equation 2.16 can be integrated (Collins, 1961 and Carman, 1956) to give the following relationship:

$$\frac{\left(p_1^{\,2} - p_2^{\,2}\right)M}{2RTLG} = \frac{\mu}{k} + bG \qquad 2.17$$

Equation 2.17 may be simplified by defining C as shown in Equation 2.18:

$$C = \frac{\left(p_1^{\,2} - p_2^{\,2}\right)M}{2RTLG} \qquad 2.18$$

Thus, a plot of C versus G would be a straight line with intercept $\frac{\mu}{k}$ and slope b.

2.2.3 Steady-state diffusion through porous solids

Gas diffusivity is of interest in technologies including catalysis (Weisz & Schwartz, 1962, Satterfield & Cadle, 1968, Wakao & Smith, 1962 and Bokhoven & Hoogschagen, 1952) tissue engineering (Radisic *et al.,* 2005) and petroleum engineering (Al-Quraishi & Khairy, 2005 and Durlofsky & Gerritsen, 2005). Hewitt & Sharratt (1963, 1964) and Hewitt & Morgan (1964) use a method where nearly pure oxygen was passed over one end of a porous sample and nearly pure nitrogen over the other. The pressures at the two ends of the porous sample were maintained equal and the rate of diffusion of oxygen through the sample was determined by measuring the (low) concentration of oxygen in the efflux nitrogen. If the nitrogen flowrate over the nitrogen-rich end of the sample is Q_N (m^3/s) and the concentration

of oxygen in that stream is $N_{O,}$ (mol m^{-3}) then the molar transport rate n_O (mol s^{-1}) of oxygen through the medium is given by:

$$n_O = Q_N N_O \tag{2.19}$$

Defining an effective diffusion coefficient D_{eff} for the medium from the expression:

$$n_O = D_{eff} A \frac{\Delta N_O}{L} \tag{2.20}$$

where ΔN_O is the difference in oxygen concentration across the sample. Recognising that the concentration of oxygen is near zero at the nitrogen-rich end of the sample and that N_O is proportional to partial pressure at constant pressure, it also follows that:

$$u_{1O} p_{1O} = -D_{eff} \frac{\Delta p_O}{L} \tag{2.21}$$

where u_{1O} is the superficial velocity of oxygen entering the sample, p_{1O} the partial pressure of oxygen at the oxygen end and Δp_O the difference in partial pressure of the oxygen across the sample. Since $p_{1O} \approx -\Delta p_O$ it follows that:

$$D_{eff} = \frac{10^{-6} L Q_N c_O}{A} \tag{2.22}$$

where c_O is the concentration of oxygen (ppm by volume) on the nitrogen efflux stream. The ratio $r_{D=} D_{eff}/D_{AB}$, where D_{AB} is the equi-molar binary diffusion coefficient for the gas pair being considered (oxygen and nitrogen in the present case), would be expected to be a property of the porous medium and to be independent of the diffusing species.

The above equations do not take account of the effect of *net drift.* Even when the pressure is constant, equi-molar counter diffusion does not occur in a porous medium for gases of different molecular weight. If one assumed that the fluxes of the two gases were equal, then the transfers of momentum to the channel surfaces would imply that a pressure gradient must exist if the molecular weights were different. This problem has been considered, for instance, by Hewitt & Morgan (1964) and by Hewitt (1967). Hewitt & Morgan (1964) derive the following correction factor (Γ) by which the value of D_{eff}/D_{AB} calculated via Equation 2.22 must be multiplied to obtain a true value of the ratio, independent of the diffusing species:

$$\Gamma = \frac{1}{1-\sqrt{M_A / M_B}} \log \frac{1}{1-\sqrt{M_A / M_B}} \qquad 2.23$$

where M_A and M_B are the molecular weights of the diffusing species. In the experiments described in this thesis, which were carried out with oxygen and nitrogen, the correction needed would have been 3.3%. Since this is smaller than the expected experimental error, the net drift effect has, for convenience, been ignored.

The data for $r_D = D_{eff}/D_{AB}$ can be used to deduce information about the pore structure of the porous medium. The ratio r_D is less than unity because only part of the cross section (equivalent to the porosity ε_{eff}) is accessible to the diffusion process and because the pores have a length (L_{eff}) which may be greater by a factor τ (often referred to as the *tortuosity*) than the length of the sample, *L*. Thus (Weisz & Schwartz, 1962, Hewitt & Morgan, 1964, Youngquist, 1970):

$$r_D = \frac{D_{eff}}{D_{AB}} = \frac{\varepsilon_{eff}}{\tau^2} \qquad 2.24$$

Equation 2.24 allows the calculation of ε_{eff} if τ is known and *vice versa.* A possible way to determine tortuosity independently (and hence determine ε_{eff}) is through the use of transient diffusion measurements and this is discussed in the next section.

In the work described in this thesis, the emphasis is on normal or bulk diffusion in porous solids. However, as mentioned above, the type of diffusion that takes place in a porous material is affected by the relationship between the pore diameter and the mean free path of the gas molecules. For samples with pore diameters lower than 10^{-2} μm, Ali *et al*. (2001) show that only Knudsen diffusion will occur whereas above 1 μm, normal diffusion will occur, in between these values will see both diffusion mechanisms occurring simultaneously.

2.2.4 Transient diffusion through porous solids

Experiments on transient diffusion in porous media are described by Hewitt & Morgan (1964). These were also based on the constant pressure oxygen/nitrogen system and started with the sample full of nitrogen. At time $t = 0$ the pores of the sample were filled with nitrogen and the concentration of oxygen on the nitrogen side was zero. Oxygen was then passed over one end of the sample and its flowrate into the nitrogen-rich side determined by measuring the concentration of oxygen in the nitrogen efflux stream. It is convenient to express the results in terms of the ratio F of the oxygen flowrate to its final value. Hewitt & Morgan (1964) give the following expression for F:

$$F = 1 + 2\sum_{n=1}^{\infty} \cos n\pi \exp\left(-\frac{D_{AB}\pi^2 t}{L_{eff}^2}\right) \qquad 2.25$$

Equation 2.25 can be fitted to experimental data for F versus t by adjusting L_{eff}. The best fit value for L_{eff} can be used together with the measured value of r_D in the estimation of ε_{eff} from Equation 2.24.

2.2.5 Measurement of gas permeability

The measurement of gas permeability requires the measurement of pressure difference across the sample and the measurement of the flowrate of gas through it. Two alternative methods have been used:

1. Steady state methods involving measurement of the flowrate of the gas using some form of gas flow meter in series with the porous sample coupled with the determination of the pressure drop across the sample.
2. Pseudo transient methods in which the gas pressure upstream of the sample is maintained constant and the flowrate determined by observing the rate of pressure rise in a known sealed volume downstream of the sample.

Methods in the first category were applied by Baraka-Lokmane (2002), Biloe & Mauran (2003), Lafhaj *et al.* (2002) and Miguel & Serrenho (2007). Baraka-Lokmane (2002) determined the gas permeability of fractured sandstones using air. The pressure difference across the sample and volumetric flowrate of air were measured and the permeability was determined from Darcy's Law. Sandstone permeabilities varied from 30 – 180 mD. Lafhaj *et al.* (2002) carried out experimental studies of gas permeability on mortar. Again, the technique required the measurement of the volumetric flowrate of the gas through the sample when a constant single pressure was applied at one end. Biloe & Mauran (2003) used a similar method to measure the permeability of porous graphite using nitrogen and a method for evaluating the Knudsen contributions to flow. Laminar flow measurements were carried out by Miguel & Serrenho (2007), where the helium and air flowrate through porous sand and a woven fibrous material was determined by measurement of the pressure drop through porous material. They also showed for lower permeability samples, that flow is governed by free molecular flow so is dependent on the gas used.

In a gas pressure rise technique, one side of the sample is maintained at a very low

pressure, using a vacuum system; gas from the other (higher pressure) side of the sample flows through the pores of the material to the low pressure side, where it passes through a vessel of known volume and from this vessel through a valve and into the vacuum pump system. The measurement is actuated by closing the valve between the vessel and the vacuum system. The subsequent rise in pressure is monitored; the pressure on the outlet side increases with time but remains small compared to that on the high pressure side.

If the pressure on the high pressure side of the sample is p_1 and that on the vacuum side is p_2, the rate of change of pressure-rise on the low pressure side will be $\frac{dp_2}{dt}$. The pressure-rise technique works on the basis that the pressure gradient Δp across the sample is effectively p_1 if it is assumed that $p_2 \approx 0$ as $p_1 >> p_2$, therefore, the mean pressure is $p_m = p_1/2$. If the volumetric flowrate of gas on the low pressure side is Q_2 at a pressure p_2, the relationship in Equation 2.26 applies:

$$Q_2 p_2 = V \frac{dp_2}{dt} \qquad 2.26$$

where V is the volume of the outlet vessel. Since $Qp_0 = Q_2p_2$, substitution of Equation 2.26 into Equation 2.1 gives the following relationship:

$$K = \frac{V\left(dp_2 / dt\right)L}{p_1 A} \qquad 2.27$$

and the linear relationship between K and p_m shown in Equation 2.28 applies:

$$\frac{V\left(dp_2/dt\right)L}{p_1 A} = \frac{k}{\mu} p_m + \frac{4}{3} K_0 \sqrt{\frac{8RT}{\pi M}} \qquad 2.28$$

where V is the known volume of the vessel, L and A are the length and cross-sectional area of the sample. If values of K are measured at various mean pressures, a linear plot of K vs. p_m has the gradient $\frac{k}{\mu}$ from which k can be easily derived. The slip coefficient K_0 is determined from the extrapolated intercept.

The pressure rise method can also be applied to flows influenced by turbulence (see *Section 2.2.2* above). The mass flux G can be estimated directly from the measurements since:

$$G = \rho_2 \frac{Q_2}{A} = Q_2 p_2 \frac{M}{RTA} \qquad 2.29$$

and since $Q_2 p_2 = V \frac{dp_2}{dt}$:

$$G = V\left(\frac{dp_2}{dt}\right)\frac{M}{RTA} \qquad 2.30$$

Substitution of Equation 2.30 into Equation 2.17 gives the linear relationship shown by Equation 2.31 and a plot of C vs. $V\left(\frac{dp_2}{dt}\right)$ will have a gradient $\frac{bM}{RTA}$ and intercept $\frac{\mu}{k}$.

$$C = \frac{\mu}{k} + V\left(\frac{dp_2}{dt}\right)\frac{bM}{RTA} \qquad 2.31$$

To simplify C, from Equation 2.18 and Equation 2.27:

$$C = \frac{\left(p_1^{\,2} - p_2^{\,2}\right)}{2Kp_1} \qquad 2.32$$

and assuming that $\left(p_1^{\,2} - p_2^{\,2}\right) \cong p_1^{\,2}$, C can be defined as shown in Equation 2.33.

$$C = \frac{p_1}{2K} = \frac{p_m}{K} \qquad 2.33$$

If turbulence is occurring, the plot of C vs. $V\left(\frac{dp_2}{dt}\right)$ will be linear.

Thus, the gas pressure rise technique can be used to determine the viscous, slip and turbulent contributions to permeability and offers the advantage of the ability to evaluate samples with a wide range of permeabilities. By reducing the outlet volume, samples with viscous

permeabilities in the milli-Darcy scale can be evaluated and similarly by using a larger volume vessel, higher permeability samples are easily measured.

The pressure rise method for the determination of permeability has been widely applied. An early use of the method was that of Barrer & Grove (1951) and the technique was used extensively in studies of permeability of graphite by Hewitt and co-workers (Hewitt, 1961, Hewitt & Lacey, 1963, Hewitt, 1964, Hewitt, 1966 and Hewitt *et al.*, 1966).

2.2.6 Diffusion measurements

Experimental methods for the determination of the effective diffusion coefficient D_{eff} have been described by Weisz & Schwartz (1962), Youngquist (1970), Satterfield & Cadle (1968), Wakao & Smith (1962), Bokhoven & Hoogschagen (1952) and Ferguson & Schumacher (1927). A series of studies of gaseous diffusion in graphite were reported by Hewitt and co-workers (Hewitt & Morgan, 1961, Hewitt & Sharratt, Hewitt & Sharratt, 1963a, 1963b, Hewitt & Morgan, 1964, Hewitt & Sharratt, 1964, Hewitt, 1967, Hewitt *et al.*, 1969, 1970) (discussed in *Section 2.2.3*).

Early designs of equipment for measuring the diffusion of gases and vapours by Ferguson & Schumacher (1927) involved a membrane of the sample being placed between two chambers, only one of which containing the diffusing substance. The rate at which the diffusing substance passed from one chamber to the other can be measured by determining the amount of the diffused gas on the other side of the sample with a simple gas analyser. The design was

proved to be an efficient apparatus for diffusion measurements, although required the use of a mercury seal to avoid any fluid leakage. Weisz (1957) and Youngquist (1970) used a method where the solid sample was mounted in a way to separate two pure gas flow systems, hydrogen flowed across one exposed face and nitrogen across the other. Hydrogen in the nitrogen stream diffusing through the solid was measured and the diffusivity was determined from the concentration of hydrogen, the nitrogen flowrate and the sample dimensions.

In the work described in this thesis, an experimental design based on that used by Hewitt and co-workers was adopted. This is described in more detail in Chapter 3; briefly, it involved flowing oxygen and nitrogen across the two ends of the sample respectively, with the two gases being at equal pressure. The rate of flow of oxygen through the sample was determined by measuring the (low) concentration of oxygen in the nitrogen efflux stream. However, in the present work, in contrast to the approach taken by Hewitt and co-workers, an *integrated* apparatus was used which allowed both permeability and diffusion (including transient diffusion) measurements to be made in the same rig.

2.3 Mercury penetration of porous solids

Mercury has the unique property, because of its high surface tension and high contact angle, of only penetrating those pores whose diameter is sufficiently high to allow penetration at the given pressure of the mercury. As the pressure of the mercury increases, then the size of pore penetrated decreases. This property is the basis of the widely-used mercury porosimetry technique and this method will be described *Section 2.3.1* below. However, advantage can

also be taken of this progressive penetration in applying two other (much less widely used) methods. The first of these (*mercury permeability*) involves measurement of the permeability of the porous solid to the mercury in place in the medium at the applied pressure. Clearly, if all the pores in the medium are full of mercury, then the measured permeability would be the same as that for a wetting liquid or for a gas which also filled the pores in the medium. By measuring the permeability as a function of applied pressure, a direct indication of the contributions to permeability made by pores of the sizes penetrated is obtained. Work on this technique is reviewed in *Section 2.3.2*. Similarly, the electrical conductivity of a medium being penetrated by mercury can be measured at various applied pressure levels. Electrical conductivity is directly analogous to diffusivity and, by measuring the electrical conductivity as a function of applied pressure, the contributions made to diffusion by the various pore groups can be assessed. This *mercury conductivity* technique is discussed in *Section 2.3.3*. Finally, in *Section 2.3.4*, an overall assessment of these mercury penetration techniques is given.

2.3.1 Mercury porosimetry

Pore structure analysis by mercury porosimetry is applicable when the material in question is sufficiently rigid to withstand relatively high compressive forces and does not amalgamate with mercury (Cosentino & Oliveira, 2000). Mercury porosimetry was recognised by Chatzis *et al.* (1991) as one of the most important methods available for the analysis of the structure of porous media. Brakel *et al*. (1981) and Garboczi (1991) describe the principle of the technique as based on the fact that mercury behaves as a non-wetting liquid towards most

substances. As a result, mercury does not penetrate pore openings and cracks in a sample unless an external pressure is applied. The basic mercury porosimetry experiment consists of a gradual intrusion of mercury into the evacuated porous sample by increasing an applied pressure in small increments. With each applied pressure increment, mercury is pushed through smaller pore throats and the pores are filled with mercury—measurements of the pressure and the corresponding volume of mercury entering the sample are taken. Figure 2.2 represents schematically the mercury intrusion method. As the applied pressure is increases, mercury penetrates pores through smaller pore throats.

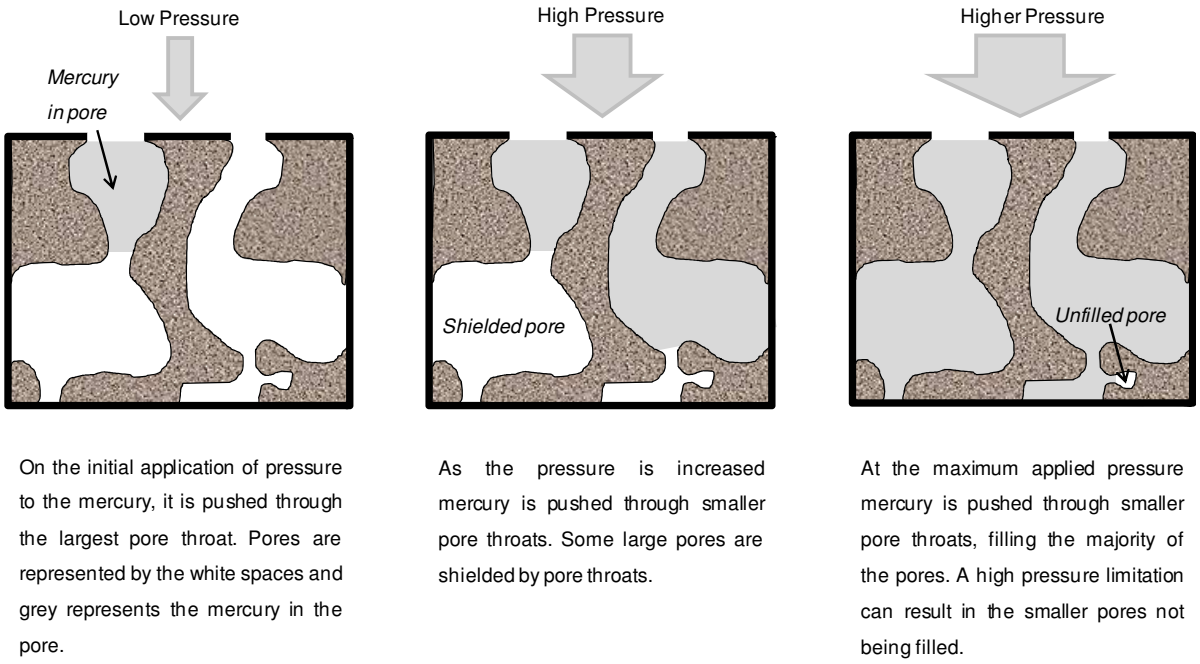


Figure 2-2: Schematic representation of the mercury porosimetry method showing the increase of mercury penetration of the pores as the applied pressure is increased

The pore size can be related to the applied pressure using the Young-Laplace relationship (Equation 2.34) which was presented by Washburn (1921) and assumes a local cylindrical pore geometry:

$$p = \frac{-2\gamma \cos\theta}{r} \qquad 2.34$$

where p *i*s the applied pressure, γ is the mercury surface tension, θ is the contact angle between mercury and solid and r is the radius of the pore. It is usually assumed that the surface tension of mercury and the contact angle between the solid and the mercury are constant. Ishizaki *et al*. (1998) have shown that the surface tension of mercury is 484 mN m^{-1} and the contact angle is in the range 130° to 140° for most solids. It has been shown, however, by Kloubek (1981) that both of these values may vary under certain conditions and lead to inaccurate values of pore size. The main contributing factors that affect the surface tension and contact angle of mercury have been described by Edler & Rigby (2002) as the pore size itself, the nature of the surface and whether the mercury is in advancing or receding motion.

The limitations of the technique (in addition to the uncertainty relating to values of the mercury properties) include the assumption that all pores are circular in cross section; experimental error due to high pressure limitations which may result in small pores not being penetrated; and, the errors caused by shielding effects of smaller pore throats and boundary effects of smaller pores as shown by Amthor & Kopaska-Merkel (1988) and is illustrated in Figure 2-2.

2.3.2 Mercury permeability

The mercury permeability method had its origins at the UKAEA Harwell Laboratory in the 1960's and was focussed on its application to the study of (porous) nuclear grade graphite. The specific methodology had its origins in studies of the containment of another liquid metal (zinc) in graphite crucibles (Hewitt, 1961, 1962). Hewitt (1960) describes the basic mercury permeability methodology and an overview of this and other liquid metal penetration techniques is given by Hewitt (1967).

Since mercury is a non-wetting liquid and thus requires the application of a pressure to force it into the pores of a material, the basis of the mercury permeability technique is similar to that of the mercury porosimetry technique and, indeed, the first step is to impregnate the pores at known pressure (corresponding to a given pore size). However, the mercury permeability method goes a step further by then applying a pressure difference (small compared to the previously applied pressure) across the sample and measuring the flowrate of mercury through the sample and hence the permeability to mercury. By repeating the experiment at a series of (increasing) applied pressures, a curve of mercury permeability against applied pressure is generated. In the original Harwell work, mercury porosimetry measurements on similar samples were made and this allowed (though indirectly) the mercury permeability to be related to the porosity penetrated at the given applied pressure (and, hence, penetrated pore size as calculated from Equation 2.34).

A diagram of the mercury-flow apparatus used in the original Harwell work is shown in Figure 2-3. The apparatus was first evacuated and then mercury was introduced so as to

establish contact between the mercury and the respective faces of the sample, with the mercury being at equal levels in the tubes above the respective sides of the sample as shown.

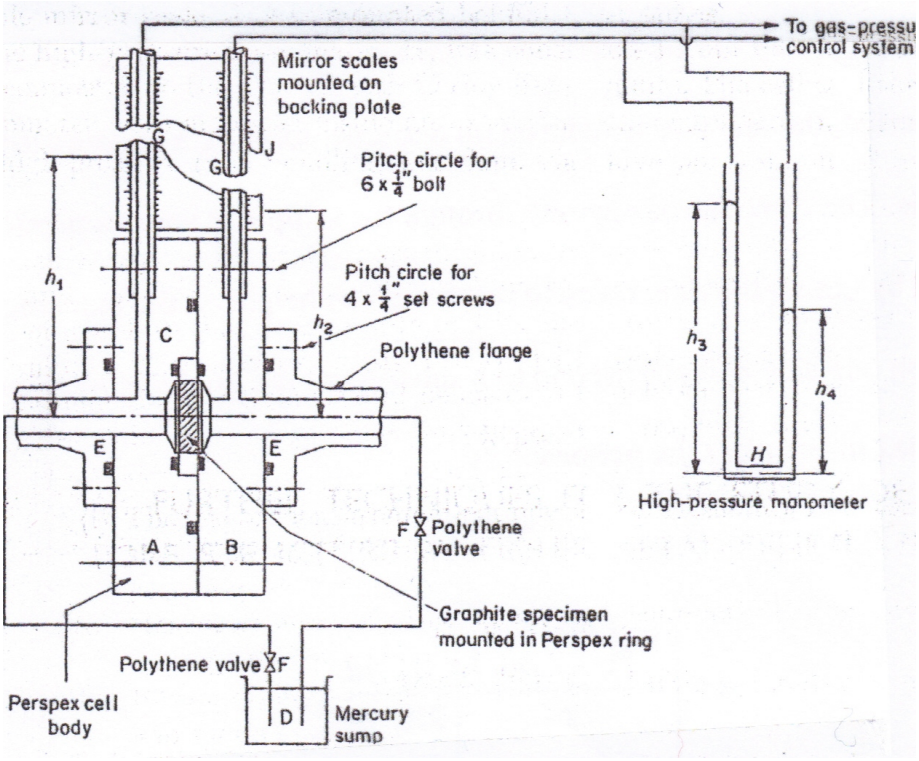


Figure 2-3: Diagram of mercury flow apparatus used by Hewitt (1967)

A known gas pressure was then applied above the mercury to force it into pores which could be penetrated at this applied pressure. When the sample was fully saturated, the pressure was reduced on one side, forming a pressure differential across the sample which was measured using a differential pressure manometer (see Figure 2.3). The flowrate of mercury under this differential pressure was measured by observing the changes in level in the tubes above the sample—the rise of mercury on one side will correspond to a subsequent fall on the other. The applied pressure was then increased in steps and the mercury permeability versus applied

pressure curve established, allowing the permeability to be related to porosity and pore size penetrated.

The mercury permeability can be calculated in the following way (Hewitt, 1960) (h_1, h_2, h_3 and h_4 are labelled in Figure 2-3), the pressure difference forcing the mercury through the material is given by Equation 2.35:

$$\Delta h = (h_1 - h_2) + (h_4 - h_3) \qquad 2.35$$

If $(h_4 - h_3)$ is fixed for the measurement, differentiation of Equation 2.35 gives Equation 2.36:

$$\frac{d(\Delta h)}{dt} = \frac{d(h_1 - h_2)}{dt} \qquad 2.36$$

If a volume, dV passes through the material from left to right, the fall in height h_1 will correspond to the rise in height h_2 with is equivalent to $\frac{dV}{A_1}$, where A_1 is the cross-sectional area of the tubes and can be expressed as shown in Equations 2.37 and 2.38:

$$dh_1 = dh_2 = \frac{-dV}{A_1} \text{ and } d(h_1 - h_2) = -2\frac{dV}{A_1} \qquad 2.37$$

$$\frac{dV}{dt} = \frac{A_1 d(h_1 - h_2)}{2dt} = \frac{A_1 d(\Delta h)}{2dt} \tag{2.38}$$

Applying Darcy's Law gives Equation 2.39 where A_2 is the cross-sectional area of the sample material:

$$\frac{dV}{dt} = uA_2 = \frac{A_2 k \Delta P}{\mu L} \text{ and } \Delta P = \rho g \Delta h \tag{2.39}$$

$$\frac{dV}{dt} = \frac{A_2 k \rho g \Delta h}{\mu L} \tag{2.40}$$

$$\frac{A_1 d(\Delta h)}{2dt} = \frac{A_2 k \rho g \Delta h}{\mu L} \tag{2.41}$$

$$k = \frac{d(\Delta h)}{dt} \frac{A_1}{2A_2} \frac{\mu L}{\rho g \Delta h} \tag{2.42}$$

After integrating for the limits $\begin{matrix} \Delta h = \Delta h_a \ at \ t = 0 \\ \Delta h = \Delta h_b \ at \ t = t \end{matrix}$, Equation 2.43 can be derived:

$$k = \left[\frac{\log\left(\Delta h_0 \middle/ \Delta h_t \right)}{t} \right] \frac{A_1}{2A_2} \frac{\mu L}{\rho g} \tag{2.43}$$

where k is the permeability of the porous sample, Δh is the change in height, t is the time taken for the height change, μ is the viscosity of mercury, ρ is the density of mercury, L is the length of sample and g is acceleration due to gravity.

Hewitt (1960, 1967) found that, for nuclear graphite, the mercury permeability approached that of the gas for a penetrated pore volume of only about a quarter of total porosity. This means that three quarters if the pore volume contributed little or nothing to the flow in this case. Since it addresses directly the flow capacity of the penetrated pores, the mercury permeability method provides useful new information about the flow behaviour in porous media. This technique has not been adopted subsequent to the original Harwell work.

2.3.3 Mercury conductivity

In the mercury conductivity method, the conductance of a sample penetrated by mercury at an ascending series of applied pressures is measured. The conductance process is directly analogous to the diffusion process. Thus, for a fully saturated medium, and where the medium itself is non-conducting, we can write (by analogy with Equation 2.24):

$$r_C = \frac{\sigma}{\sigma_o} = \frac{\varepsilon_{eff}}{\tau^2} \qquad 2.44$$

where r_C is the ratio of the conductivity of the saturated medium σ to the conductivity of the fluid saturating the medium σ_o. The conductivity of the saturated sample can be measured

by determining the current passing through the sample for a given voltage drop between the ends of the sample. Thus, from Ohm's Law as:

$$\sigma = \frac{L}{R_s A} = \frac{LI}{EA} \qquad 2.45$$

where L is the sample length, R_s is the resistance of the sample, A is the cross-sectional area of sample, I is the current flowing through fluid and E is the electrical potential difference (voltage).

If the fluid entering the medium is mercury, then Equation 2.44 will apply only if the pores are fully saturated with mercury at very high pressures. At low and intermediate pressures, the value of r_C will be lower; as in the case of permeability, this gives an opportunity of assessing the contribution of the various pore sizes to the conduction (and hence diffusion) process.

The mercury conductivity technique was explored at Harwell in the 1960's for the study nuclear graphite (Hewitt, 1960, 1967). The apparatus used is illustrated in Figure 2.4.

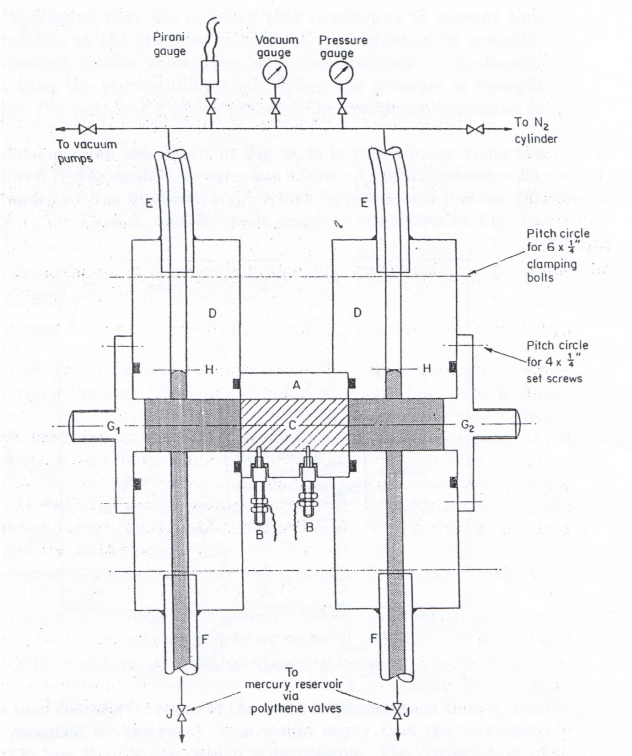


Figure 2-4: Diagram of the mercury conductivity cell used by Hewitt (1967)

Mercury was forced into the pores of the graphite samples contained in a conductivity cell (shown in Figure 2-4) using the technique discussed in *Section 3.2*. Current was passed through the cell through plugs G (shown in Figure 2-4) and the resistance between the electrodes B across the cell was measured with a Kelvin Bridge as a function of the total pressure. For low pressures, the conductivity was low (corresponding to that of the graphite) but increased with increasing applied pressure. The data could be interpreted to throw light on the contributions of the various sizes of pores to conductance (and hence diffusion) but the interpretation was difficult because the medium itself (graphite) was an electrical conductor.

Though there has been no further application of the mercury conductivity method since the 1960's Harwell work, the measurement of the conductivity of samples fully saturated with a conducting fluid (typically brine) has been quite widely applied (Archie, 1942, Wyllie & Spangler, 1952, Le Doussal, 1989, Tiab & Donaldson, 1996, and Ali *et al*., 2001). An empirical equation that links the electrical conductivity of a porous solid that's pore space is saturated with an electrically conducting fluid and the porosity was first proposed by Archie, 1942. The relationship is known as Archie's law and is shown in Equation 2.46:

$$\frac{\sigma_p}{\sigma_O} \propto s^n \qquad 2.46$$

where s is the conducting fluid saturation of the sample and n is the empirical parameter that varies with the lithology of the material and is reported by Koplik *et al.* (1984) as approximately 2.

This work has been used to throw light of the structure of porous media (for instance through the use of Equation 2.44).

2.3.4 Mercury penetration techniques: Overall assessment

The power of mercury porosimetry in examining the pore structure of porous media is well recognised and the technique is widely used with commercial apparatus being available from several sources. The extension of the technique to mercury permeability measurements and,

for non-conducting media, to mercury conductivity measurements is very promising, though it has not been implemented since the development of these methods in the 1960's at the Harwell laboratory in the UK. Moreover, it is important to stress that the methods are interdependent; for example, it would be difficult to interpret the mercury permeability measurements without information from mercury porosimetry. These considerations led to the concept, pursued in the present work, of *integrating* the three mercury penetration methods (porosimetry, permeability and conductivity) into a single apparatus. The development of this apparatus is described in Chapter 4 and the application of the methodology (in conjunction with gaseous transport measurements) to sandstones and polymer foams is described in Chapters 5 and 6 respectively.

CHAPTER 3

DEVELOPMENT OF AN INTEGTRATED APPARATUS FOR GAS PERMEABILITY AND DIFFUSION MEASUREMENTS

As will have been seen from the discussion in Chapter 2, the measurement of gas permeability and diffusivity in porous media is of great importance in itself and also as a means of gaining insights into the structure of the media. The understanding gained from such measurements can be augmented by extending the measurements to include transient diffusion and diffusion in the presence of a pressure gradient, as was also explained in Chapter 2. In the past, permeability and diffusion measurements have conventionally been made using different and separate apparatus. A major focus of the present work was to develop a new form of apparatus in which both permeability and diffusion measurements could be made, including transient diffusion and diffusion under the influence of a pressure gradient. In this Chapter, the design, construction and commissioning of this apparatus are discussed. The application of the apparatus to the study of porous rocks and polymer foams is discussed in Chapters 5 and 6, respectively.

In what follows, *Section 3.1* deals with sample preparation (which is generic for both the gaseous transport and the mercury penetration methods discussed in Chapter 4) and *Section 3.2* describes the design, construction and application of a prototype apparatus for gas permeability, this apparatus being a precursor to the integrated gaseous transport apparatus

described in *Section 3.3*. Finally, *Section 3.4* gives an overview if the progress made in this topic.

The gases used in all the experiments were oxygen free nitrogen (99.9% purity) and oxygen (99.5% purity) obtained from BOC Edwards Ltd., Crawley, UK.

3.1 Preparation of samples

Appropriate preparation of samples for permeability and related measurements is essential. In particular, it is important to ensure that the flows are restricted to one-dimensional ones between the inlet and outlet faces of the sample and that leaks round the edges of the sample are eliminated. Considerable attention was devoted to the development of a sample system which could be applied to both the gaseous transport studies (described in this Chapter) and to the mercury penetration studies (described in Chapter 4).

The porous solid cores were sealed with a non-permeable coating to eliminate any fluid leakage from the sample via cross-flow. This was achieved by coating the whole surface of the sample with a layer of epoxy resin, when fully cured the sample was set coaxially in an epoxy resin cylinder using a PTFE sample mould. A sample mould was prepared according to the diagram shown in Figure 3-1.

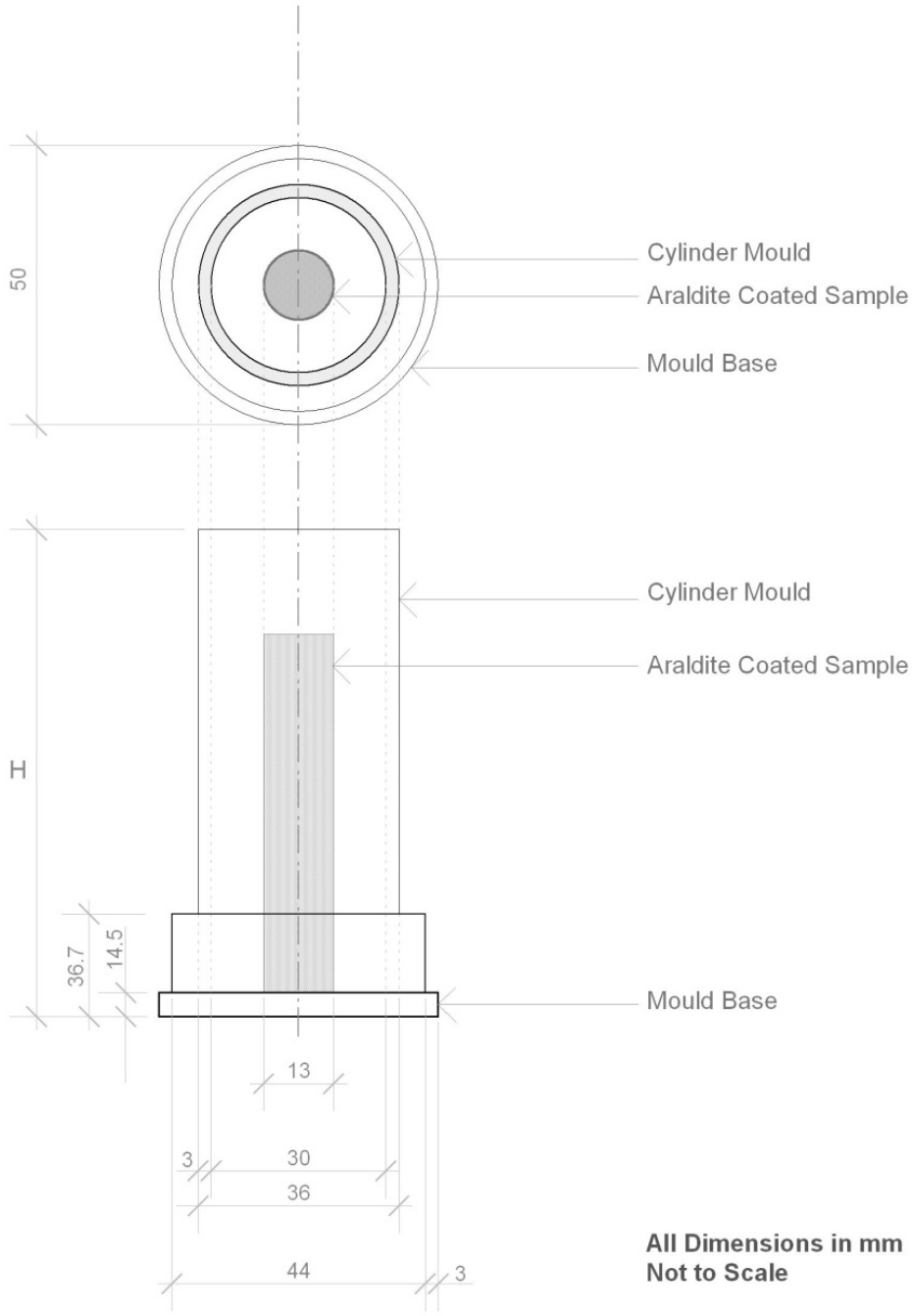


Figure 3-1: Dimensions of the sample mould for sealing porous solid samples

The sample cores were initially coated with *Araldite® Precision Adhesive* (RS Components Ltd. Corby, UK) and left to cure at room temperature. The coated cores were then inserted

into the sample holder in the mould base which was sprayed with a silicon release agent (*Silicone mould release spray,* Electrolube, RS Components Ltd., Corby, UK) and the mould cylinder was attached around it. A two-component epoxy adhesive, *Araldite® 2020* (RS Components Ltd., Corby, UK) and was poured into the mould cylinder around the sample and left at room temperature for 24 h to cure. Once coated and sealed, the core was machined at both ends to reveal the faces of the sample, a representation of the coated sample is shown in Figure 3-2.

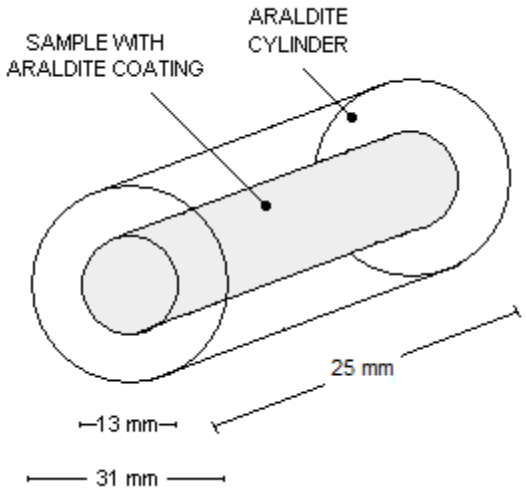


Figure 3-2: Dimensions of coated sample

3.2 Prototype apparatus for the measurement of gas permeability - design detail

A prototype apparatus was designed and constructed to evaluate the viability of the pressure-rise technique and ensure, before proceeding with the integrated apparatus described in Section 3.4, that the experimental set-up was practical for the measurement of gas flow

through porous solids. The apparatus is described in this *Section* as are the results of trial experiments carried out on sandstone (Samples R1, R2 and R3 – see Chapter 5 for details of sandstone samples).

A photograph of the apparatus is given in Figure 3-3 and a diagram in Figure 3-4. The apparatus consisted of a test cell in which the sample was mounted and an outlet system (including a vessel as shown) of known volume (1.28×10^{-4} m^3) to collect the permeating gas.

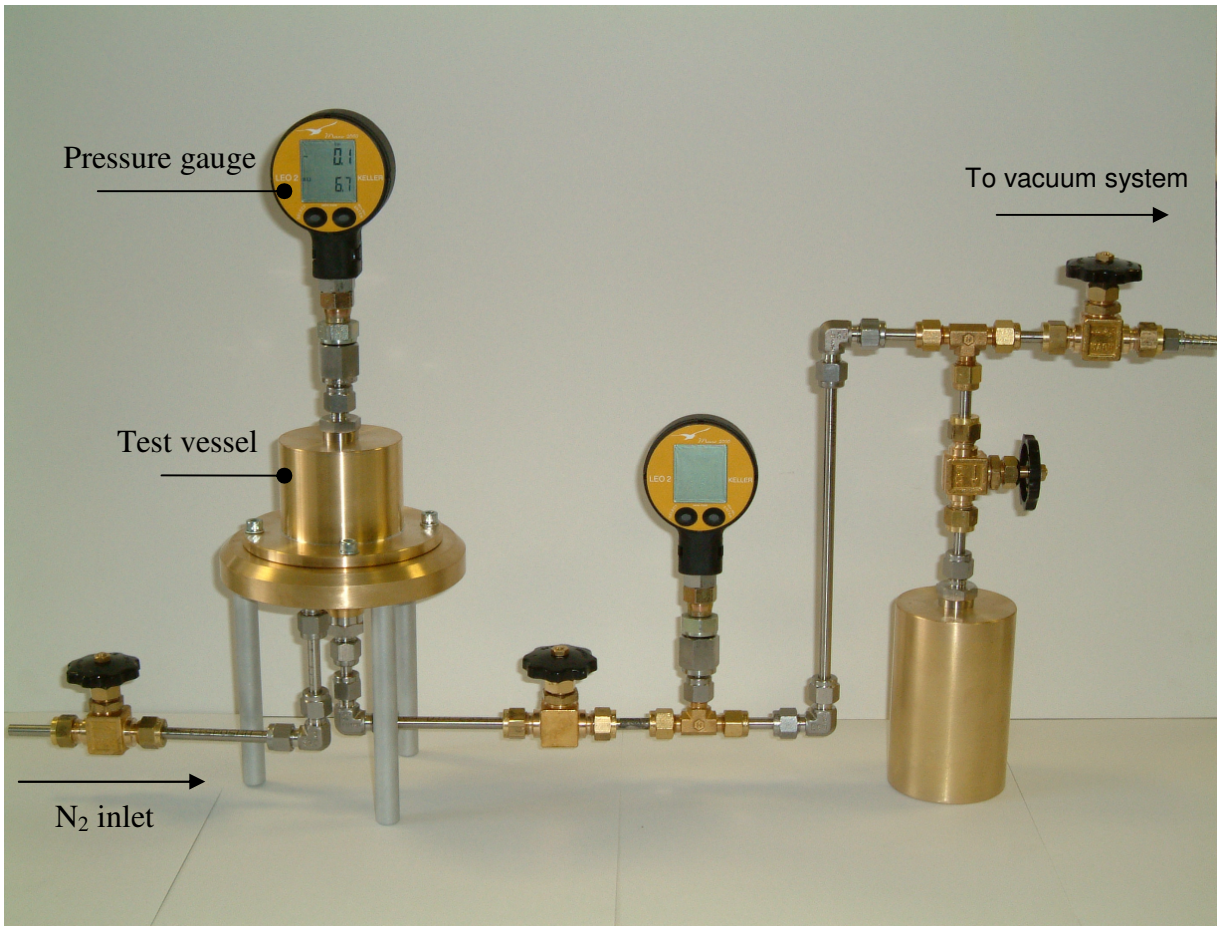


Figure 3-3: Photograph of primary gas permeability apparatus

The test cell was constructed from a disc of 20 mm thick brass with a groove cut into it to house the sample with a rubber O-ring seal which became effective when the outlet was evacuated. The disc had an open outlet underneath the sample space, to allow gas flow through the sample material. A brass lid could be tightly screwed to the brass disc creating a seal around the sample due to a second rubber O-ring seal. The second vessel was also constructed from brass and joints which were soldered to withstand internal pressures of 10^6 Pa. Connections and fittings were ¼ inch NPT and brass needle valves were used. Two pressure gauges (*Digital Manometer LEO 2* Keller (UK) Ltd., Dorchester, UK) were fitted for measurement of the test cell and outlet pressures and a supply of nitrogen with a pressure regulator was connected to the test vessel. A start-up and shut-down procedure for operation of the prototype apparatus is given in *Appendix I* which corresponds to the schematic in Figure 3-4.

A vacuum pump (*Model E-Lab-2 Vacuum Pump*, BOC Edwards Ltd., Crawley, UK) and vacuum system was used for evacuation. The vacuum system consisted of 1" diameter vacuum hoses and a vacuum trap, (both supplied by Leybold Vaccum UK Ltd., Chessington, UK).

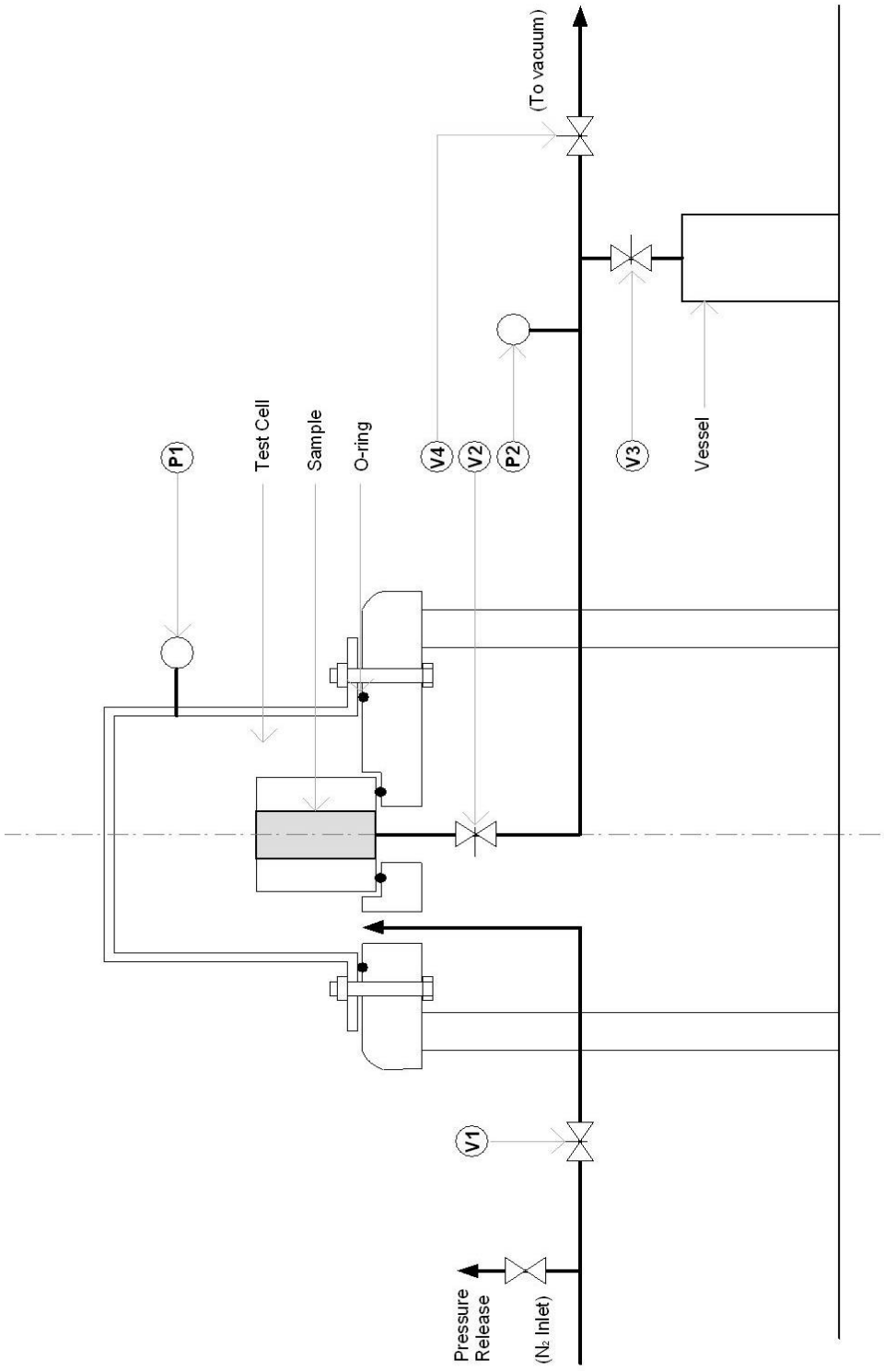


Figure 3-4: Schematic diagram of the test cell (around sample) and connections

3.2.1 Preliminary results of permeability measurements with the prototype apparatus

Three sandstone samples, R1, R2 and R3 were prepared as described in *Section 3.1* and were used in this preliminary investigation to test the viability of the pressure-rise method for the measurement of permeability and the operational procedure. The samples were sealed into the vessel and evacuated from the underside (for an illustration of the apparatus see Figure 3-4). Once a sufficiently low pressure was reached (approximately 10 Pa), nitrogen was allowed into the vessel at pressure $p_1 = 10^5$ Pa. Isolation of the vacuum system by closing valve V4 initiated the test. Gas flow through the sample into the outlet system (including the outlet vessel) continued at a rate close to that applying before the vacuum system was isolated and the rate at which the pressure (p_2) downstream of the sample increased with time was measured. The system was then evacuated again and the nitrogen was allowed to flow back into the vessel at an increased pressure, i.e. $p_1 = 1.5\times10^5$ Pa etc. Data collected were used to calculate the permeability coefficient K for the samples at the corresponding mean pressure p_m . Since $p_1 >> p_2$, $p_m \approx p_1/2$. They are presented in Figure 3-5.

The viscous permeability was determined from the gradient and the slip coefficient K_0 was found from the intercept. Sample R1 shows a trend with the largest gradient, indicating a high viscous permeability coefficient and Sample R3 has a very small gradient in comparison denoting a lower viscous permeability coefficient K. Similarly, it can be noted that the same pattern is true for the Knudsen coefficient terms K_0. The results are summarised in Table 3-1.

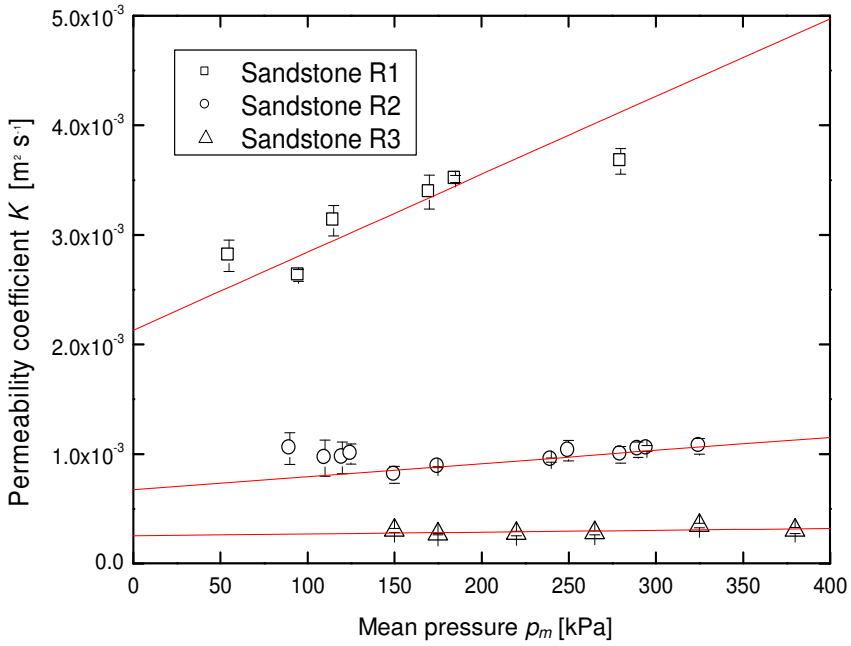


Figure 3-5: Permeability coefficient plot for sandstone permeability measurement in the prototype pressure-rise cell

The gas permeability was also measured using a Hassler air permeameter and the results were compared to measurements taken from the newly constructed pressure rise apparatus. Samples R1, R2 and R3 were contained in a Hassler sleeve with a confining pressure of 10 bar. A variable flowrate of air was applied to one face of the sample and the corresponding pressures on both the inlet and the gas outlet sides were measured on digital pressure gauges.

Analysis of the data required the measurement of the sample face surface area and length to allow the application of Darcy's Law which is given in Equation 3.1. To account for gas slippage at the wall of the pores, the Klinkenberg correction was used to determine the true

permeability. This required that the data was extrapolated on a plot of $1/p_m$ vs. k_g to $1/p_m = 0$. The intercept of the extrapolated data gives the equivalent permeability to that if the sample was 100% saturated with an unreactive liquid, or the true permeability. Figure 3-6 shows a plot of $1/p_m$ against k_g and has been used to determine the permeability according to Darcy's Law. It can be noted that Sample R1 has the highest permeability as the intercept is at approximately 123 mD. Sample R2 has a slightly lower permeability to air with a value of 36 mD and Sample R3 has the lowest value of 0.6 mD. Values of the equivalent permeability for each sample are presented in Table 3-1 along with permeability values obtained using the gas pressure rise apparatus.

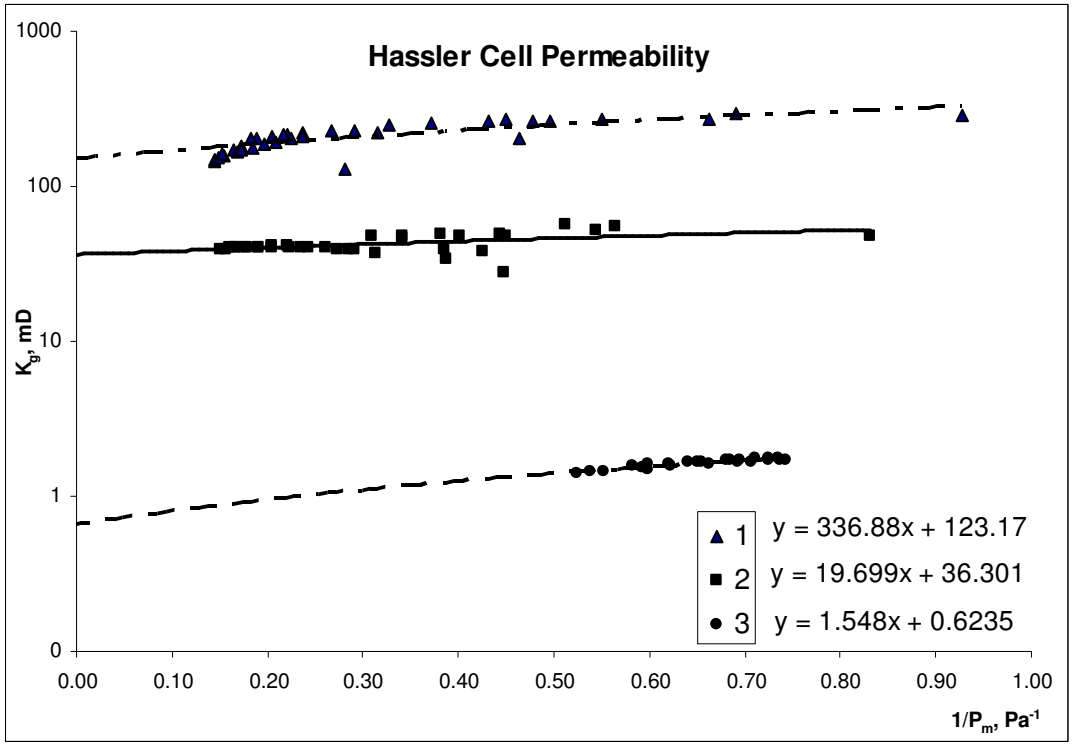


Figure 3-6: Permeability results from measurements obtained using the Hassler cell method

Comparisons of the values found from both pieces of apparatus are in good agreement indicating that the newly constructed gas pressure rise apparatus yields permeability measurements consistent with those of the existing Hassler apparatus.

Table 3-1: Results of permeability measurements

Sample	Permeability [mD]	
	Hassler	Pressure Rise
R1	123.0 ±15.3	118.0 ± 8.4
R2	36.3 ± 4.5	19.8 ± 2.6
R3	0.62 ± 0.1	2.8 ± 2.4

The prototype gas permeability apparatus performed satisfactorily in allowing determination of permeability and slip coefficients; the results obtained indicate that the method is viable and so a more robust version of the apparatus, integrated with a diffusion apparatus, was developed that could withstand higher gas pressures. This is discussed in *Section 3.3*.

3.3 Integrated apparatus for the measurement of gas permeability and diffusivity – design detail

The integrated apparatus for the measurement of gas permeability and diffusivity was designed to incorporate a system for the measurement of gas diffusivity with the previously designed gas permeability method. The integrated apparatus is a unique experimental set-up that enables measurement of both permeability and diffusivity of a single solid sample.

From the permeability measurements, the slip coefficient and viscous permeability can be determined and from gas diffusion measurements, information about the porosity, effective diffusion coefficient, pore tortuosity and effective pore length can be obtained. The design is discussed here together with the basic operating procedure. Start-up and shut-down procedures can be found in *Appendix II*. Figure 3-7 shows an illustration of the apparatus.

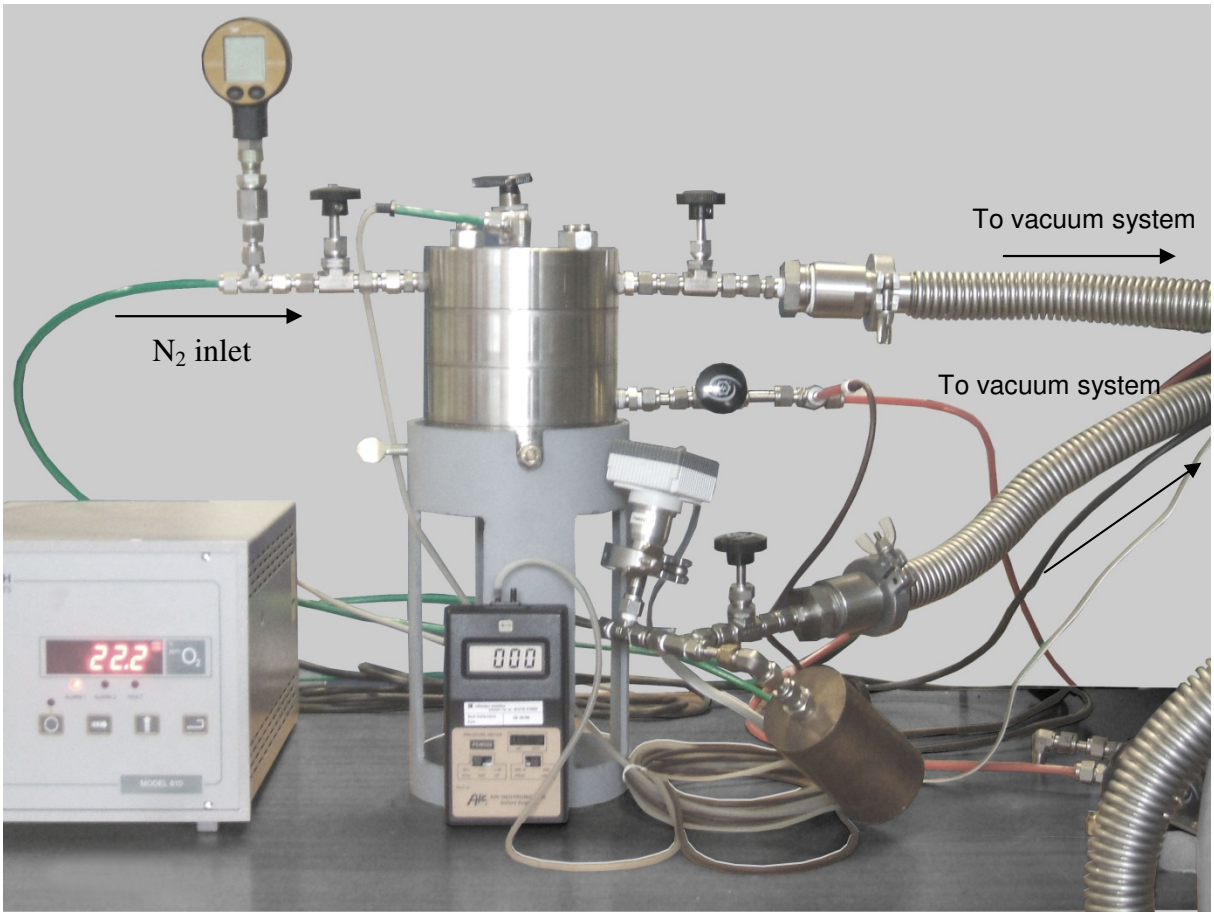


Figure 3-7: Photograph of the integrated gas permeability and diffusivity apparatus

The sample cell consisted of four stainless steel discs which were bolted together with four tie bolts as shown in Figure 3-8. Rubber O-ring seals were placed between each disc. The sample was held in between discs 2 and 3 with O-rings at either end to ensure no gas leakage around the edge of the sample. Disc 4 was secured to a base stand which elevated the cell from bench height for easy access to the nitrogen outlet. The discs had guide pins to ensure that the cell was assembled in the correct order. Disc 3 was placed onto disc 4 following the guide pins and the sample then fitted on top of the O-ring set in disc 3. Disc 2 was then placed on top of disc 3 and disc 1 on top of that. The tie bolts were threaded through all of

the discs and fastened with nuts on the top of the cell. With the sample sealed in the cell, the bolts were sufficiently tightened and the cell was then evacuated to 10 Pa before measurements commenced.

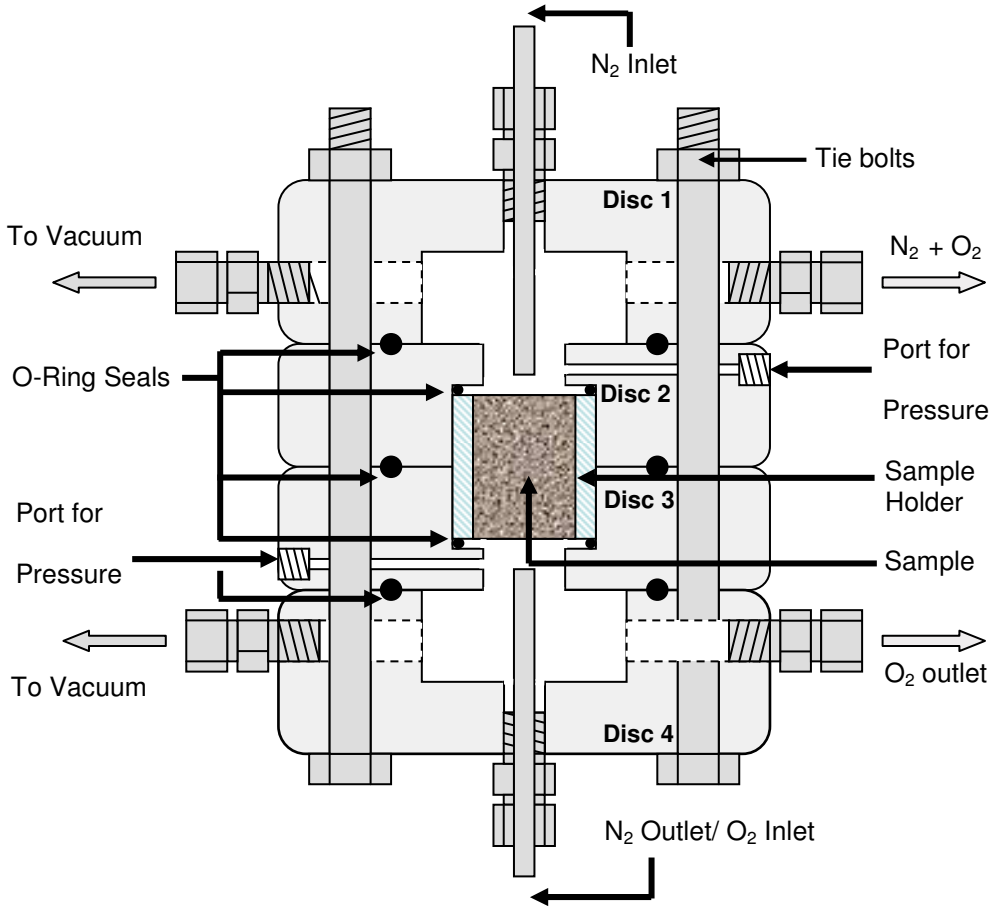


Figure 3-8: Detailed diagram of the sample cell of the gas permeability and diffusivity apparatus showing inlet and outlet points (not to scale)

3.3.1 Set-up for permeability measurements

Figure 3-8 shows the connections to the sample cell and Figure 3-9 is a schematic of the gas permeability cell set-up. The vacuum pump was connected to the cell via outlets V2 and V3

using 1" diameter vacuum hoses (Leybold Vaccum UK Ltd., Chessington, UK), and the pressure was monitored with a Pirani vacuum gauge P2 (*Pirani APG-M-NW16 with Active Pirani Gauge ADL Active Digital Controller*, Boc Edwards Ltd., Crawley, UK). Valves V1 and V4 were closed whilst the sample, cell and vessel were evacuated to a pressure of 10 Pa.

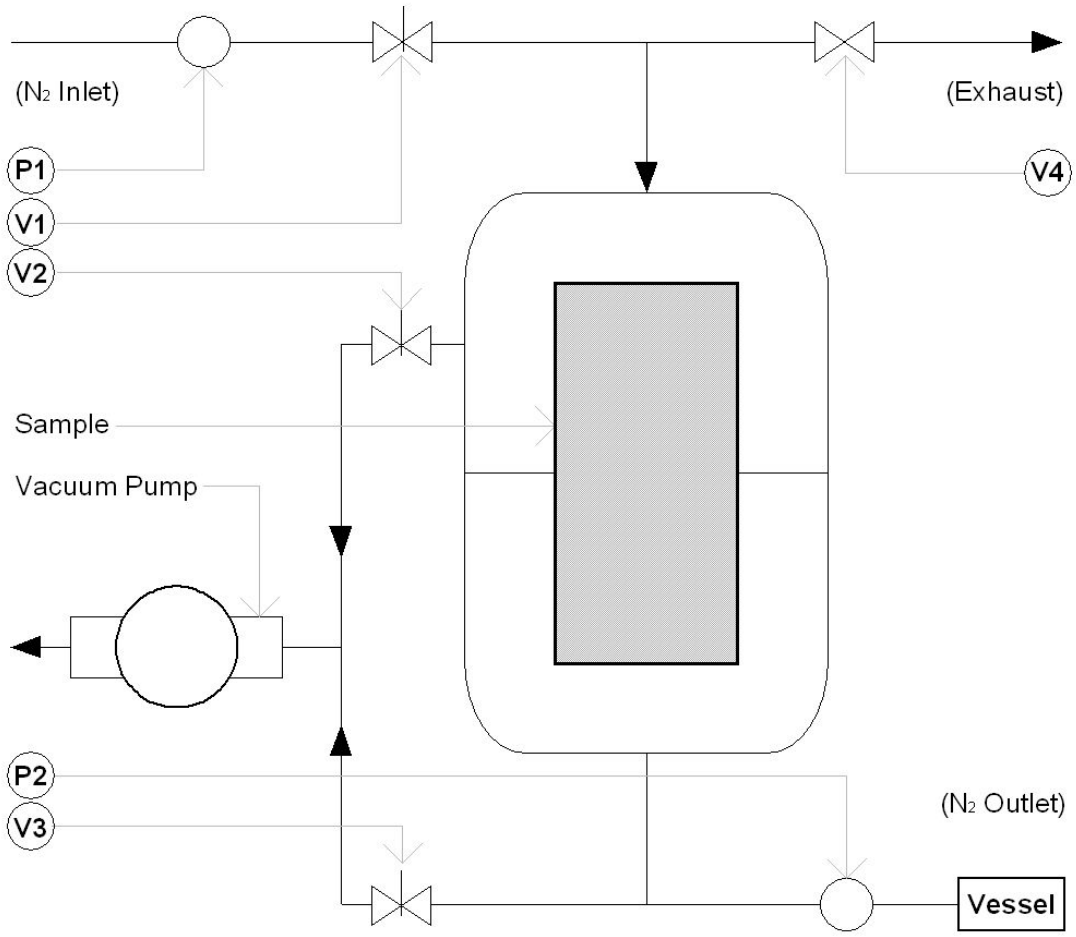


Figure 3-9: Schematic of the pressure-rise gas permeability measurement apparatus

With valves V2 and V3 open, the cell, vessel and sample were then evacuated to a pressure of 10 Pa using a vacuum pump (*Model E-Lab-2 Vacuum Pump*, BOC Edwards Ltd., Crawley, UK). The inlet side was isolated from the pump by closing valve V2 and the outlet side of the sample and the vessel were maintained at a low pressure (p_2) which was monitored using pressure gauge P2 (*Digital Manometer LEO 2* Keller (UK) Ltd., Dorchester, UK). Nitrogen at a constant pressure p_1 was fed into the system when V1 was opened. When V3 was closed, gas permeated through the sample and was collected in the vessel. The rate of pressure-rise $\frac{dp_2}{dt}$ at applied pressure p_1 was measured. The procedure was repeated at various inlet pressures. To run low mean pressure experiments, nitrogen fed into the inlet side was simultaneously evacuated through V4 and the balance between feed and bleed adjusted to give constant a (sub-atmospheric) pressure.

3.3.2 Diffusivity set-up and measurements

After completion of the permeability experiments the cell was used to measure the diffusivity of the same sample. A schematic of the cell set-up is shown in Figure 3-10 and a start-up and shut-down procedures can be found in *Appendix III*. A thorough evacuation of the sample and apparatus was carried about before the diffusion tests. The inlet pressures of nitrogen and oxygen were adjusted to give a pressure difference of zero. The apparatus and sample were filled with nitrogen, oxygen was then fed into the oxygen side of the sample and the gas pressures were adjusted accordingly. Oxygen diffusing through the sample to the nitrogen side was continuously monitored with an oxygen analyser (*800 Series Zirconia Cell Oxygen Analyser Model 810*, Systech Instruments Ltd., Thame, UK) which was also used to measure

the flowrate of the nitrogen purge stream. Over a period of time the oxygen concentration reached an equilibrium value.

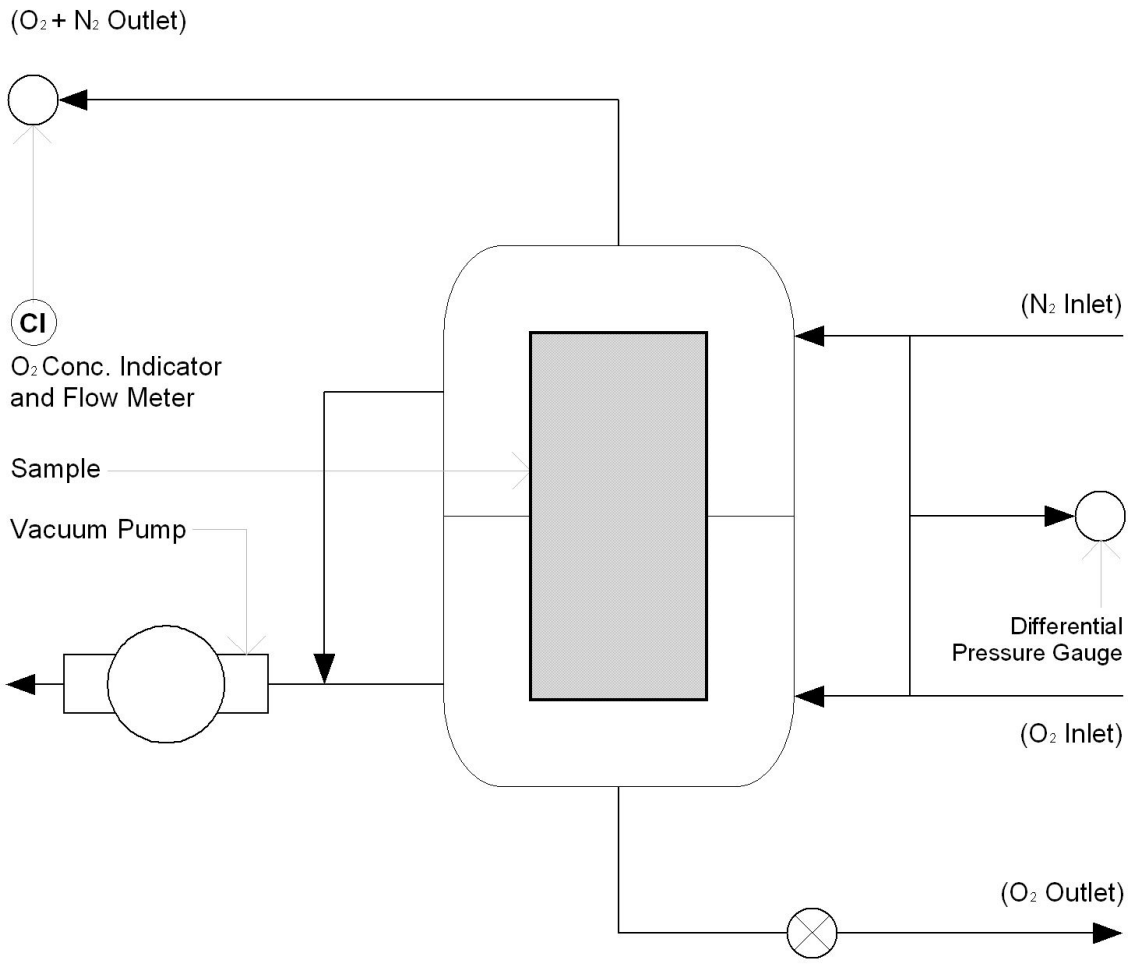


Figure 3-10: Schematic of the diffusivity measurement apparatus

3.3.3 Steady state diffusion of oxygen through nitrogen filled pores

The same porous solid samples from the permeability investigation were used in the diffusion investigation. The effective diffusion coefficient of oxygen through the sandstone

samples was determined from measurements of the oxygen concentration in the nitrogen outlet stream. In all cases, the oxygen concentration (initially zero) gradually increased until an equilibrium concentration was reached, the final concentration and time taken for equilibration was dependent on the structure of the porous network. Figure 3-11 shows an example of the results obtained from the steady state diffusion experiments. It shows the increase of the oxygen concentration in the nitrogen purge stream after diffusion through the pores of Sample R1.

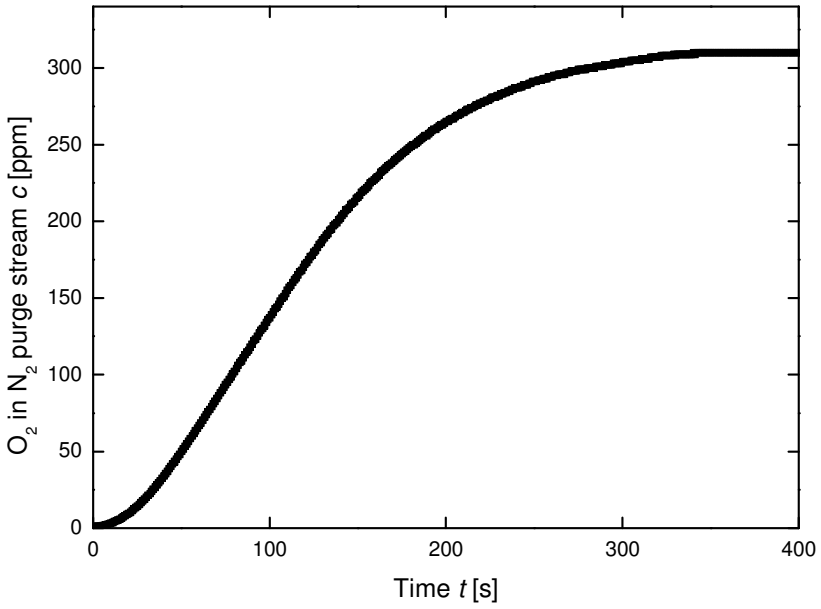


Figure 3-11: Rate of oxygen diffusion through pores of Sample R1

In this example, the final oxygen equilibrium concentration is 322 ppm and this value is used in Equation 2.22 to calculate the effective diffusion coefficient of oxygen in nitrogen through the porous solid which is $1.82\times10^{-8} \pm 8.7\times10^{-10}$ m^2 s^{-1}. (The free diffusion coefficient of oxygen in nitrogen is 1.81×10^{-5} m^2 s^{-1}).

3.3.4 Transient diffusion of oxygen through nitrogen filled pores.

Figure 3-12 shows the experimental transient diffusion data fitted to the theoretical data for Sample R1. The experimental data were fitted to the theoretical curve for data for F (Equation 2.25) using the procedure described in *Appendix IV* (see Figure 3.11). The corresponding value of $\left(\frac{D_{AB}t}{L_{eff}^{\ 2}}\right) = 0.138825$ interpolated from values in Table A.1 in *Appendix IV*. The effective pore length was calculated to be 132 mm and the tortuosity is ratio of the actual sample length to the effective pore length and therefore is 5.3. Equation 2.24 was used to calculate an effective porosity of 28.3%.

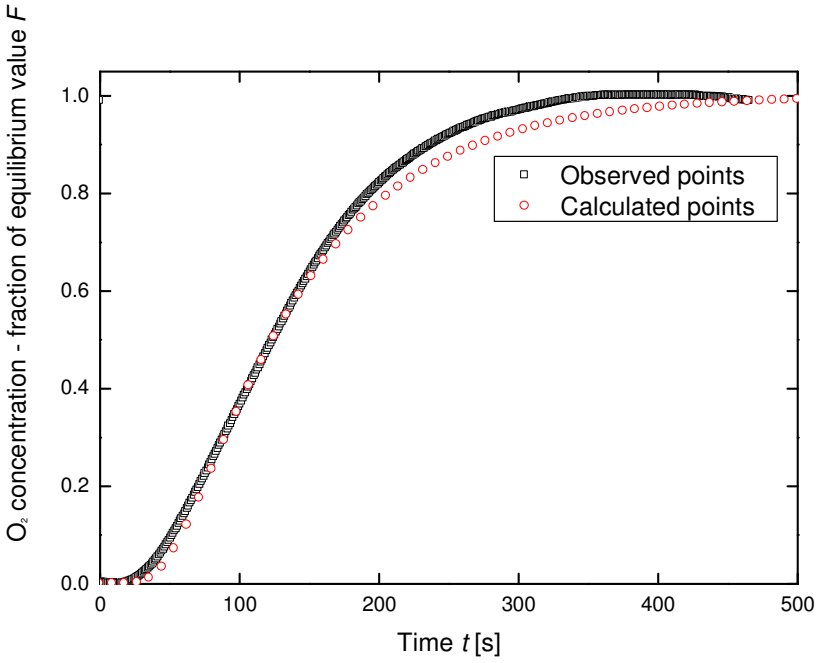


Figure 3-12: Plot of experimental transient diffusion data fitted to theoretical data at F = 0.5 for Sample R1

3.4 Overview

Following the construction and testing of a prototype gas permeability apparatus, a new integrated permeability-diffusion apparatus was constructed and successfully commissioned for permeability measurements and for both steady state and transient diffusion studies. It was demonstrated that the diffusion measurements gave reasonable values for tortuosity and effective porosity. This apparatus is essentially complementary to the integrated mercury permeability apparatus described in Chapter 4.

CHAPTER 4

DEVELOPMENT OF AN INTEGTRATED APPARATUS FOR MERCURY PENETRATION PERMEABILITY AND CONDUCTANCE

In Chapter 2, the (widely used) mercury porosimetry technique for measurement of pore size distribution was described and discussed. The much less widely used mercury permeability method was also described as was the mercury conductivity technique. Though each of these techniques can, in itself, give valuable information, there is a clear case for development of an apparatus in which all three methods can be used simultaneously. Such an integrated approach avoids having to cross reference data from one apparatus to that from another (for example the use of mercury porosimetry data from one apparatus in the interpretation of mercury permeability data from another). The production, commissioning and application of such an apparatus was a major objective of the work described in this thesis. The design, construction and commissioning of this apparatus is described in this present Chapter and the applications of the methods (together with the gaseous transport methods described in Chapter 3) to two types of porous media (namely sandstone rocks and polymer foams) are discussed in Chapters 5 and 6 respectively.

4.1 Introduction to the mercury integrated method

Triple distilled mercury was used and was obtained from Rose Chemicals Ltd., London, UK. Oxygen free nitrogen (99.998% purity) supplied by BOC Edwards Ltd., Crawley, UK was used to apply pressure to the mercury.

Using the apparatus described hereunder, the aim is to provide more information about the dynamic flow and diffusion performance of samples of porous media as a function of pore space occupied by extending the use of mercury penetration techniques. A technique has been developed to include three distinct procedures to determine the properties, as outlined below:

1. **A variation of mercury intrusion porosimetry** which is used to measure:

- Effective pore volume
- Effective porosity
- Pore diameter distribution
- Flow limiting pore diameter of porous solids.

2. **Mercury permeability** which is used to obtain the:

- Permeability distribution as a function of the pore volume
- Total permeability of a porous medium.

3. **Electrical conductivity measurements** of mercury contained in the pores of the porous medium to determine:

- Electrical conductivity ratio
- Tortuosity
- Effective pore length of a porous medium.

The methods are discussed in more detail in this section. A photograph of the equipment designed and built is shown in Figure 4-1.



Figure 4-1: Illustration of the mercury permeability and conductivity apparatus

4.1.1 The mercury porosimetry technique

The mercury intrusion characterisation technique initially is based on and follows the widely-used principle of mercury porosimetry, in which the medium is first evacuated and then brought into contact with mercury. The technique however differs as the sample is first sealed in an impermeable coating (see *Section 3.1*) to avoid any flow from the sides of the sample and mercury is applied to the sample on two faces. Pressurisation of the mercury leads to mercury penetration into the pores. The relationship between the diameter d of the smallest pore penetrated at a given applied pressure p is set out in Equation 4.1 (Smithwick, 1982):

$$d = \frac{-4\gamma \cos\theta}{p} \qquad 4.1$$

where γ is the surface tension of mercury and θ is the contact angle between mercury and the surface of the sample. The intrusion technique relies on the use of successive incremental increases in the applied pressure to control the diameter of pores that are penetrated by mercury. The largest pores will be penetrated first and then smaller and smaller pores are filled as the pressure is progressively increased.

At each applied pressure, corresponding to a given pore diameter penetrated, the volume of mercury that has entered the pores of the sample is measured. By measuring the additional volume of mercury that is pushed into the sample at each incremental pressure increase, the

volume of the pores within a diameter range calculated from Equation 4.1 for the initial and final pressures can be estimated and, hence, the pore size distribution determined.

The sample is deemed to have reached full saturation when an increase in applied pressure does not force any more mercury into the pores. The maximum amount of mercury taken up by the medium due to the application of pressure gives an indication of the total effective pore volume. The pore volume is called “effective” as it is the volume that is interconnected and available for fluid flow only i.e. closed pores cannot be filled. Since the volume of the sample is known, the effective porosity can easily be calculated as it is the fraction of the volume taken up by the effective pore volume.

Mercury is pushed into the sample from two opposite faces of the sample core. As the pressure applied to the mercury is increased, the mercury entering the sample from either side will eventually come into contact. This is a crucial point for the conductivity measurements as will be discussed later – but the liquid contact indicates that the mercury forms an continuous pathway throughout the sample and at least one pore is connected from end to end of the sample and fluid will be able to flow through it. Since the pores are penetrated starting from the largest first to the smallest (from low to high pressure) the pore diameter that limits the flow can be defined. The pressure required for the mercury to come eventually into contact will be characteristic of a pore of a specific diameter and is defined as the *flow limiting pore throat diameter.*

4.1.2 The mercury permeability measurement technique

At the point where the mercury is in contact through the material, it becomes possible to start making permeability measurements. The mercury on either side of the sample is at equal pressures and by creating a pressure differential across the sample, a measurement of the volumetric flowrate of mercury allows for determination of the permeability. A distribution is obtained when the permeability is measured at a range of applied pressures and hence pore diameters. The permeability rises with increasing pressure i.e. with decreasing size of penetrated pore. A plot of permeability against pressure (or pore volume penetrated) gives unique information about the mechanism of flow through the medium. Thus, the contribution of the various sizes of pore to the permeability can be directly determined. At a high enough pressure, the mercury permeability becomes equal to the permeability for a wetting fluid (gas or liquid) and is defined in this case as the total permeability of the porous solid.

4.1.3 Electrical conductivity measurements of mercury in the pores of a porous solid

When mercury is contained within the pores of an electrically non-conducting medium, the measured mercury electrical conductivity is governed by the electrical conductance through the mercury.

When an alternating current is applied across the porous solid while the mercury intrusion experiments are carried out, no electrical current will pass across the sample until the mercury comes into contact through the interconnected pores of the sample. Here it is assumed that the porous solid is an electrically insulating medium. When there is mercury

contact through the sample, the electrical resistance can be easily measured and the electrical conductivity deduced. By analogy with Equation 2.24 we may write:

$$r_{C\,p} = \frac{\sigma_p}{\sigma_O} = \frac{\varepsilon_{eff,p}}{\tau_p^2} \qquad 4.2$$

where r_{Cp} is the ratio of the electrical conductivity σ_p of the sample, after mercury has been forced into the sample at pressure *p,* to that of pure mercury σ_O. $\varepsilon_{eff,p}$ and τ_p are the effective porosity and tortuosity of the pores penetrated at pressure *p.* When all the pores of the sample are filled with mercury, then the medium is saturated and $\sigma_p = \sigma_O$ and $r_{Cp} = r_{C.}$ Equation 4.2 is a useful starting point for analysis of the diffusional performance of the medium. Thus, if it is assumed that $\varepsilon_{eff,p}$ corresponds to the pore volume occupied at pressure p (as indicated by the porosimetry measurements) then τ_p can be estimated as a function of pore size. In any case, the variation of r_{Cp} with pore size occupied gives an indication of the contribution of the various pores to the total diffusivity, just as the similar measurements of mercury permeability did in the case of total permeability.

The apparatus has been designed to encompass all three of the above mentioned techniques. It was possible to use all of the techniques on a single sample encased in a single measuring cell in the apparatus with no need for any adjustments or changes to the set-up. The design of the apparatus and the operating procedure are discussed below and a set of results are presented to demonstrate the analytical process carried out on experimental data.

4.2 Integrated mercury apparatus description and operation

4.2.1 Design description

The apparatus was designed so that the sample could be evacuated from two opposite sides using a vacuum pump before measurements were carried out and so that mercury could come into contact with the sample at opposite ends. Nitrogen gas was used to pressurise the mercury and force it into the pores of the porous sample. The apparatus is shown schematically in Figure 4-2 where the two parts of the system, the nitrogen and the mercury systems are highlighted. This *Section* outlines the methods used for operation of the apparatus and refers to valves and connections shown in Figure 4-2. A concise start-up and shut-down procedure is given in *Appendix V.* The labels in Figure 4-2 refer to the following:

1 Sample cell

2 Mercury sumps

3a & 3b Measuring manometer tubes

4 Connection to vacuum pump (*Model E-Lab-2 Vacuum Pump*, BOC Edwards Ltd., Crawley, UK)

5 Nitrogen inlet

6 Nitrogen exhaust

V Pirani vacuum gauge (Pirani APG-M-NW16 with Active Piiani Gauge ADL Active Digital Controller, Boc Edwards Ltd., Crawley, UK)

P1 – P3 Pressure gauges (*Digital Manometer LEO 2* Keller (UK) Ltd., Dorchester, UK)

V1 – V15 Manual valves (Ball, needle and three way valves, Swagelok, Herts, UK)

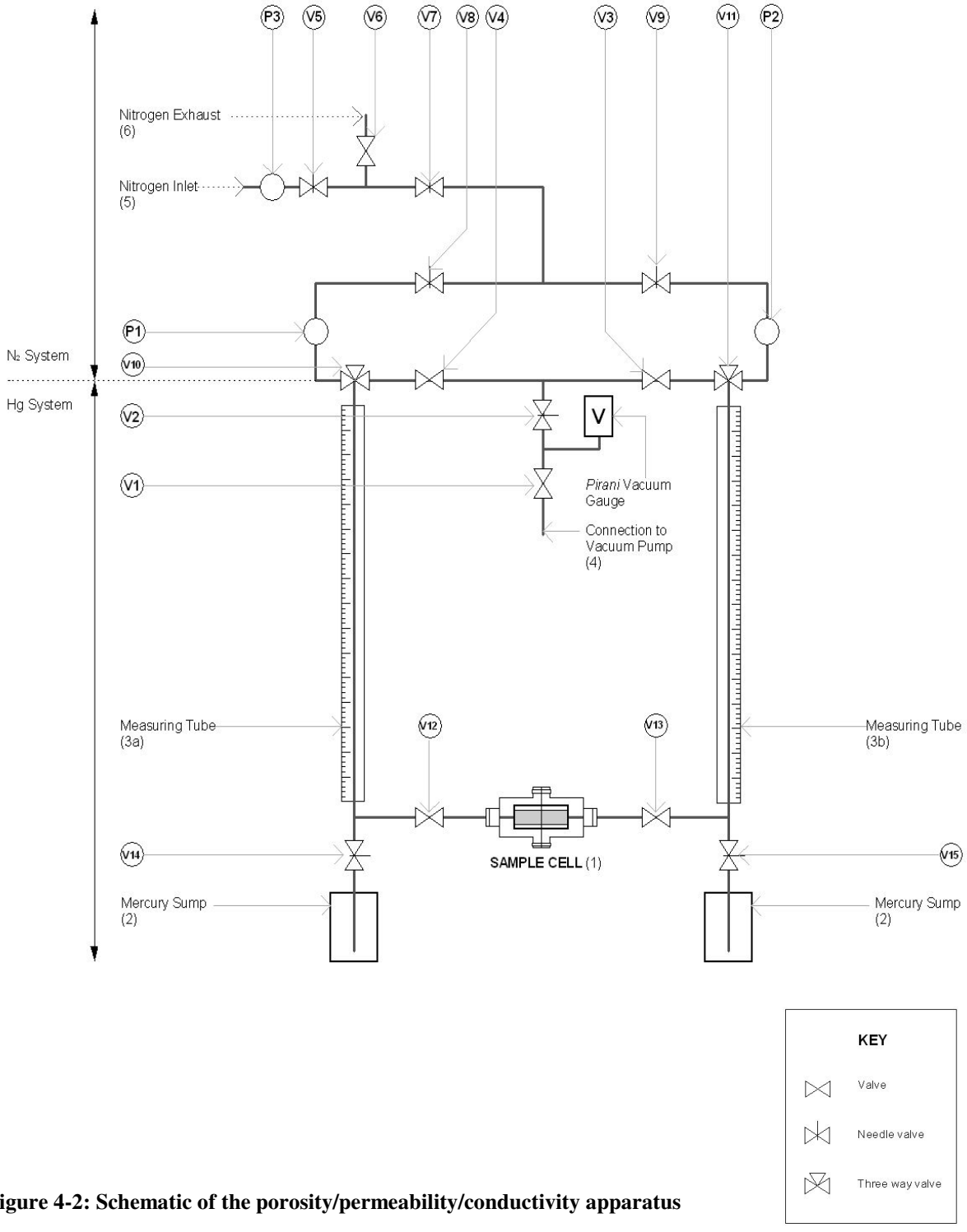


Figure 4-2: Schematic of the porosity/permeability/conductivity apparatus

The sample was sealed into the sample cell (as shown in Figure 4-3). The sample cell was fitted in the middle of the mercury system between two mercury sumps which were directly connected to measuring tubes *(3a)* and *(3b)*.The measuring tubes were also open to the ends of the sample cell. The mercury system and the sample could be evacuated through the vacuum pump attached to *(Point 4)*. During this evacuation process, the pressure of the mercury system could be monitored by means of a Pirani Vacuum Gauge *(V)*. For operation, the pressure on the respective sides of the nitrogen system could be measured by means of pressure gauges P1, P2. The nitrogen system consisted of a nitrogen inlet *(Point 5)* connected to a nitrogen cylinder (not shown) and a nitrogen exhaust *(Point 6)*.

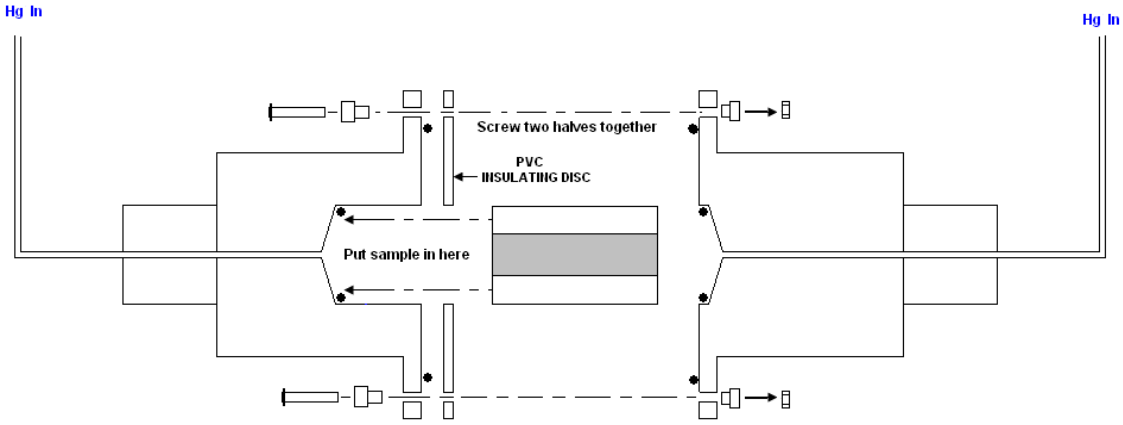


Figure 4-3: Detail of the sample cell

4.2.2 Preparation of samples

Before measurements could be carried out, the sample cores were prepared using the preparation technique outlined in Chapter 3 and were fitted into the sample cell as illustrated

in Figure 4-3. The sample cell was then connected to the apparatus and electrodes were fitted at either side of the sample.

4.2.3 Mercury intrusion porosimetry (MIP)

MIP involved the measurement of mercury volume uptake by the sample as a function of the pressure applied at the interface between the bulk mercury and the sample faces. The initial value of this pressure corresponds to the static head applied by the mercury which must be low enough to avoid penetration of mercury into the largest pores in the sample.

The system was evacuated and set up as described in *Section 4.2.* The heights of mercury in each of the measuring tubes (which should be identical) were recorded. To begin the penetration of mercury into the largest pores, nitrogen gas was applied to the system at a known pressure. The nitrogen pressure was controlled using the inlet valve V5, and when necessary could be lowered using the exhaust valve V6. Simultaneously turning the three-way valves V10 and V11 to open the nitrogen-side, let nitrogen gas in to the mercury system and applied pressure to the mercury in the measuring tubes. The gas forced mercury at the faces of the sample to penetrate the larger pores. The pores of equivalent size (or larger than the diameter that corresponds to the applied pressure, see Equation 4.1) were penetrated with mercury. Once the system had equilibrated, the new heights in the measuring tubes were recorded. The difference in the initial and final heights of mercury in the measuring tubes enabled the deduction of the volume of mercury that had penetrated the pores at the applied pressure and hence, the total volume of the pores open to pore throats of the given diameter.

Increasing the applied nitrogen pressure by small increments, repeating the process of pore penetration and taking measurements of the mercury volume that had filled the sample pores enables the determination of a pore size distribution. During the measurement of the pore size distribution, an increase in the pressure will eventually see the mercury from both sides of the cell coming into contact through the pores of the sample. The corresponding pore diameter is called the flow limiting pore diameter as this is the pore size that must be penetrated with mercury before fluid flow can occur. After each incremental pore volume measurement was made, permeability and conductivity measurements were carried out before the pressure was increased further. This procedure was repeated until no further mercury penetration could be achieved in our apparatus.

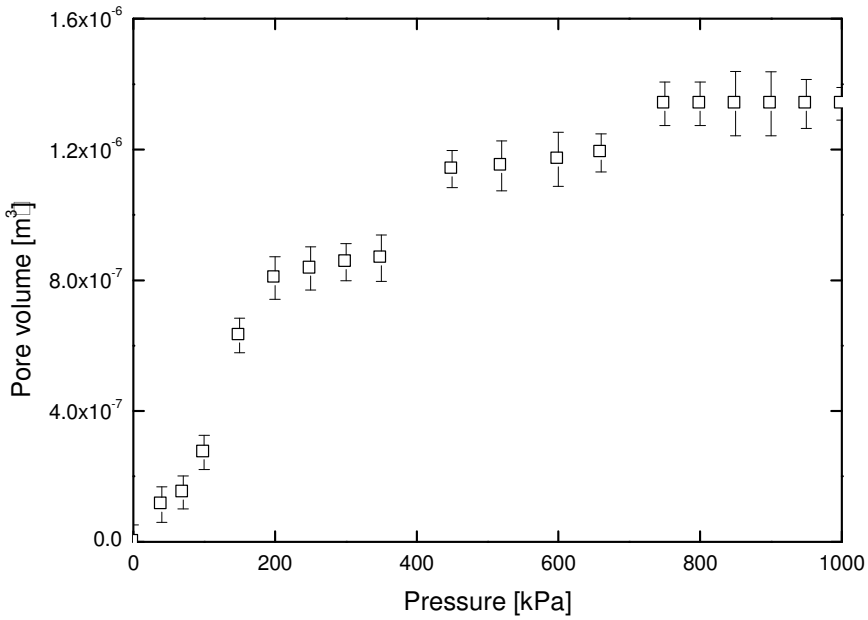


Figure 4-4: Pore volume distribution as a function of the applied pressure for sandstone Sample R1

Sandstone Sample R1 was tested in the equipment and an example of the results obtained using the mercury porosimetry technique is given in Figure 4-4. As the pressure applied to the mercury is increased, the volume of mercury pushed into the pores of the sample gradually increases. The resultant stepped curve may be attributed to experimental inconsistencies. It is possible that the experiment was carried out too rapidly at the applied pressure of 380 kPa and 680kPa and hence at these points an under-measurement of the total pore volume can be seen. The total volume of mercury in the sample at 800 kPa is $1.3\times10^{-6} \pm 5\times10^{-8}$ m^3, as the pressure is increased further; the volume of mercury in the sample remains the constant indicating that the total porous volume is filled. The volume of mercury in the sample at this point was used to calculate the total porosity of the sample as 40.4 ± 1.5 %. The values are summarised in Table 4-1.

Table 4-1: Summary of the results obtained using the mercury porosimetry technique for sample R1

Sample	Pore Volume [m^3]	Porosity [%]
R1	$1.3\times10^{-6} \pm 5\times10^{-8}$	40.4 ± 1.5

4.2.4 Mercury permeability distribution and total permeability

Figure 4-5 is a set of diagrams showing the four main steps required for permeability measurements. Image 1 shows the application of mercury to the faces of the sample and Image 2 shows the filling of the manometer tubes with mercury. Image 3 shows the small change in heights of the mercury in the manometer tubes due to the application of a small (compared to the total pressure) pressure differential across the sample. The mercury heights could be reduced in the measuring tubes 3a or 3b by opening then closing V14 or V15,

respectively to create a very small pressure differential. Image 4 shows the flow of the mercury in the direction of the differential.

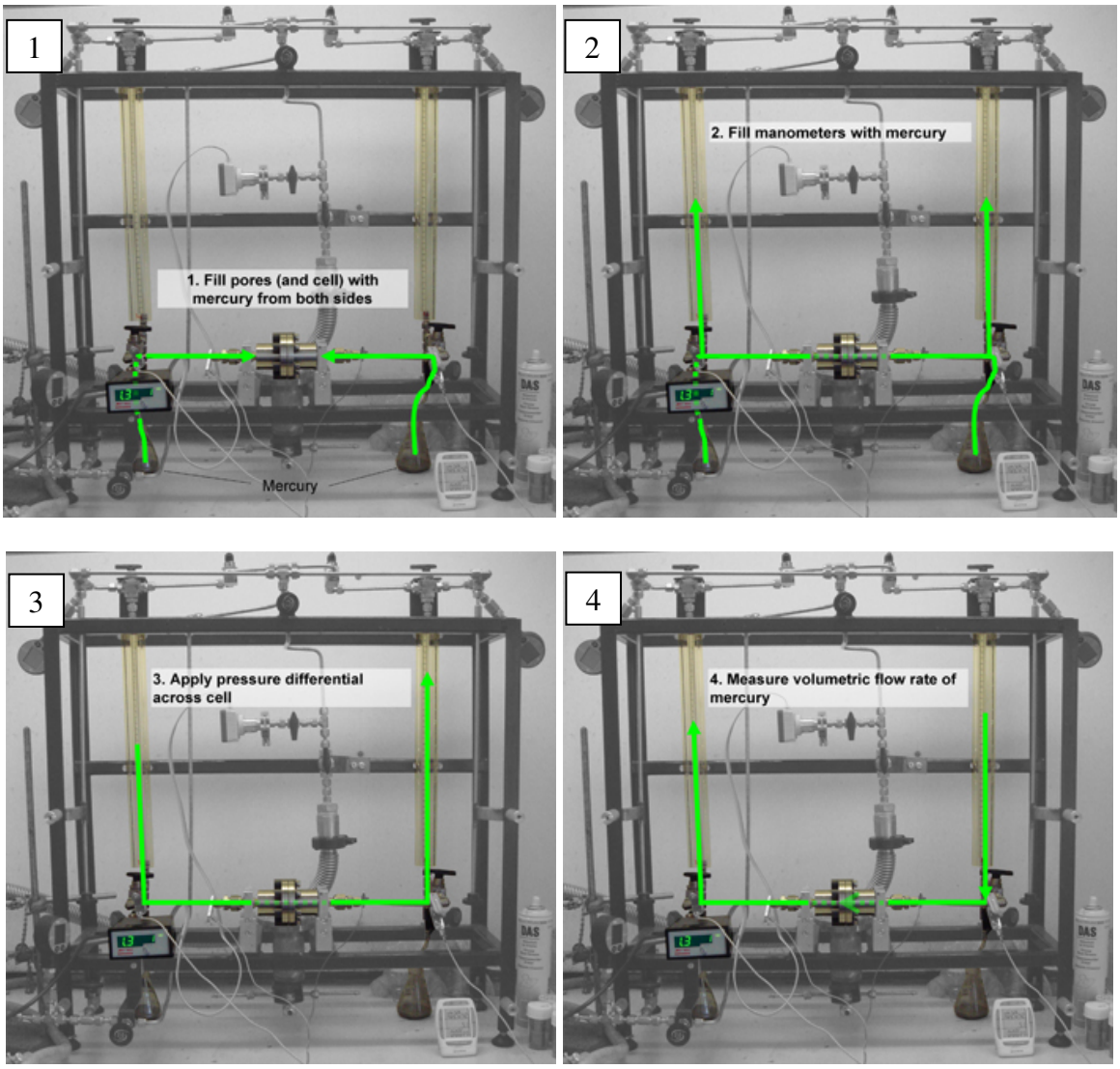


Figure 4-5: Schematic procedure used for mercury permeability measurements

Measuring the rate of change in heights of the mercury in the measuring tubes allows for the determination of the volumetric flowrate of mercury through the sample. To begin flow measurements, the heights of mercury in the measuring tubes at the initial condition, and

hence the difference in heights, Δh_0 at time t=0 were recorded. The pressure in the nitrogen system should remain unchanged from the porosimetry measurements, and should not be notably affected by the small adjustments for the formation of the differential. Opening V10 and V11 (see Figure 4-2) simultaneously to the nitrogen side subjected the mercury in the measuring tubes to the gas pressure (which was marginally lower in one tube than the other due to the differential). The mercury was forced through the sample in the direction of the pressure differential. To measure the flowrate of mercury through the sample, the time taken for mercury to reach the final heights in the measuring tubes at time, $t=t$ was measured. As the valves are opened to induce mercury flow through the material, there is an initial period where the height change is more rapid, the volumetric flowrate then stabilises and then gradually decreases as the heights begin to equilibriate. It must be taken into account when carrying out the flow measurements that the true volumetric flowrate can only be measured after the initial relatively rapid period and before the gradual decrease into height equilibriating rate. An effective way of identifying this true flowrate would be to plot the rate of change of flowrate to identify the three different time scales to ensure that it is the intermediate volumetric flowrate that is used for the calculation of the permeability. The new mercury heights in tubes *3a* and *3b* and hence Δh_t were recorded. A detailed operating procedure is presented in *Appendix V*

Equation 4.3 can be used to calculate the mercury permeability when the difference in heights of mercury in the measuring tubes at $t=0$ and $t=t$ are measured. The rate at which mercury flows through the sample is characteristic of the permeability of the pore space filled

with mercury and is dependent on the applied pressure. A derivation of Equation 4.3 is given in *Section 2.3.2*:

$$k = \frac{\log \Delta h_0 / \Delta h_t}{t} \frac{A_1}{2A_2} \frac{\mu L}{\rho g} \qquad 4.3$$

where k is the permeability of the porous sample, Δh is the change in height, t is the time taken for the height change, A_1 is the area of manometer tubes, A_2 is the cross-sectional area of sample, μ is the viscosity of mercury, ρ is the density of mercury, L is the length of sample and g is acceleration due to gravity (Hewitt, 1960).

The volume of mercury pushed into the sample was increased as the porosimetry technique continued and both pore size and permeability were measured at higher nitrogen pressures. Repetition of this technique over a range of nitrogen pressures can lead to the determination of permeability distribution of a porous medium as a function of pore space filled by liquid. An example of a permeability distribution obtained using the mercury permeability technique is given in Figure 4-6.

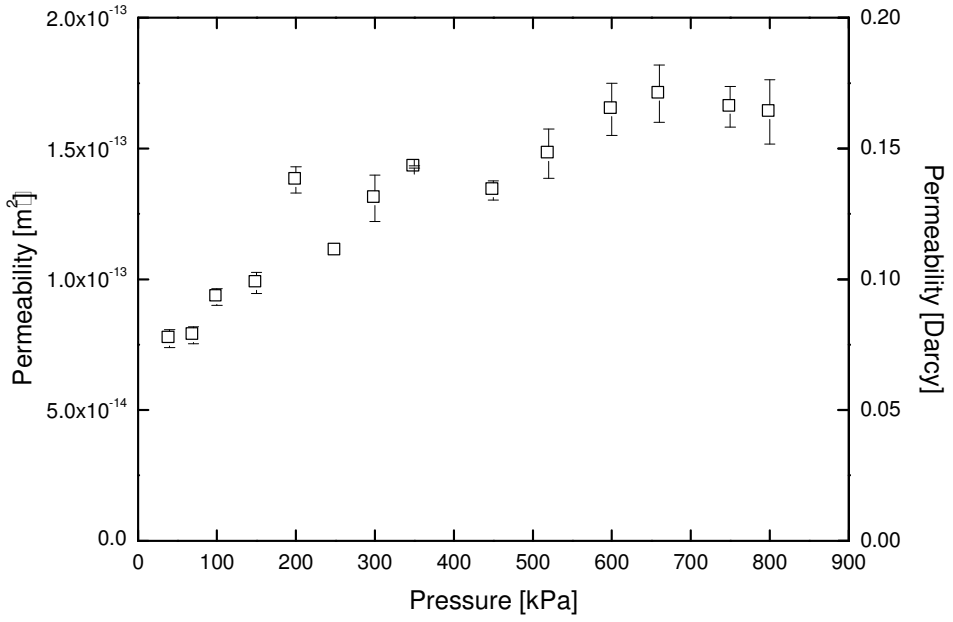


Figure 4-6: Permeability distribution for sandstone Sample R1

The permeability as a function of the absolute (or total) permeability is commonly described as the relative permeability and when plotted against the saturation of the porous solid, a relative permeability curve is produced. In the mercury intrusion experiments carried out in this work, the primary drainage relative permeability of the non-wetting phase (mercury) has been measured and the relative permeability curve is shown in Figure 4-7..

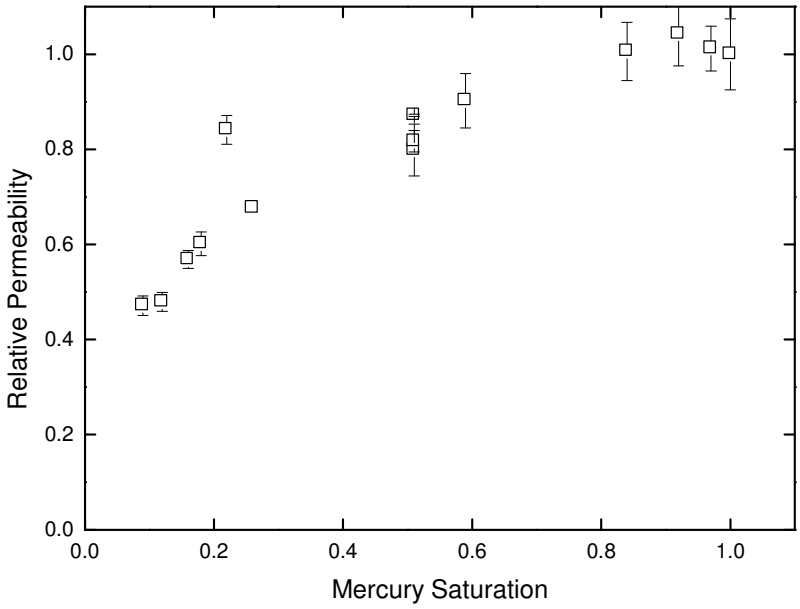


Figure 4-7: Relative permeability curve for sandstone R1

It is evident that that there is a significant pressure limitation in mercury permeability method and the relatively small permeability range (seen in Figure 4-6 and Figure 4-7) may be attributed to high pressure constraints in the apparatus and the possible inability to measure the total maximum permeability. This should be noted when quoting measurements of the total permeability and suggests that the mercury permeability method may in some cases provide an underestimation of the permeability.

Measurements were made of the flow of mercury through sandstone Sample R1. It is clear that as the pressure applied to the mercury increases, the permeability of the sample increases. The pressure at which the flow of mercury is initiated is at approximately 40 kPa,

this corresponds to a pore diameter of 40 ±13 μm, this is defined at the flow limiting pore throat diameter. The permeability at an applied pressure of 650 kPa is approximately 166 mD and as the applied pressure is increased, there is no further permeability increase. The total permeability of the sample is therefore 166 mD. These results are summarised in Table 4-2.

4.2.5 Electrical conductivity of mercury in the pores of a porous solid

Following on from the flow measurements, at the given applied pressure *p*, the electrical conductivity of the medium σ_p was determined by measuring (using a *195A Digital Multimeter*, Keithley Instruments, Inc., Ohio, USA) the voltage drop *E* across the sample resulting from the flow of an AC current *I* (drawn from a *Thurlby PL320 Dual power supply*, Electroplan, Herts, UK). σ_p is calculated from:

$$\sigma_p = \frac{I}{E}\frac{L}{A} \qquad 4.4$$

where *L* is the sample length in the direction of the current flow and *A* in the sample cross-sectional area in a direction normal to the current flow. The ratio $r_{Cp} = \sigma_p / \sigma_o$ (see Equation 4.4) can then be estimated and is shown as a function of pressure. Figure 4-8 shows the relationship between the electrical conductance and the saturation of the material on double logarithmic axes. Using Archie's law (Eqn 2.46) the parameter *n* can be deduced from the gradient as 2.3, this is consistent with values for Berea sandstone presented in the literature (Koplik *et al.,* 1984).

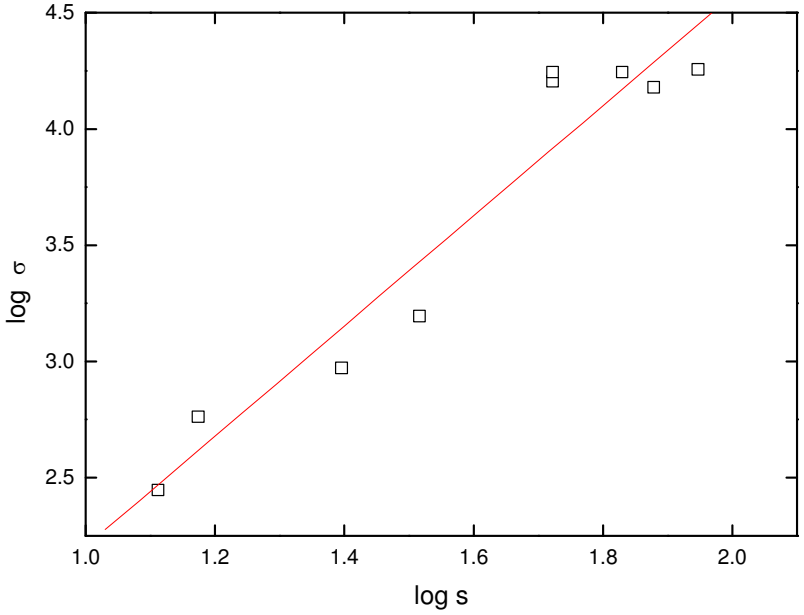


Figure 4-8: Conductance as a function of saturation for Sample R1

If it is assumed that $\varepsilon_{eff,p}$ corresponds to the pore volume occupied by the mercury at pressure p (as determined by the mercury porosimetry measurement) then the tortuosity ($\tau_p = L_{eff} / L$) can be estimated from Equation 4.2 and is shown as a function of percentage of pore volume occupied in Figure 4-9. The results for sandstone sample R1 are summarised in Table 4.2.

Table 4-2: Summary of the results obtained using mercury permeability and conductivity techniques on Sample R1

Sample	k [mD]	Limiting Pore Throat Diameter [µm]	r_c
R1	166 ± 13	40 ± 13	8.9×10^{-5}

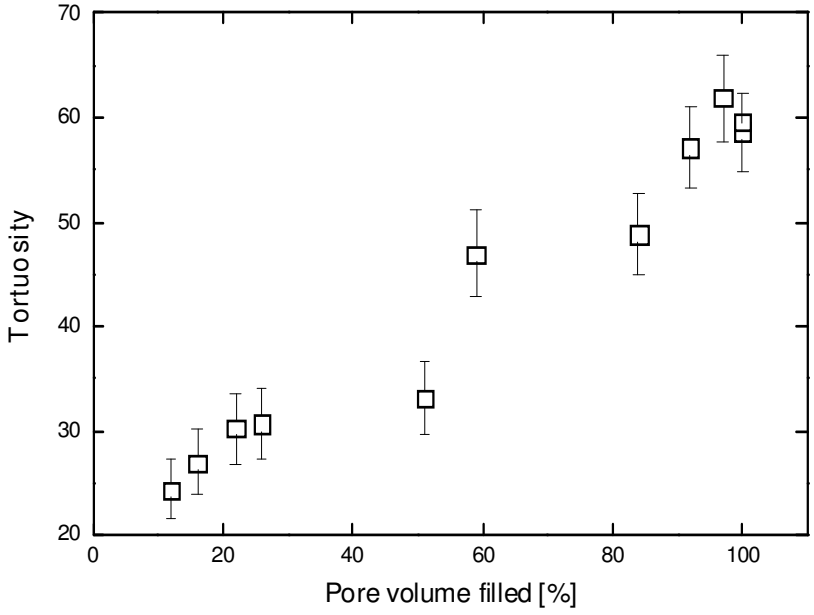


Figure 4-9: Tortuosity τ_p as a function of pore volume occupied for sandstone Sample R1

4.3 Overview

A new integrated apparatus for combined porosimetry, permeability and conductivity measurements using mercury penetration has been successfully designed, constructed and commissioned. When combined with the gaseous transport system described in Chapter 3, this integrated apparatus is capable of giving important new insights into the flow and diffusion behaviour of porous media. The application of these methods to the study of sandstones and porous polymer foams are described in Chapters 5 and 6.

CHAPTER 5

APPLICATION OF INTEGRATED METHODS TO THE STUDY OF POROUS MATERIALS

I: POROUS SANDSTONES

Porous sandstones are the archetypical materials found in oil and gas reservoirs and, as such, have been widely studied. However, by using the power of the integrated gas permeability/diffusion and mercury penetration methods described in Chapters 3 and 4, new light can be thrown on the structure and behaviour of such materials.

The purpose of Chapter 5 is to present and compare the measurements obtained for sandstone samples using the integrated gas permeability and diffusivity and the integrated mercury porosimetry, permeability and electrical conductivity apparatus described in Chapters 3 and 4 and to summarise the findings obtained throughout this investigation. In what follows, *Section 5.1* gives information on the sandstone samples used and *Section 5.2* and *5.3* present results for gas permeability and diffusion. *Section 5.4* presents results obtained using the mercury penetration methods and *Section 5.5* presents image analysis. *Section 5.6* discusses the results obtained from the respective integrated methods and from image analysis. Finally, *Section 5.7* summarises the findings.

5.1 Materials

5.1.1 Berea sandstone sample details

In this Chapter, studies of Berea sandstone samples which were used during the commissioning and set-up of the integrated characterisation methods are presented.

The Berea sandstone samples used in this work were supplied by Berea Sandstone Petroleum Cores, Ohio, USA. Berea Sandstone is a sedimentary rock with grains that are composed of quartz sand held together by silica. The relatively high porosity and permeability of Berea Sandstone makes it a good reservoir rock replica. The samples were cut into 13 mm diameter cylindrical cores and were dried for 24 h in a vacuum oven at 70°C as recommended by Caruso *et al.* (1985) to remove any excess moisture from the pores before they were used for experiments.

The porosities of the sandstone cores were determined from measurements of the absolute and bulk densities. The absolute densities were measured using a helium pycnometry technique. The bulk densities were measured indirectly by mass and volume measurements. The porosities were then calculated using Equation 5.1:

$$\varepsilon = 1 - \frac{\rho_{bulk}}{\rho_{abs}} \qquad 5.1$$

where ε is the porosity, ρ_{bulk} is the bulk density and ρ_{abs} is the absolute density. The sample codes, densities and porosities of the various sandstone samples used are shown in Table 5-1.

Table 5-1: Sample codes, density and porosity values of the sandstone samples used in this study

Sample Code	Density [kg m^{-3}]	Porosity [%]
R4	2702.0 ± 11.3	10.1 ± 3.4
R5	2702.0 ± 11.3	9.1 ± 1.6
S1	2706.9 ± 19.1	32.6 ± 7.5
S2	2789.0 ± 14.6	30.3 ± 0.7
S3	2840.8 ± 7.6	21.9 ± 1.1
S4	2789.0 ± 2.9	22.1 ± 1.2
S5	2674.5 ± 15.8	7.0 ± 0.4
S6	2646.6 ± 7.8	5.3 ± 1.1
S7	2651.3 ± 12.0	3.8 ± 0.3
S8	2654.8 ± 6.1	3.7 ± 0.7
S9	2942.7 ± 1.7	28.9 ± 5.7
S10	2942.7 ± 1.7	30.3 ± 7.2

The Berea sandstone sample cores were prepared according to the procedure outlined in *Section 3.1* before being used in the gaseous transport and mercury penetration apparatus described in Chapters 3 and 4.

5.2 Permeability of sandstone - results

5.2.1 Sandstone permeability - data reproducibility

The integrated apparatus for measurements of gas permeability and diffusivity discussed in *Section 3.3* was commissioned using sandstone samples R4 and R5 and the initial results of gas permeability were used to ensure experimental reproducibility. Sandstone samples R4 and R5 were cut from the same original core. The two cores were tested three times and values of the permeability coefficient K at various mean pressures are plotted in Figure 5-1. The results are summarised in Table 5-2. The average viscous permeability coefficient k for the test sample is 18.8 ± 1.1 mD (± 6%). The average slip coefficient K_0 is 0.23×10^{-6} ± 0.02×10^{-6} m (± 8%). The values of k and K_0 were calculated from the gradients and intercepts of the curves as described in *Section 3.2.1.* It is evident that the results obtained are generally consistent implying a high level of confidence that the gas permeability cell produces reliable, reproducible data, though with some experimental scatter as would be expected.

Table 5-2: Standard deviations of the results obtained from reproducibility experiments

Sample	k [mD]	$K_0 \times 10^6$ [m]
R4	19.9	0.22
R5 x1	17.2	0.25
R5 x2	18.7	0.22
Average	18.8	0.23
SD	1.1	0.02

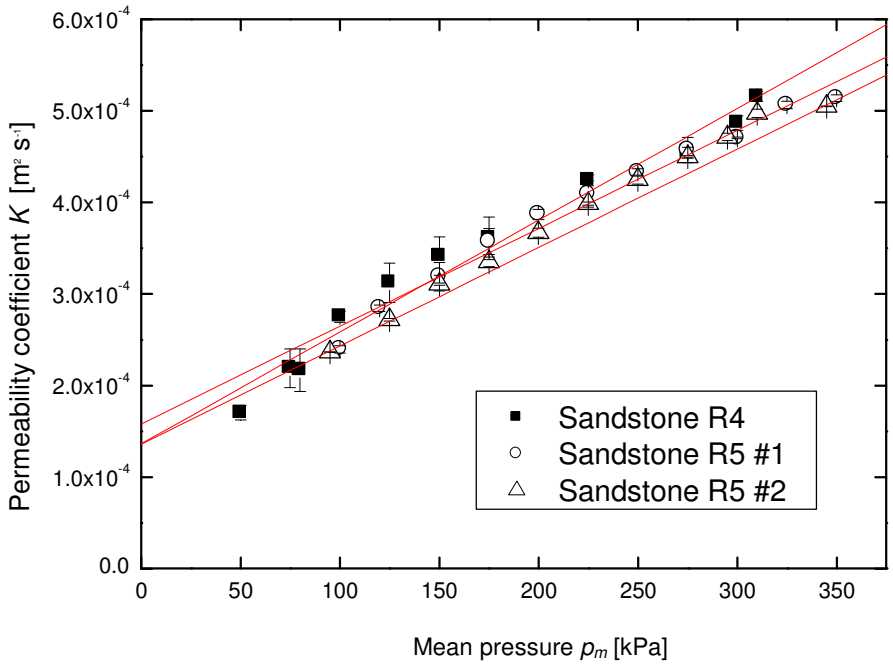


Figure 5-1: Permeability coefficient *K* at various mean pressures for sandstone Samples R4 and R5 used to demonstrate the reproducibility of data collected using the integrated gas permeability cell

5.2.2 Viscous permeability (k) and slip flow coefficients (K_0) of sandstone samples

Eight porous sandstone samples S1 – S8 with various porosities and pore structures were used in this investigation to illustrate the versatility of the gas pressure-rise technique. (Details of the samples used are given in Table 5-1). The sandstone samples were separated into two groups, Set 1 includes sandstones S1 – S4 which have porosities ranging from 32 – 22% and Set 2 includes sandstones S5 – S8 which have porosities ranging from 7 – 4%.

Each sample was placed in the gas permeability cell and the rate of pressure rise through the samples was measured at various applied inlet pressures. Figure 5-2 shows the linear relationships between the permeability coefficients K and the mean pressure p_m for high porosity sandstone samples in Set 1.

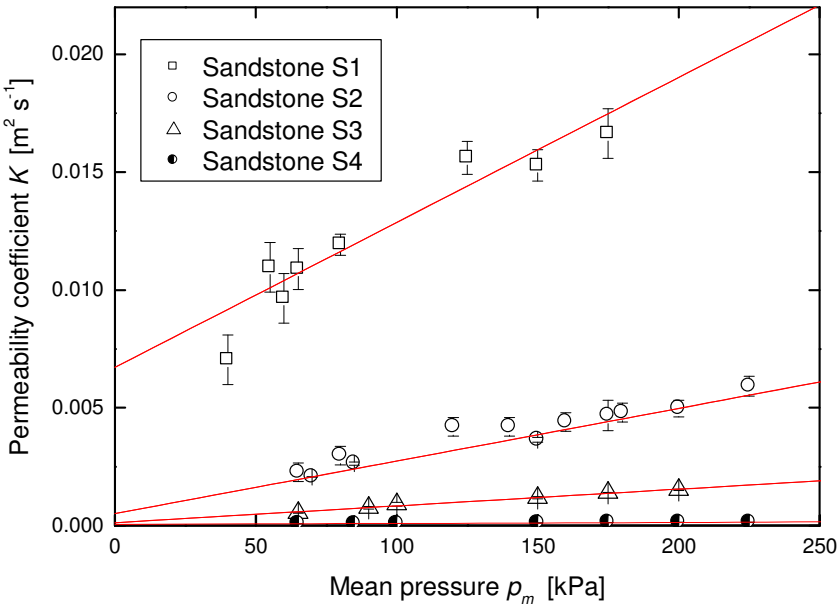


Figure 5-2: Permeability coefficient at various mean pressures for sandstone Samples S1 – S4

The viscous permeability was subsequently determined from the gradient of the linear fits. Sample S1 had the highest permeability of 1050 ± 166 mD ($1.05 \pm 0.166 \times 10^{-12}$ m^2). Figure 5-3 shows the data obtained from measurements of Set 2.

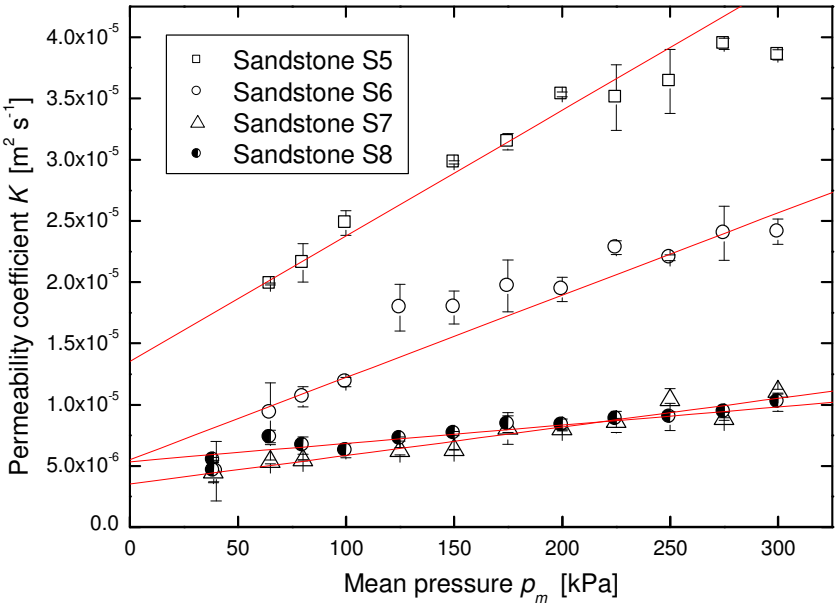


Figure 5-3: Permeability coefficient at various mean pressures for sandstone Samples S5 – S8

The viscous permeabilities are summarised in Table 5-3. Sandstone samples in Sets 1 and 2 demonstrate a general trend where the permeability of the samples is dependent on the porosity, with the lowest porosity Sample S8 having the lowest permeability. The slip flow coefficients K_0 were calculated from the intercepts of the linear fits and are also summarised in Table 5-3. For Sample S1 the Knudsen flow coefficient was $1.08\times10^{-5} \pm 1.68 \times10^{-6}$ m and was found to decrease for lower porosity samples. The slip flow coefficient would be expected to exert a more significant influence on gaseous transport the lower the pore size and, hence, the lower the viscous permeability. The results presented here are consistent with this.

Table 5-3: Porosity and permeability results

Sample	ρ_{abs} [kg m^{-3}]	ρ_{bulk} [kg m^{-3}]	Porosity [%]	k [mD]	k_{turb} [mD]	K_0 [m]
S1	2707 ± 19	1825 ± 97	32.6 ± 7.5	1050 ± 166	3300 ± 182	$1.08\times10^{-5} \pm 1.68\times10^{-6}$
S2	2789 ± 15	1902 ± 14	30.3 ± 0.7	350 ± 20.7	602 ± 4.98	$1.45\times10^{-6} \pm 3.41\times10^{-7}$
S2	2841 ± 7.6	2213 ± 25	21.9 ± 1.1	126 ± 2.98	160 ± 4.53	$1.10\times10^{-7} \pm 4.61\times10^{-8}$
S4	2789 ± 2.9	2172± 17	22.1± 1.1	9.81 ± 0.26	18.2 ± 0.32	$5.14\times10^{-8} \pm 3.11\times10^{-9}$
S5	2675 ± 16	2488 ± 13	7.0 ± 0.4	1.38 ± 0.11	5.35 ± 0.28	$2.54\times10^{-8} \pm 1.99\times10^{-9}$
S6	2647 ± 8	2507 ± 19	5.3 ± 1.1	1.11 ± 0.04	2.10 ± 0.02	$8.71\times10^{-9} \pm 8.58\times10^{-10}$
S7	2651 ± 12	2552 ± 50	3.8 ± 3.3	0.37 ± 0.01	1.17 ± 0.11	$5.16\times10^{-9} \pm 1.07\times10^{-10}$
S8	2658 ± 6.1	2560 ± 13	3.7 ± 0.7	0.24 ± 0.01	1.34 ± 0.02	$8.46\times10^{-9} \pm 2.36\times10^{-10}$

5.2.3 Investigation of permeability at low mean pressures

The feed and bleed technique discussed in *Section 3.3.1* was used to achieve low mean pressure differences across the cell. The low pressure gas permeability results are shown in Figure 5-4. Note the increase in the permeability coefficient at mean pressures lower than 50 kPa. As the mean pressure falls, gas flow is increasingly dominated by a diffusional process and viscosity has a smaller and smaller effect. Ultimately, at very low pressures, this diffusional process is dominated by collisions of molecules with the pore walls (Knudsen diffusion). The average viscous permeability of S9 and S10 is $1.7\times10^{-2} \pm 6.8\times10^{-4}$ mD and the extrapolated slip flow coefficient is $1.1\times10^{-6} \pm 1.6\times10^{-8}$ m. Extrapolation of the low pressure curve to zero pressure indicates a limiting Knudsen diffusion coefficient of approximately 0.027 m^2 s^{-1}.

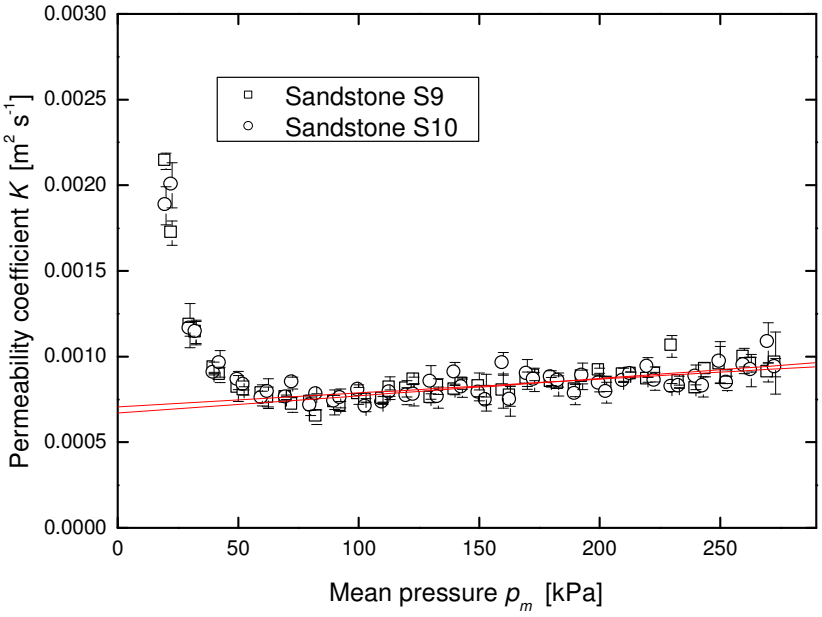


Figure 5-4: Results of gas permeability tests on sandstone Samples S9 and S10 from the investigation of low mean pressure

5.2.4 Results for turbulent flows

At higher flowrates, the flow through the porous medium may depart from purely viscous (Darcy) flow due to the occurrence of inertial (turbulent) losses. It is convenient to describe the flow in terms of the following equation (see Chapter 2):

$$\frac{dp}{dz} = au + b\rho u^2 \qquad 5.2$$

where the coefficient $a\left(=\frac{\mu}{k}\right)$ represents the viscous flow and the coefficient b is a measure of the inertial effects. From Equation 5.2, a methodology can be developed for representing such flows in which a plot of $C=\frac{\left(p_1{}^2-p_2{}^2\right)M}{2RTLG}$ (see Equation 2.32) against the mass flux G (proportional to $V\left(\frac{dp_2}{dt}\right)$) is a straight line with intercept $a\left(=\frac{\mu}{k}\right)$. The data obtained from the permeability investigations was used to assess the occurrence of turbulence in the pores.

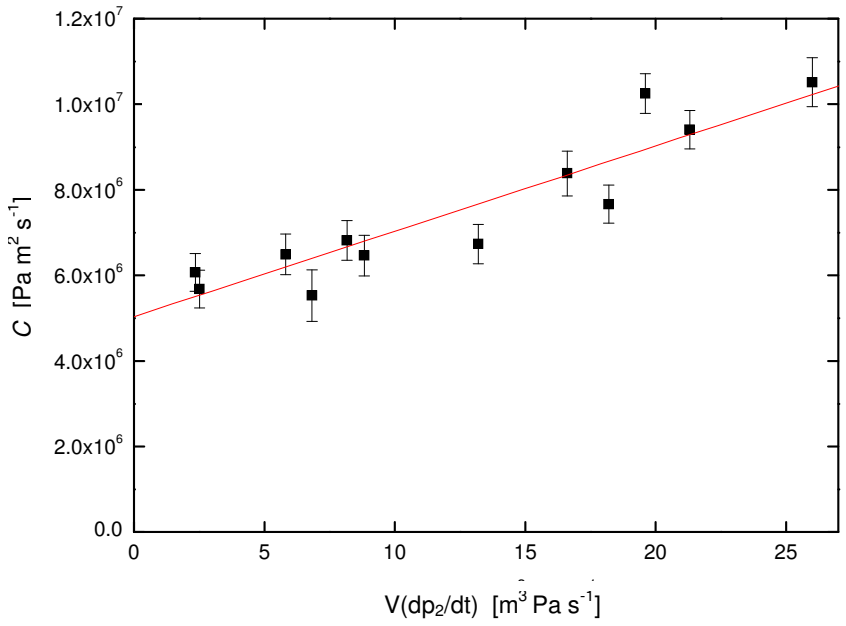


Figure 5-5: Linear plot of *C* vs. $V\left(\frac{dp_2}{dt}\right)$ for sandstone Sample S1

C was plotted against the term $V\left(\frac{dp_2}{dt}\right)$ as exemplified by Figure 5-5 which shows the variation of C vs. $V\left(\frac{dp_2}{dt}\right)$ for sandstone sample S1. The linearity indicates that turbulence occurs in the pores of the sample during the gas flow tests.

The graphs plotted of C vs. $V\left(\frac{dp_2}{dt}\right)$ for sandstone samples S2 – S8 are shown in *Appendix VI* and, as expected, the presence of turbulence is evident from the linear relationships. The intercept is equivalent to $\frac{\mu}{k}$, therefore the permeability k can be estimated; the results are given in Table 5-3. The estimation of permeability from the turbulent data gives values up to three times higher than the predictions from viscous flow and in all cases overestimates the permeability values. This finding should be investigated further. A possible reason for the discrepancy is that turbulent (inertial) effects are occurring at different stages in different pores. Suppose that there are two groups of pores and that we can write the following relationships for these two groups:

$$\frac{dp}{dz} = a_1 u_1 + b_1 \rho u_1^2 \qquad 5.3$$

$$\frac{dp}{dz} = a_2 u_2 + b_2 \rho u_2^2 \qquad 5.4$$

If we combine the two equations and rearrange and integrate we obtain the result that:

$$C = (a_1 + a_2)\frac{G_1 G_2}{G^2} + (b_1 G_1 + b_2 G_2)\frac{G_1 G_2}{G^2} \qquad 5.5$$

where G_1 and G_2 are the mass fluxes through the two groups of pores and G is the total mass flux. Thus a plot of C versus G will only extrapolate to $(a_1 + a_2)$ in the special case where $G = G_1 = G_2$.

5.3 Diffusivity of sandstone – results

5.3.1 Diffusivity of oxygen through nitrogen filled sandstone samples - data reproducibility

Two sandstone samples were used to investigate the reproducibility of results obtained using the gas diffusivity technique. Sandstone samples R4 and R5 were each tested. The concentration of oxygen in the nitrogen purge stream was measured on three separate occasions. After a given amount of time, an equilibrium concentration of oxygen was reached, this is shown in Figure 5-6 (for sandstone sample R4) and in Figure 5-7 (for sandstone sample R5).

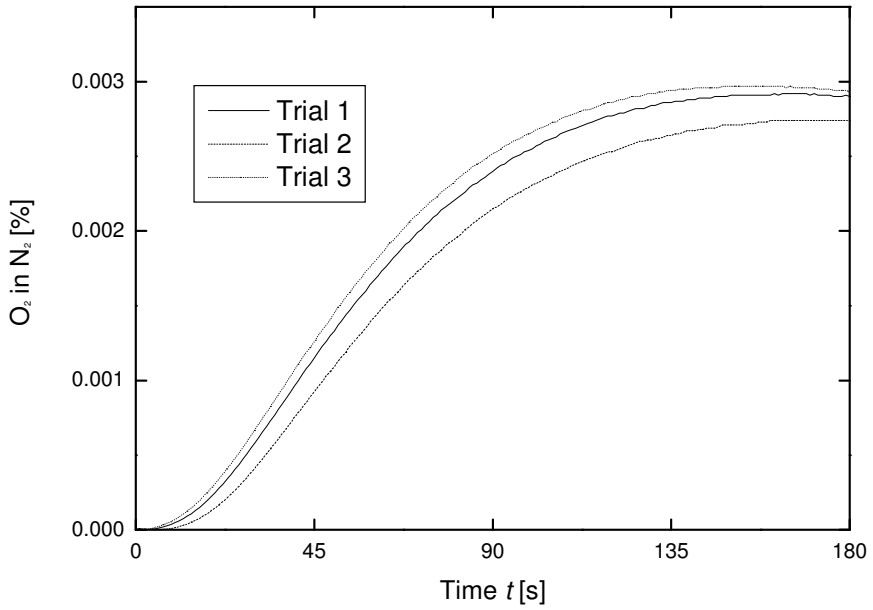


Figure 5-6: Oxygen concentration in the nitrogen purge stream as function of time for sandstone R4

Steady state and transient analysis detailed in *Section 3.3.3* were carried out on the results for each sample. For each of the trials, the equilibrium concentration of oxygen measured in the nitrogen purge stream was used to calculate the effective diffusion coefficient as described in Equation 2.22. The equilibrium concentrations reached are relatively consistent in each trial with a negligible error for both Sample R4 and Sample R5, the average values for the effective diffusion coefficients are 1.62×10^{-8} m^2 s^{-1} and 3.8×10^{-8} m^2 s^{-1}, respectively.

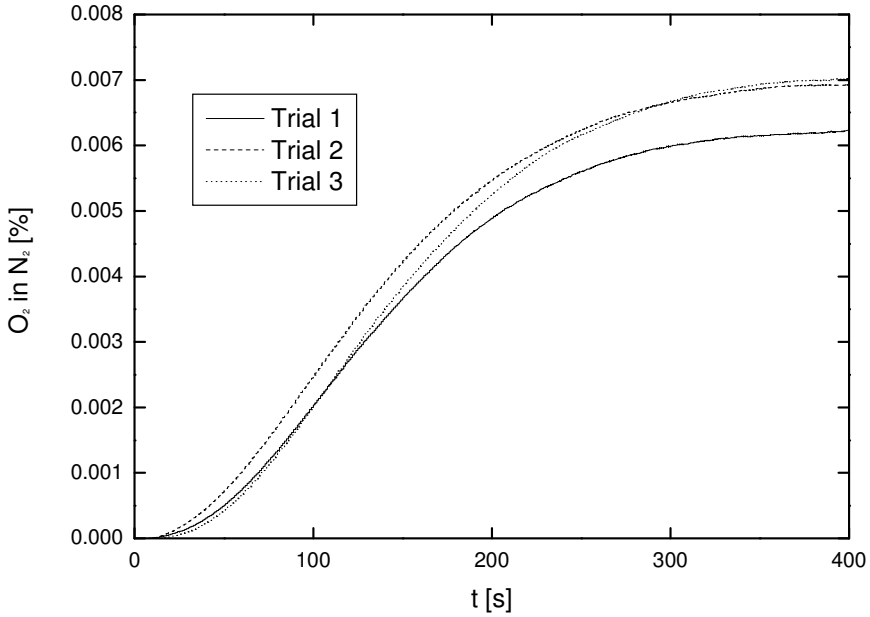


Figure 5-7: Oxygen concentration in the nitrogen purge stream as function of time for Sample R5

The reproducibility investigation confirms the reliability of the results obtained using the gas diffusion technique. The ratio r_D of the effective diffusivity (D_{eff}) to the (free space) diffusivity of oxygen in nitrogen (D_{AB}) may be equated (Equation 2.24) to the ratio $\left(\frac{\varepsilon_{eff}}{\tau^2}\right)$ where ε_{eff} is the effective porosity and τ is the tortuosity (and = $\tau = \frac{L_{eff}}{L}$ where L_{eff} is the effective pore length in a sample of length L). By fitting Equation 2.25 to the transient diffusion data, L_{eff} (and hence τ^2) can be estimated and, thus, ε_{eff} can be calculated from the known value of r_D. The values of L_{eff}, τ^2 and ε_{eff} were estimated in this way for each of the sandstone samples and the results from the trial tests on samples R4 and R5 are presented in

Table 5-4 in the form of average values and standard deviations. The standard deviation for the effective length calculations is approximately 5%; for tortuosity, 2.5%; and for the porosity is in the range 1 to 9.6%.

Table 5-4: Reproducibility of steady state and transient diffusion results for sandstone Samples R4 and R5

Steady State Analysis				Transient Analysis		
Sample	**Trial**	**c [ppm]**	**$D_{eff} \times 10^9$ [$m^2 s^{-1}$]**	**τ^2**	**L_{eff} [mm]**	**ε_{eff} [%]**
R4	Trial 1	29.7	16.8	10.4	80.7	9.7
	Trial 2	29.0	16.4	10.9	82.6	9.9
	Trial 3	27.4	16.5	11.5	84.9	9.9
	Average	28.7	16.2	11.0	82.8	9.8
	SD	1.2	0.7	0.6	2.1	0.1
R5	Trial 1	62.4	35.3	25.6	126.4	5.0
	Trial 2	69.3	39.2	25.1	125.2	5.4
	Trial 3	70.3	39.7	27.5	131.1	6.0
	Average	67.2	38.0	26.1	127.6	5.5
	SD	4.3	2.4	1.3	3.1	0.5

5.3.2 Steady state and transient gas diffusivity of sandstone samples

Sandstone samples S1 - S8 were tested in the gas diffusivity cell and the final equilibrium concentrations are summarised in Table 5-5 which includes the calculated values of the effective diffusion coefficient. It is evident that the rate of oxygen diffusion through the sample pores is higher for high permeability Samples S1 – S4 and the lower permeability samples have lower oxygen diffusion rates.

Table 5-5: Summary of diffusivity results

Steady State Analysis			Transient Analysis		
Sample	**c [ppm]**	**$D_{eff} \times 10^9$ [$m^2 s^{-1}$]**	**τ^2**	**L_{eff} [mm]**	**ε_{eff} [%]**
S1	25300 ± 300	1446 ± 6.95	5.1 ± 1.2	49.5 ± 3.5	40.1 ± 8.8
S2	11150 ± 150	638 ± 8.48	16.7 ± 2.7	110 ± 7.7	58.2 ±10.2
S3	322.3 ± 15.3	182 ± 8.65	28.0 ± 2.1	132 ± 4.7	28.3 ± 3.5
S4	464.5 ± 11.5	26.3 ± 0.65	31.1 ± 1.2	139 ± 3.9	4.5 ± 0.3
S5	325.0 ± 23.0	19.0 ± 1.30	35.6 ± 0.7	149 ± 3.3	3.6 ± 0.2
S6	213.3 ± 11.3	11.4 ± 0.64	32.4 ± 5.4	142 ± 10	2.2 ± 1.2
S7	67.3 ± 3.0	0.04 ± 0.01	26.1 ± 1.5	128 ± 3.1	0.5 ± 0.1
S8	1.3 ± 0.1	0.07 ± 0.01	14.6 ± 0.1	95.4 ± 2.1	0.1 ± 0.0

This data was analysed using the methodology summarised above and the calculated values of τ^2, L_{eff}, ε_{eff}, are presented in Table 5-5. As the permeability of the samples decreases, the effective length tends to increase and the effective porosity also decreases. It is noted that the majority of the values of ε_{eff} are lower than the total measured porosity (see Table 5.1) as might be expected. However, for high porosity samples, the values given in Table 5.1 can sometimes be even higher than the measured total porosity. The reasons for this are not clear but it is possible that the helium pycnometry method used for measuring total porosity is giving significant errors.

5.4 Pore size distribution, permeability and electrical conductivity measurements

The mercury intrusion technique described in Chapter 4 was used to measure the volume of pores penetrated with mercury at a range of applied pressures. The results of the tests for pore volume as a function of the applied pressures for sandstone samples S2, S3, S5 and S6 are shown in Figure 5-8.

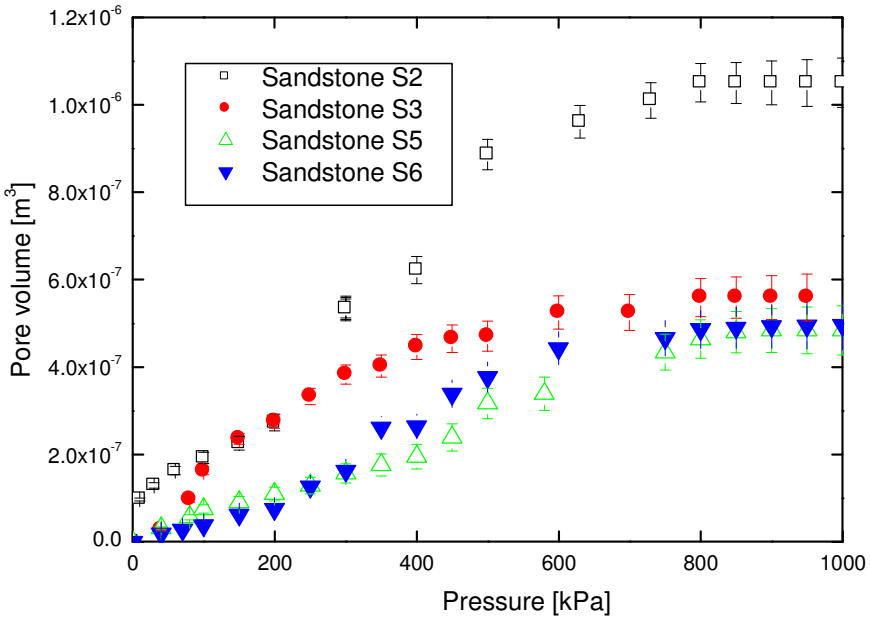


Figure 5-8: Pore volume distributions for sandstone samples S2, S3, S5 and S6

Sample S2 has the largest total pore volume of $1.0\times10^{-6} \pm 1.5\times10^{-7}$ m^3 (Figure 5-8), which when compared to the total volume of the sample gives a total porosity of 30.4 ± 4.5 %. The total pore volumes and the estimated porosities associated with the measurements are

summarised in Figure 5-9. The pore volumes of Samples S3, S5 and S6 were determined to be $5.3\times10^{-7} \pm 4.1\times10^{-8}$ m^3, $4.8\times10^{-7} \pm 2.5\times10^{-8}$ m^3 and $5.0\times10^{-7} \pm 9.7\times10^{-8}$ m^3, respectively.

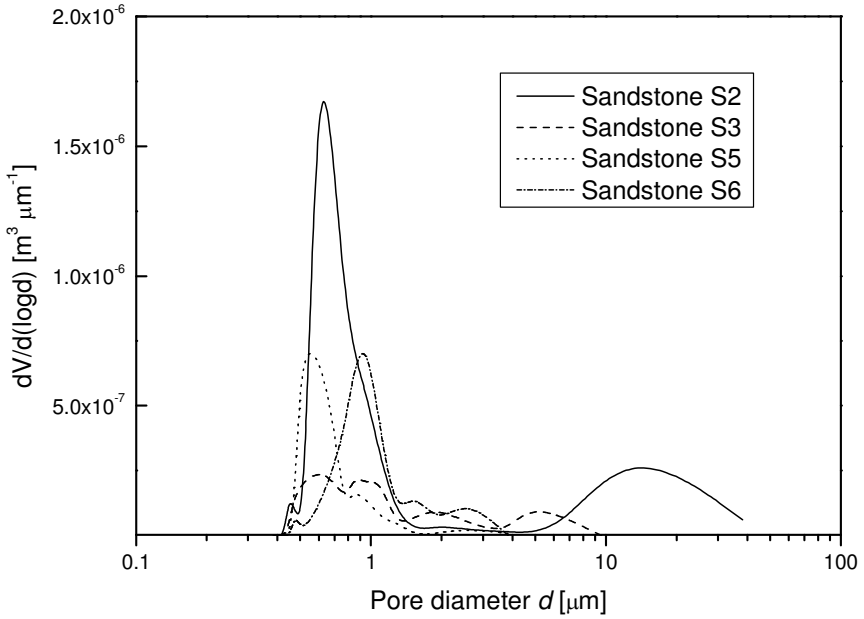


Figure 5-9: Pore size distributions of sandstone samples S2, S3, S5 and S6

The pore size distribution is defined as the pore volume increment per unit logarithm of pore diameter vs. corresponding pore diameter *d*, i.e., d*V*/d(log *d*) vs *d*. Figure 5-9 shows the pore size distributions as plots of sandstone samples S2, S3, S5 and S6. The pore size distribution of Sample S2 shown by the solid line in Figure 5-9 has two significant peaks at approximate pore diameters of 9.6 µm and 0.6 µm. Sample S3 has a much smaller distribution of pore sizes than Sample S2 but there are four significant peaks at 4.7 µm, 2.0 µm, 1.0 µm and 0.6 µm showing that there is an even distribution of pores of these diameters throughout the material. The pore size distribution of Sample S5 shows a significant peak at both 0.9 and 0.5

µm, corresponding to applied pressures of 450 and 750 kPa respectively. An example of the applied pressure as a as a function of saturation for sandstone Sample S5 is shown in Figure 5-10. It is assumed that the sample is fully saturated when an increase in applied pressure sees no further increase of mercury intrusion.

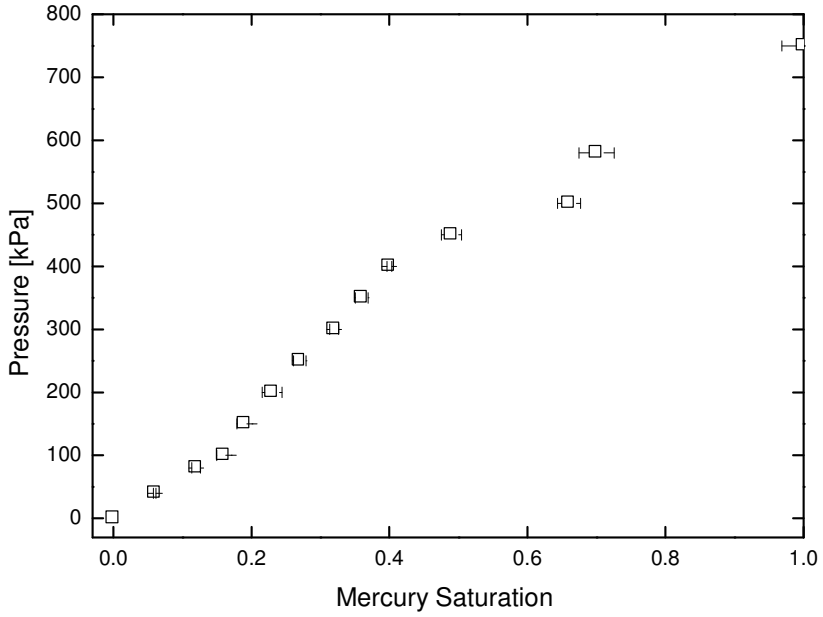


Figure 5-10: Applied pressure as a function of the mercury saturation

Permeability distributions of Samples S2, S3, S5 and S6 are shown in Figure 5-11. The permeability of Sample S2 reaches a maximum of 160 ± 18 mD and is reached at 400 kPa, which corresponds to a pore diameter of 1.0 µm, indicating there was no mercury flow through pores with larger diameters than this. With reference to the pore volume distribution, Figure 5-8 shows that at pressures higher than 400 kPa, the pore volume increases from 6.5×10^{-7} m^3 to 1.0×10^{-6} m^3 however, since there was no significant increase in permeability it

can be assumed that the pores filled at higher pressures do not contribute to flow and are non-interconnected. The permeability results for Sample S3 (Figure 5-11b) indicate that until a pressure of 250 kPa was applied there is no flow through the material. At 250 kPa, pores with a diameter of 1.5 μm were filled with mercury and this was the flow limiting pore diameter. At around 600 kPa, the permeability was 1.0×10^{-13} m^2 (= 104 mD) which was the maximum permeability reached. The total permeability of Sample S5 is 1.3 ± 0.1 mD and is reached at approximately 500 kPa, (Figure 5-11c). Since there is still mercury penetration into the pores at pressure greater than 500 kPa it is possible that pores filled at pressures higher than 500 kPa do not contribute to the flow and again, are non-interconnected. The permeability distribution of Sample S6 shows the total permeability is 1.5 ± 0.2 mD, (Figure 5-11d).

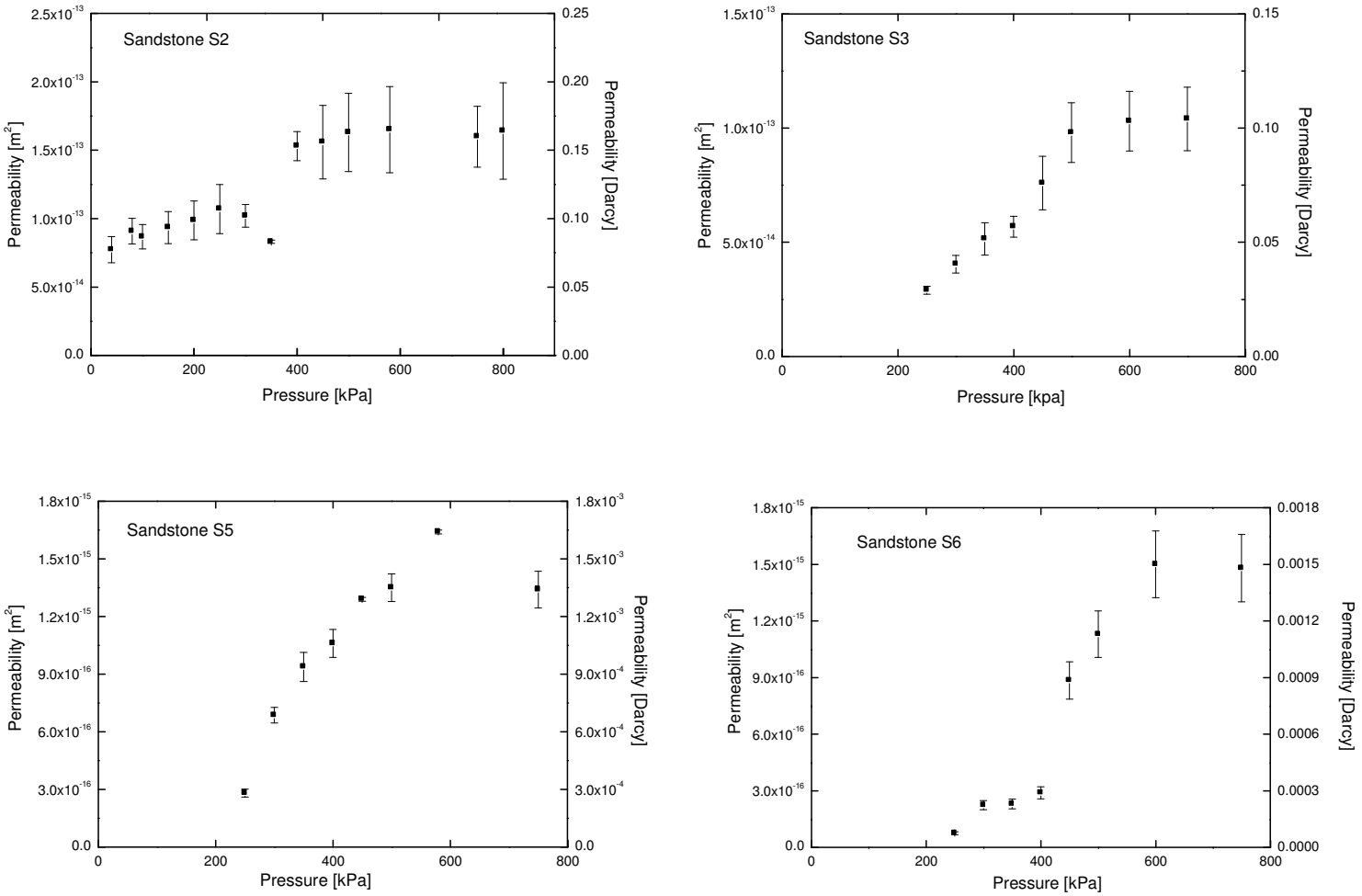


Figure 5-11a – d: Permeability distribution of SamplesS2, S3, S5 and S6.

It is interesting to combine the permeability data with the porosimetry data, allowing the permeability to be expressed as a function of pore volume occupied (exemplified in Figure 5-12 and Figure 5-13 in the form of a relative permeability curve) and also as a function of the pore size occupied. Plots of this form are shown in Figure 5-14 to Figure 5-17. Superimposed on these plots are pore size distributions of the form shown in Figure 5-9.

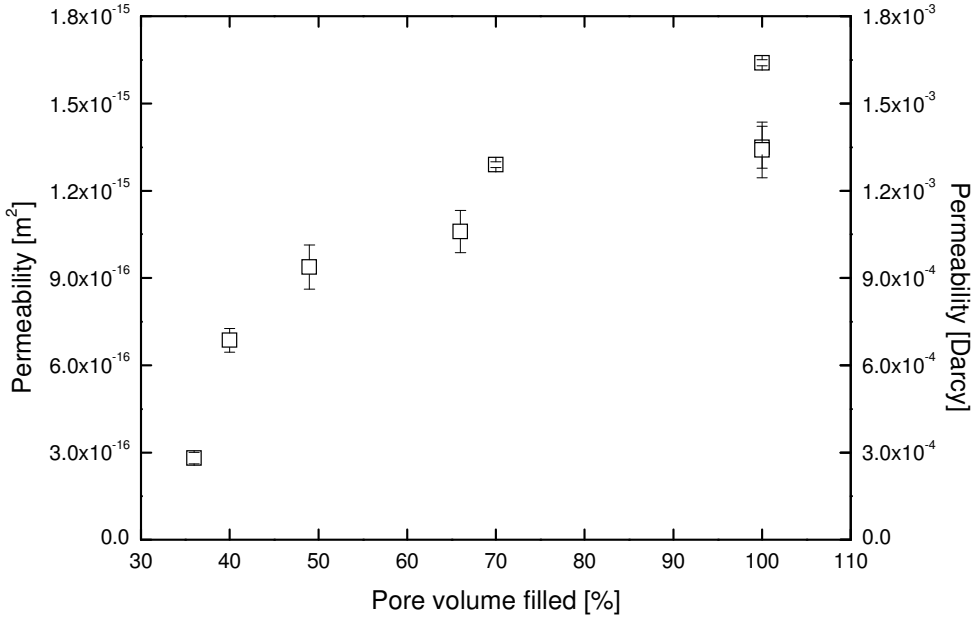


Figure 5-12: Permeability as a function of pore volume occupied for Sample S5

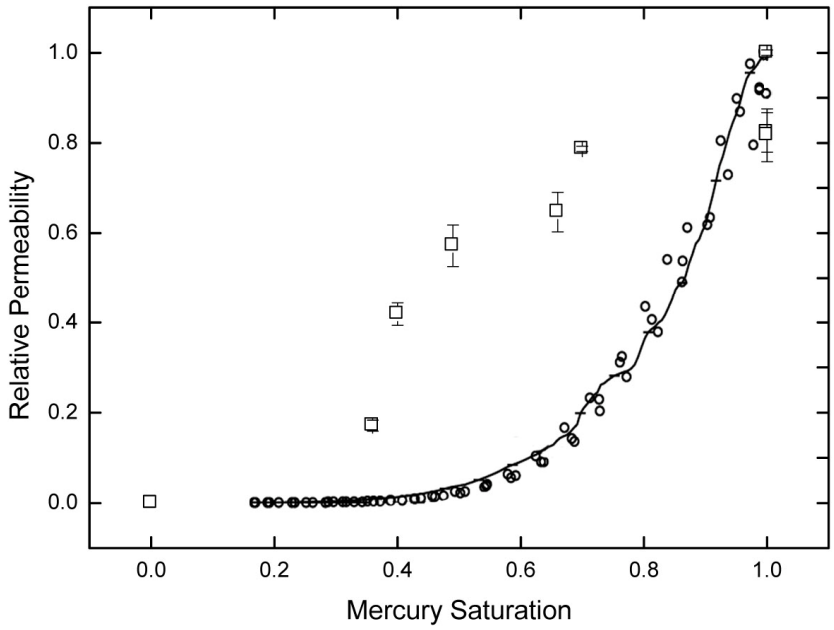


Figure 5-13: Relative permeability as a function of mercury saturation for Sample S5

Relative permeability measurements for Berea sandstone presented by Oak (1990) and predictions presented by Valvatne (2004), in the literature, exhibit a similar increase in the relative permeability as the sample reaches full saturation. The relative permeability data collected by Oak (1990) for Berea sandstone is presented in Figure 5-13 as the round circles for comparison against the results obtained using the mercury intrusion method (squares). It is interesting to note the difference in the shapes of the curves. With reference to Figure 5-13, at low liquid saturations the Oak data shows no increase in the relative permeability, at approximately 50% saturation the relative permeability increases rapidly. In contrast, the mercury permeability results show a rapid increase in the relative permeability between 40

and 60% saturation. The apparent shift to the left of the mercury data may imply that in the mercury intrusion work, it is possible to detect flow at lower fluid saturations.

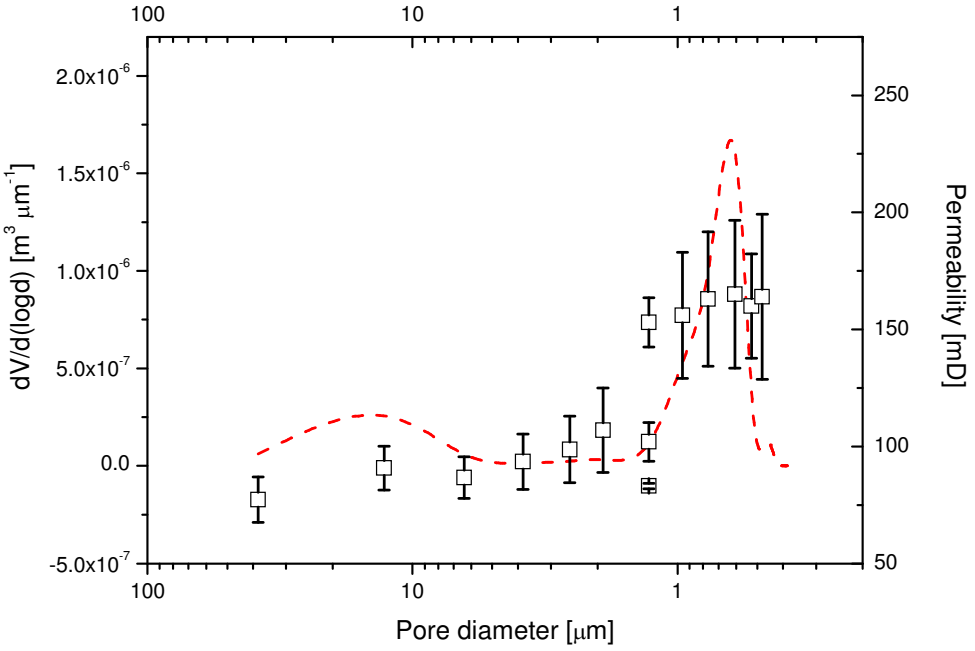


Figure 5-14: Pore size and permeability distribution of Sample S2

Figure 5-14 shows the results for Sample S2. Large pores of approximately 10 µm are partially interconnected as there is evidence of fluid flow when they are filled. However, it is possible to deduce from Figure 5-11a, that the pores are only partially interconnected since the permeability is relatively low compared to the maximum permeability of the sample (about 75 mD). When the smaller pores are filled the permeability rapidly increases to the maximum value and can be assumed to be the main contributors to the total permeability.

When the pores of 0.8 µm diameter are filled, the permeability reaches its maximum value and the mercury in the porous medium has reached its maximum connectivity.

Figure 5-15 shows the distributions of Sample S3. The first peak of the pore size distribution represents large pores of diameter 4.7 µm that are not interconnected, perhaps dead end or blind pores since there is no flow when these pores are filled. The second peak at 2.0 µm corresponds to the onset of flow through the sample. These pores are hence connected. The permeability increases rapidly when 1.0 µm pores are penetrated and reached the maximum permeability when pores with a diameter of 0.6 µm are filled. We can deduce that the pores of 1.0 µm and smaller are the main interconnected pores and are the main contributors to flow.

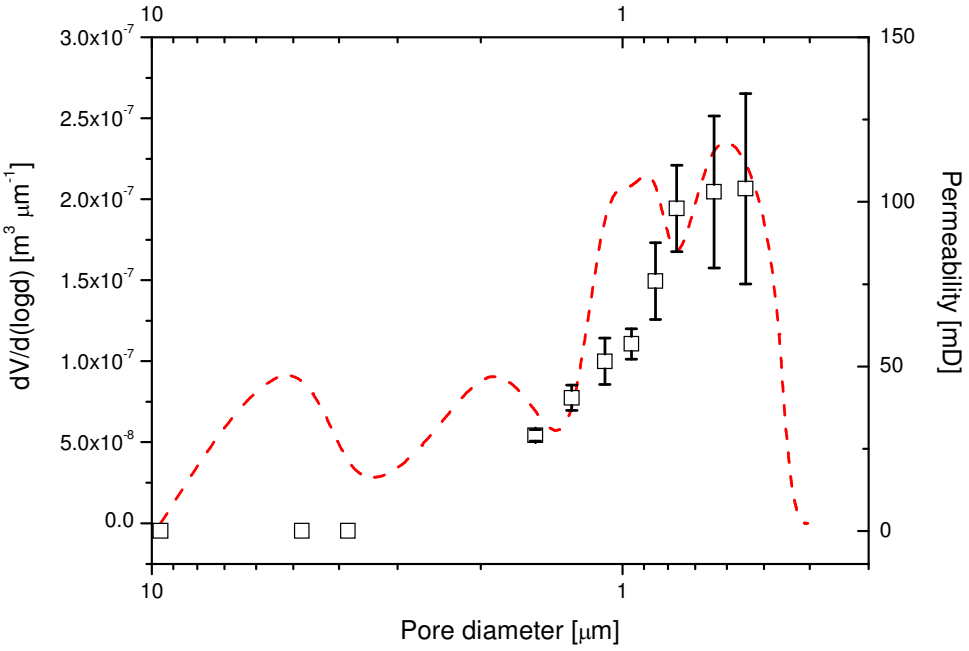


Figure 5-15: Pore size and permeability distribution of Sample S3

The pore size and permeability distribution of Sample S5 are shown in Figure 5-16. The maximum permeability is reached when pores of 0.9 µm diameter are filled. The permeability of Sample S5 increases steadily when pores between of 2.0 µm and 0.9 µm diameters are penetrated, since there is only a small pore volume being filled we can assume that the permeability is increasing due to the formation of mercury interconnections through the larger pores as the pressure is increased. The structure appears to have reached maximum interconnectivity when the maximum permeability is reached, this occurs when the pores of 0.4 µm are filled.

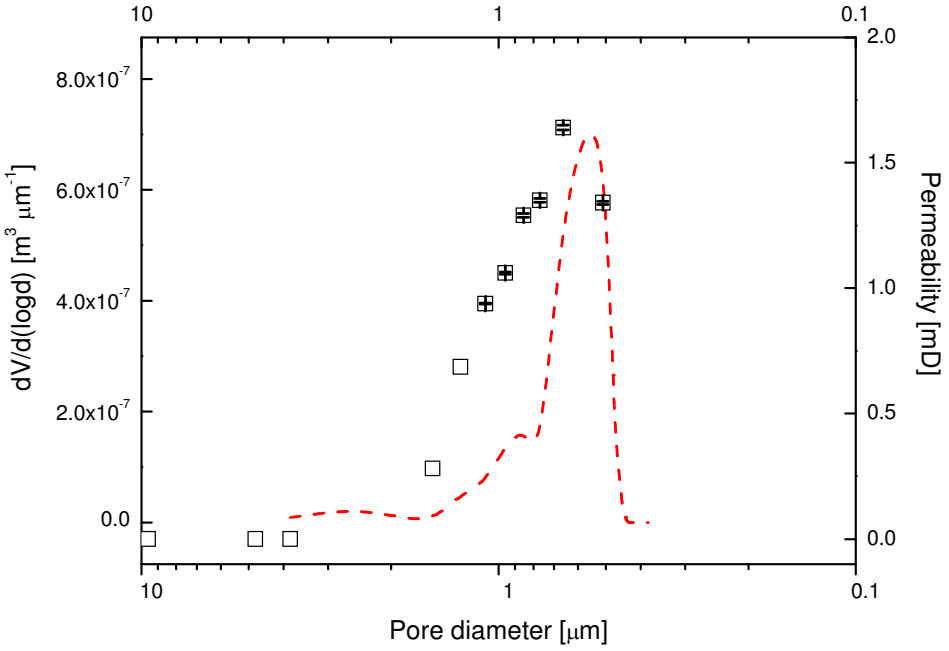


Figure 5-16: Pore size and permeability distribution of Sample S5

Figure 5-17 represents results obtained from Sample S6. There are a number of large pores of 3.0 µm and 1.5 µm diameter however these are not interconnected and no flow occurs

through these pores. When pores of 1.0 µm are filled, the permeability rapidly increases to maximum value indicating that the total permeability is mainly affected by the interconnection of pores of 1.0 µm diameter.

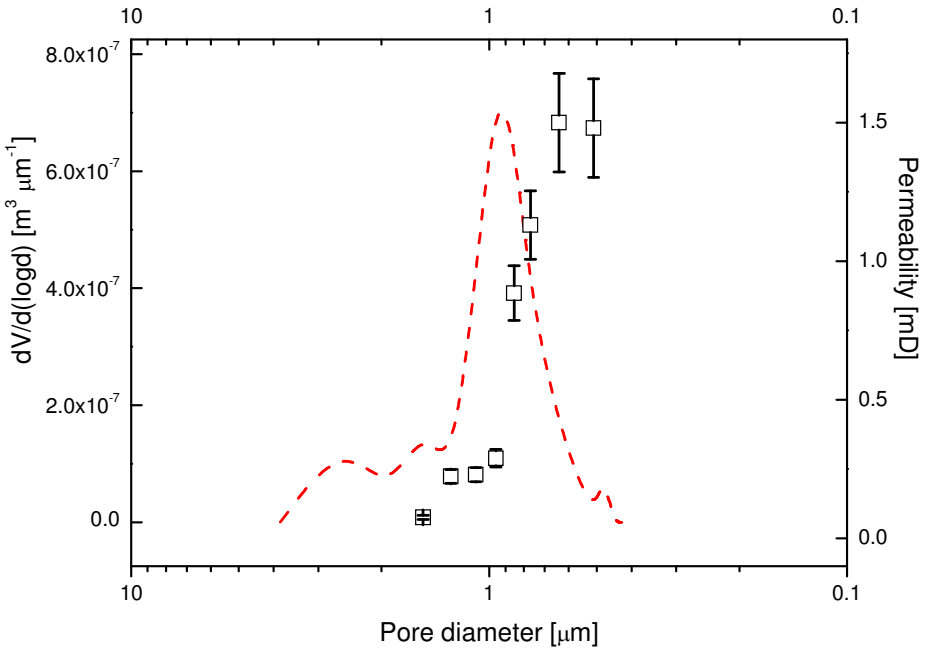


Figure 5-17: Pore size and permeability distribution of Sample S6

The results for typical mercury conductance experiments are shown in Figure 5.15 in the form of the conductivity ratio r_{Cp} as a function of pressure; at the highest pressure, all of the pores are filled with mercury in this case. The limiting value of r_{Cp} at the highest pressure was around 0.0105 which compares with an r_D value of 0.0353 for the same values. As will be seen, the values are in reasonable agreement. What is gained additionally from the conductance measurements is the information about which pores are contributing to the diffusivity.

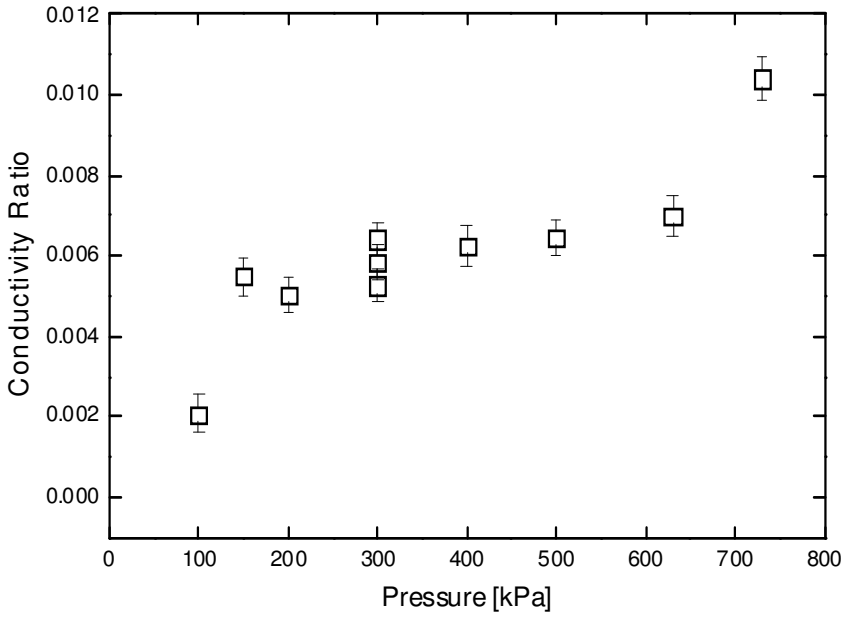


Figure 5-18: Plot of conductivity ratio r_{Cp} as a function of applied pressure for Sample S2

Using steady state and transient diffusion experiments, it is possible to estimate the effective porosity and the effective pore length (tortuosity) as described above; briefly, this involves measuring the diffusivity ratio r_D, estimating effective pore length L_{eff} by fitting Equation 2.25 to the transient diffusion data and then calculating ε_{eff} from Equation 2.22. In the case of the mercury conductivity measurements, we have measurements of r_{Cp} and, when the pore space is fully occupied by mercury, it should be the case that $r_{Cp} = r_D$. Indeed, subject to the limitations of experimental accuracy, this equality does indeed apply. However, conductivity data have both a disadvantage and an advantage relative to the diffusivity data. The disadvantage is that there is no measurement equivalent to the transient diffusion

measurement in the conduction case. The advantage is that values of r_{Cp} are obtained over a range of pressures and it is thus possible to assess the contributions the various pores make to the overall conductivity (and, hence, diffusivity). This information is, in essence, of the same type as that shown in Figure 5-14 to Figure 5-17 above for permeability. Figure 5-18 and Figure 5-19 show data for r_{Cp} as a function of pore size penetrated for Samples S5 and S6, respectively. As in the case of permeability, rapid changes in relative conductivity (and, by analogy, diffusivity) occur over small ranges of pore size when there is a rapid increase in pore size penetrated for a similar range.

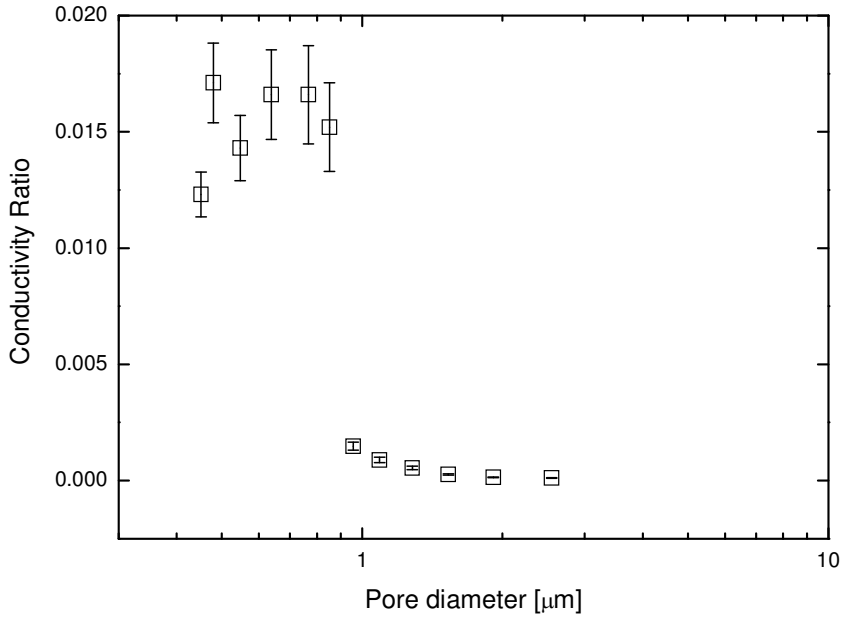


Figure 5-19: Relative conductivity r_{Cp} as a function of pore size penetrated for Sample S5

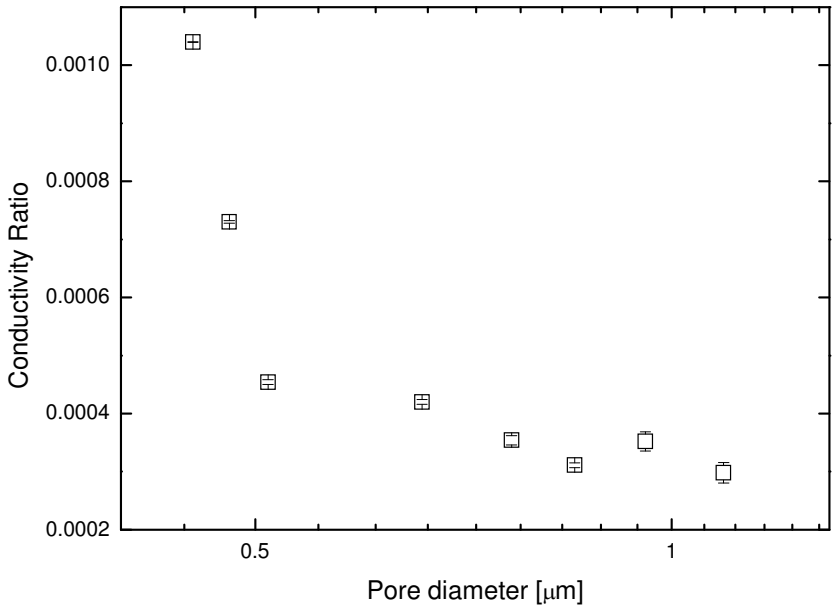


Figure 5-20: Relative conductivity r_{Cp} as a function of pore size penetrated for Sample S6

5.5 Image analysis of thin-sections of sandstone samples

5.5.1 Structural interpretation of porous solids

Thin-sections of sandstone Samples S1 – S8 were prepared by first evacuating the sample using a vacuum system and then allowing dyed resin to penetrate the evacuated pores. The sample was then cut into thin-sections using a diamond blade on a high speed saw. It was mounted in a glass slide and ground down to the desired thickness. The thin-sections were studied using a reflective microscope. The microscope images were analysed using software, *UTHSCSA Image Tool© Version 3.00*, which enabled direct measurements of pore

diameters and perimeters. It was possible to measure the perimeter of individual pore/grain interfaces and also the total pore area. The pore area was used to calculate the specific porosity of the samples. Equation 2.7 was used to determine the specific surface area which was then used in Equation 2.6 to calculate a value of permeability. Twenty images were analysed for each sample as recommended by Solymar & Fabriciu (1999). Figure 5-21a and b are an example of the images obtained from thin-section analysis and show microscope images of thin-sections that are representative of the sandstone Sample S1. The blue parts of the images represent the pores as the resin was dyed blue before impregnation. The yellow parts are the sand grains which make up the solid volume of the sandstone.

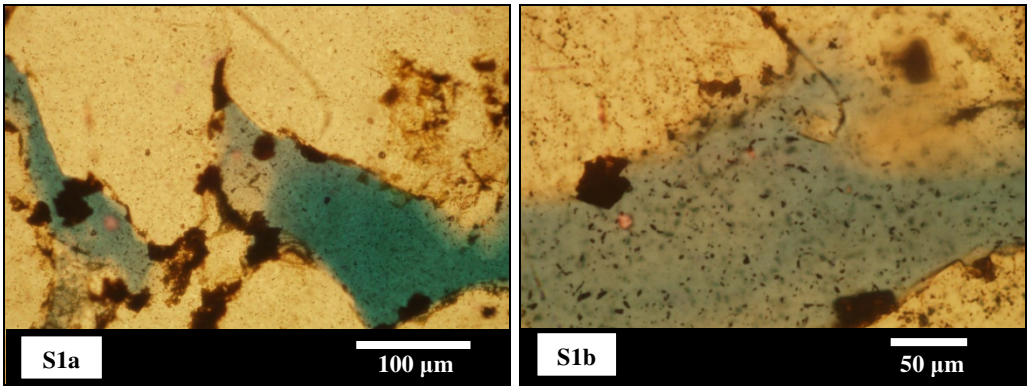


Figure 5-21a and b: Microscope images of sandstone Sample S1

The ratio of the pore space to the grain space was used to calculate the porosity of the section of the sample in each image. The average porosity of Sample S1 was found to be 19.6 % ± 2.7 %. The permeability from the Carman-Kozeny equation (Equation 2.6) was found to be 355 ± 23 mD. The image analysis results for Samples S1 to S8 are presented in Figure 5-21.

The thin-section images of sandstone Samples S2 – S8 are given in *Appendix VII* for reference.

Table 5-6: Summary of the results of porosity, specific surface, pore diameter and permeability obtained from analysis of thin-section microscopic images

Sample	Porosity [%]	Ss [μm^{-1}]	d [µm]	k_{image} [mD]
S1	19.6 ± 2.70	0.07 ± 0.01	84.8 ± 4.00	355 ± 23.0
S2	18.9 ± 4.68	0.07 ± 0.03	120 ± 90.4	251 ± 24.5
S3	11.8 ± 4.61	0.05 ± 0.01	115 ± 21.6	54.7 ± 21.8
S4	7.79 ± 3.33	0.12 ± 0.05	55.6 ± 20.4	3.06 ± 1.29
S5	4.40 ± 0.53	0.08 ± 0.03	80.4 ± 26.3	0.10 ± 0.03
S6	4.36 ± 0.93	0.08 ± 0.03	80.4 ± 26.3	0.10 ± 0.03
S7	2.11 ± 1.56	0.78 ± 0.83	43.4 ± 46.0	0.02 ± 0.01
S8	0.94 ± 0.35	1.01 ± 0.84	56.4 ± 45.9	0.03 ± 0.01

5.6 Discussion of the results obtained using the integrated methods and image analysis

5.6.1 Permeability results

The permeability values obtained using the gas and mercury permeability methods ranged from 1050 – 0.24 mD. This is in very good agreement with measurements made on Berea sandstone by Baraka-Lokmane *et al.* (2007) and Siddiqui *et al*. (2002). Permeability predictions from image analysis give values in a similar range. The permeability measurements made using the integrated gas and mercury apparatus are presented in Table 5-7.

Table 5-7: A summary of the permeability measurements and predictions of sandstone Samples S1 – S8. k_{gas} = permeability measured using gas, k_{Hg} = permeability measured using mercury, k_{turb} = permeability predicted from turbulent analysis, k_{image} = permeability predictions from image analysis and K_0 = Knudsen diffusion coefficient

Sample	k_{gas} [mD]	k_{Hg} [mD]	k_{turb} [mD]	k_{image} [mD]	K_0 [m]
S1	1050 ± 166	-	3300 ± 182	355 ± 230	$1.08\times10^{-5} \pm 1.68\times10^{-6}$
S2	350 ± 20.7	160 ± 18	602 ± 4.98	251 ± 24.5	$1.45\times10^{-6} \pm 3.41\times10^{-7}$
S3	126 ± 2.98	104 ± 14	160 ± 4.53	54.7 ± 21.8	$1.10\times10^{-7} \pm 4.61\times10^{-8}$
S4	9.81 ± 0.26	-	18.2 ± 0.32	3.06 ± 1.29	$5.14\times10^{-8} \pm 3.11\times10^{-9}$
S5	1.38 ± 0.11	1.3 ± 0.1	5.35 ± 0.28	0.10 ± 0.03	$2.54\times10^{-8} \pm 1.99\times10^{-9}$
S6	1.11 ± 0.04	1.5 ± 0.2	2.10 ± 0.02	0.10 ± 0.03	$8.71\times10^{-9} \pm 8.58\times10^{-10}$
S7	0.37 ± 0.01	-	1.17 ± 0.11	0.02 ± 0.01	$5.16\times10^{-9} \pm 1.07\times10^{-10}$
S8	0.24 ± 0.01	-	1.34 ± 0.02	0.03 ± 0.01	$8.46\times10^{-9} \pm 2.36\times10^{-10}$

The general trend was as expected— that the permeability of the porous samples is somewhat dependent on the porosity. However, the porosity does not necessarily govern the permeability. For example Samples S1 and S2 have similar porosity values of 19.6 % and 18.9 %, respectively, measured from images but the gas and mercury permeability shows a larger variation. Figure 5-22 shows the comparison of the gas and mercury permeability measurements. It also includes permeability values form the turbulent investigation and predictions from thin-section image analysis. Permeability values predicted from image analysis are in approximate agreement with measured permeabilities for Samples S1 – S3, however the predictions are much lower than both gas and mercury permeability measurements for Samples S5 – S8. This may be due to the limitation of identification of pores that are connected since the images are 2-dimensional showing that permeability predictions derived from 2-dimensional section images are not necessarily a good

representation of the sample, especially in the case of very low permeability samples such as Samples S5 – S8.

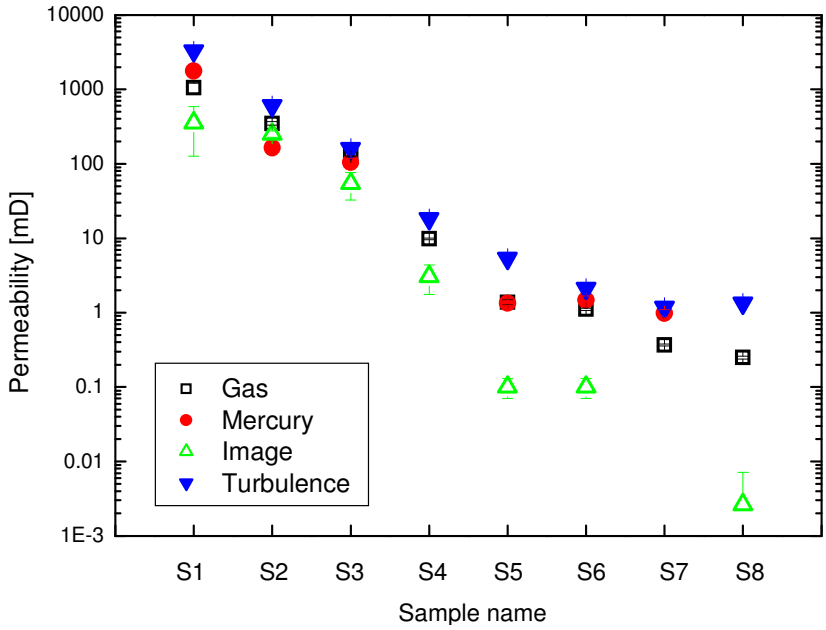


Figure 5-22: Permeability measurements obtained from gas and mercury techniques and predictions from image analysis and turbulent effects

5.6.2 K_0 the slip coefficient

The slip coefficients were measured and the results are presented in Table 5-7. The values range from 1.08×10^{-5} m for Sample S1 to 5.14×10^{-9} m for Sample S4. The slip coefficient is dependent on the pore diameter since slip occurs due to collisions of gas molecules with the walls of the pores. It seems that there is scope for more investigation of the slip coefficient of porous solids and how the values are quantified. In this case, it can be assumed that gas

transport by Knudsen diffusion is negligible in the case of the permeability measurements in this investigation.

5.6.3 Turbulent effects on gas permeability

The analysis of turbulent gas flow identified the occurrence of turbulent flow in the case of sandstone Samples S1 – S8 (turbulent data is presented in *Appendix VI* for reference). The linear relationships between C and $V\left(\frac{dp_2}{dt}\right)$ indicate that turbulence is present in the pores during gas permeability experiments. The permeability was calculated from the intercept and the values are plotted in Figure 5-22. The values of permeability calculated from the turbulence should be similar to the viscous permeability k (as observed, for instance, by Hewitt, 1961) The results show fairly good agreement between k_{gas} and k_{turb}, with the exception of Sample S1 and Sample S2, for which the permeabilities were over predicted; this may reflect the fact that there are multiple groups of pores which are behaving differently (see Equation 5.5).

5.6.4 Permeability and pore size distribution

The permeability and pore size distributions of sandstone Samples S1 – S8 were determined using the mercury porosimetry and mercury permeability technique. The total permeability results have been addressed and used as a comparison with the gas permeability results discussed in the previous *Section 5.6.1.* The permeability distribution results give an insight to the ability of the material to transmit fluid. By combining the permeability distribution

results with the measurements of the pore size distribution, an informative overview into the structure and flow properties of a porous solid is obtained. These results provide a detailed insight into the porous structure and the effect that pores of specific diameter have on the permeability. It is possible to deduce the diameter of pores that are interconnected and of those pores that are not interconnected, due the effect on permeability of the specific pores. The technique also enables the identification of specific pore diameters that have most effect on the permeability and also which of the pores are blocked and do not allow fluid flow. This in itself is an extremely useful analytical technique for the investigation of porous structures and the effect of the structure on permeability.

5.6.5 Effective diffusion coefficient and electrical conductivity

The electrical conductivity of mercury forced into the pores of the samples and effective diffusion coefficients were measured. It is interesting to compare the values obtained for the ratio of the diffusivity to the free gas diffusivity (r_D) with the value obtained for the ratio of sample conductivity to mercury conductivity (r_{Cp}) for the case when the applied pressure is high enough for the mercury to have penetrated all the pores. In principle, since the diffusion and conductance processes are analogous, r_{Cp} should equal r_D at the high applied pressure limit. Values of r_D and the limiting values of r_{Cp} are listed in Table 5.8. As will be seen, the values agree reasonably well, bearing in mind the complexities and uncertainties involved in the techniques.

Table 5-8: Comparison of values of r_D and r_{Cp} obtained from diffusion and from conductivity at high applied pressure respectively

Sample	Ratio of gas diffusivity to free space value r_D	Ratio of conductivity of sample impregnated with mercury at high pressure to that of pure mercury r_{Cp}
S1	$7.99\times10^{-2} \pm 9.37\times10^{-4}$	-
S2	$3.53\times10^{-2} \pm 4.68\times10^{-4}$	$1.04\times10^{-2} \pm 2.23\times10^{-3}$
S3	$1.01\times10^{-2} \pm 4.78\times10^{-4}$	$7.13\times10^{-3} \pm 2.37\times10^{-4}$
S4	$1.45\times10^{-3} \pm 3.59\times10^{-5}$	-
S5	$1.05\times10^{-3} \pm 7.18\times10^{-5}$	$1.23\times10^{-2} \pm 9.58\times10^{-4}$
S6	$6.31\times10^{-4} \pm 3.53\times10^{-5}$	$1.04\times10^{-3} \pm 6.52\times10^{-7}$
S7	$1.95\times10^{-6} \pm 2.02\times10^{-4}$	-
S8	$3.96\times10^{-6} \pm 3.12\times10^{-7}$	-

5.7 Summary of the integrated methods and their application to porous sandstone

The integrated gas and integrated mercury apparatus were used to measure flow and structural properties of porous sandstone samples. Thin-section analysis was also carried out to aid confirmation of the measurements obtained. The main findings are summarised as follows:

- The gas and mercury permeability measurements were consistent with each other however; permeability predictions from image analysis always underestimated the permeability.

- Permeability and pore size distribution together give a very good graphical representation of the effect of pore diameters on permeability. Mercury conductivity measurements together with pore size distributions give similar indications of the role of the various pores in the diffusion process.
- Effective pore lengths determined by combining steady state and transient diffusion measurements range from double to six times the actual sample length.
- Thin-section image analysis provides a good visual representation of the samples.
- The integrated methods have been successfully operated to produce reliable, reproducible results of permeability, diffusivity, conductance and pore size distribution and of the characteristics derived from these parameters.

CHAPTER 6

APPLICATION OF INTEGRATED METHODS TO THE STUDY OF POROUS MATERIALS

II: POLYMER FOAMS

Polymer foams produced by the polymerisation of emulsion templates are an important class of materials for a wide range of applications. Typically, emulsion templates consist of an aqueous phase and a monomer phase. The aqueous (internal) phase is in the form of droplets and the monomer phase is the continuous phase between the droplets. Until recently it was thought that open porous polymer foams could only be produced from the polymerisation of high internal phase emulsion (HIPE) templates. Improvement of the poor mechanical performance, characteristic of such polymer foams (polyHIPEs), was achieved by increasing the material density of the polymer foam; however, this required a reduction in the internal phase volume of the emulsion template and therefore reduction of porosity. Polymerisation of emulsion templates with a reduced internal phase volumes resulted in the production of poly(medium internal phase emulsions) (polyMIPEs) and poly(low internal phase emulsions) (polyLIPEs). Compression tests show that mechanical properties were improved as the material density was increased. Development of these improved polymer foam materials is being pursued at Imperial College and the objective of the work described in this Chapter

was to improve the background knowledge of these materials by gas and mercury integrated measurements using the new integrated gas and mercury apparatus.

6.1 Introduction to polymer foams

Open porous polymer foams can be produced by polymerisation of an emulsion template. Typically, emulsion templates for the production of polymer foams consist of an aqueous phase and a monomer phase. The aqueous (internal) phase is in the form of droplets and the monomer phase is the continuous phase between the droplets. Figure 6-1 is an illustration identifying the dispersion of the internal phase in the continuous monomer phase.

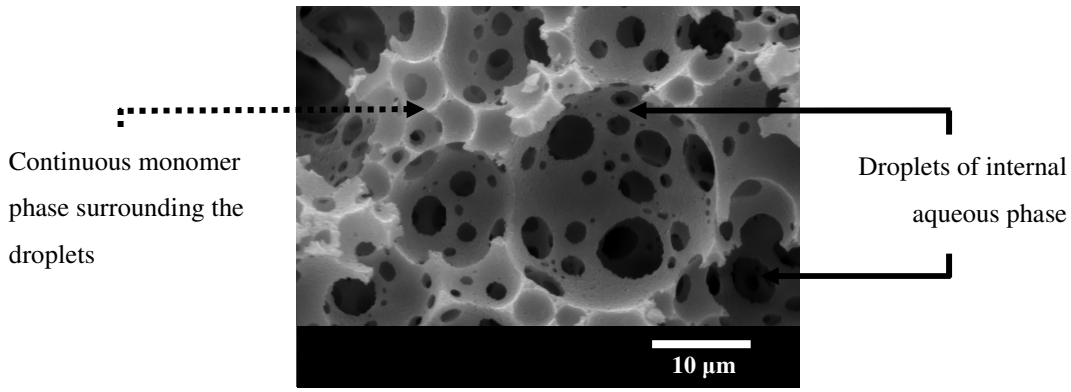


Figure 6-1: Illustration of the dispersion of the internal phase in the continuous monomer phase to form an emulsion template

Polymerisation of the continuous phase of the emulsion results in the formation of an open porous polymer foam with the structure determined by the emulsion template. Pores are formed in the space of the internal phase droplets and pore throats form during polymerisation in the area of contact points between neighbouring droplets (Cameron *et al.*,

1996, Cameron, 2005). Until recently it was thought that open porous polymer foams could only be produced from the polymerisation of *high internal phase* emulsion (HIPE) templates with an internal phase level exceeding 74 vol.-%, to form *polyHIPES*.

There are numerous potential applications for polyHIPEs including scaffolds for tissue engineering and monolithic polymer supports for heterogeneous catalysis and ion exchange modules (Christenson *et al.,* 2007, Krajnc *et al.,* 2005, Ottens *et al.,* 2000, Silverstein *et al.,* 2005, Grosse *et al.,* 2007, Wakeman *et al.,* 1998 and Krajnc *et al.,* 2006). The permeability of scaffolds for tissue engineering and cell cultures is an important parameter as it affects the flow of nutrients necessary for cell growth. The permeability of porous catalyst supports will affect the flow of reagents and hence the reaction rates. It has also been shown that ion-exchange selectivity is dependent on permeability, so it is important to be able to quantify the flow properties in these applications. Generally polyHIPE foams have poor mechanical properties which impose severe limitations on the uses and applications of the material. In this investigation, it is hypothesised that the improvement of the poor mechanical performance can be achieved simply by increasing the material density of the polymer foam. However, the effect on the porosity and permeability remains extremely important, since polyHIPEs are typically of interest due to their relatively low material density, interconnected porous structure and high and controllable porosity but an open porous structure is still desirable.

An increase in the material density however, required a reduction of the internal phase volume of the emulsion template to below 74 vol.-%. To test the hypothesis, polymer foams

were prepared from emulsion templates with a reduced internal phase volume ranging from 80 vol.-% to 25 vol.-%. This resulted in the production of a collection of polyHIPEs, poly(medium internal phase emulsions) and poly(low internal phase emulsions) (polyMIPEs and polyLIPEs). Compression tests show that as predicted, the mechanical properties improved as the material density was increased. The gaseous mass transport and mercury penetration techniques described in the earlier Chapters of this thesis were used to characterise these polymer foams to test whether the materials produced had open porous structures.

6.2 Experimental

Two sets of samples were prepared, Set 1 with internal phase volumes ranging from 84 vol.-% to 60 vol.-% produced from emulsion templates stabilised by the surfactant Hypermer 2296 and Set 2 with internal phase volumes ranging from 60 vol.-% to 25 vol.-% produced from emulsion templates formulated using a mixture of surfactants Hypermer 2296 and Hypermer B246sf. The samples were characterised using SEM analysis and mechanical tests. Gas and mercury permeability measurements were made according to the procedures described in Chapters 3 and 4.

6.2.1 Porous polymer foams and the method used for their production

Open porous polymer foams were produced by the polymerisation of emulsion templates. The emulsion templates for the production of polymer foams consisted of an aqueous phase and a monomer phase. The aqueous (internal or dispersed) phase is in the form of droplets

and the monomer phase is the continuous phase between the droplets. Polymerisation of the continuous phase of the emulsion results in the formation of an open porous polymer foam with the structure determined by the emulsion template.

Materials and methods for the production of porous polymers

Styrene, divinylbenzene (DVB), $CaCl_2 \cdot 2H_2O$ and α,α'-azoisobutyronitrile (AIBN) were purchased from Sigma Aldrich (Gillingham, UK). Non-ionic polymeric surfactants Hypermer 2296 (Hydrophilic Lipophilic Balance (HLB) = 4.9) and Hypermer B246sf (HLB = 6.0) were kindly supplied by Croda (Wirral, UK). All chemicals were used as received. The epoxy resins Araldite® Precision Adhesive and Araldite® 2020 as well as the silicone mould release spray Electrolube were purchased from RS Components Ltd. (Corby, UK).

6.2.2 Preparation of polymer foams by polymerisation of the continuous phase of emulsion templates

The general procedure to prepare 50 mL emulsions consisting of a continuous organic phase and an internal aqueous phase is described below. The continuous organic phase contained 20 vol.-% styrene, 60 vol.-% divinylbenzene, 20 vol.-% surfactant and 1 mol.-% of the initiator AIBN with respect to the monomers. Hypermer 2296 was used as the surfactant to stabilise emulsion templates with internal phase volumes ranging from 84 vol.-% - 60 vol.-%. It was found that the emulsions prepared with less than 60 vol.-% internal phase were unstable when solely stabilised by Hypermer 2296. A surfactant mixture of Hypermer 2296 and Hypermer B246sf (1:1 by weight) was found to be suitable to stabilise emulsions with

internal phase volumes ranging from 60 vol.-% - 25 vol.-%. The continuous organic phase was mixed in a reaction vessel fitted with an addition funnel and a glass paddle rod connected to an overhead stirrer. The stirring rate of 400 rpm was kept constant during the preparation of the emulsion. The aqueous internal phase, containing $CaCl_2 \cdot 2H_2O$ as electrolyte, was slowly added to the stirring reagents. In order to create finely dispersed droplets the stirring rate was increased to 2000 rpm for 10 minutes. The resulting emulsions were transferred into free standing polypropylene centrifuge tubes (Fisherbrand). Each centrifuge tube was sealed with a lid and heated to 70°C in an oven for 24 h. The polymerised foams were removed from the centrifuge tubes and purified by Soxhlet extraction first with distilled water followed by methanol. The samples were dried to constant weight in a vacuum oven at 80°C. The samples that were prepared and the sample codes used are summarised in Table 6-1.

Table 6-1: Summary of the polymer foams produced and the naming system

Sample		Surfactant	Internal Phase Volume [vol.-%]
1	PolyHIPE1	Hypermer 2296	84
	PolyHIPE2		74
	PolyMIPE3		64
	PolyMIPE4		60
2	PolyMIPE5	Hypermer 2296 + B246sf	60
	PolyMIPE6		40
	PolyMIPE7		34
	PolyLIPE8		25

6.3 Characterisation methods

6.3.1 Scanning electron microscopy (SEM)

The average pore and pore throat diameter of the polymer foams were determined using scanning electron microscopy (Jeol *JSM 5610 LV*, Jeol Ltd., Welwyn Garden City, UK). Prior to observation, approximately 1 cm^3 of each sample was mounted on a sample holder and sputtered with gold for 120 s in argon atmosphere using an *Emitech K550* (Emitech Ltd., Ashford, UK) to ensure sufficient electrical conductivity. SEM images were analysed with the software, *UTHSCSA Image Tool© Version 3.00*, which enabled direct measurements of pore diameters from the images. At least 200 pore and pore throat diameters were measured to make a reasonable estimation of the average pore and pore throat distribution.

6.3.2 Material and foam density measurements of porous polymers

Material and foam density measurements were performed using pycnometry (*GeoPyc 1360*, Micrometrics Ltd. Dunstable, UK) in conjunction with measurements obtained of the material density from helium displacement pycnometry (*AccuPyc 1330*, Micrometrics Ltd. Dunstable, UK). The porosity ε was calculated using Equation 6.1:

$$\varepsilon = \left(1 - \frac{m}{V\rho_m}\right) \times 100\% \qquad 6.1$$

where m is the sample mass, V is the sample volume and ρ_m is the material density.

6.3.3 Mechanical testing of porous polymers

Compression testing of the cylindrical samples of porous polymers was carried out using a *Lloyds Universal Testing Machine* (Lloyds EZ50, Lloyds Instruments Ltd., Fareham, UK). The samples were loaded at a rate of displacement of 1 mm min^{-1} until a displacement of 5 mm was reached. The elastic modulus is the slope of the initial linear region of the stress-strain plots. The crush strength was defined as the maximum strength at the end of the initial linear elastic region.

6.4 Results and discussion of structural and permeability investigations of polymer foams

The average material density of all macroporous polymers is 1.17 ± 0.01 g cm^{-3}. The foam densities and the porosities of the macroporous polymers are presented in Table 6-2. As the internal phase volume of the emulsion template was increased, the foam density of the resulting macroporous polymers decreased and the porosity increased. Even under the assumption that the entire internal phase and the surfactant was removed during the purification and drying steps, the porosities of all porous polymers are higher than expected. This indicates that the polymerisation was incomplete.

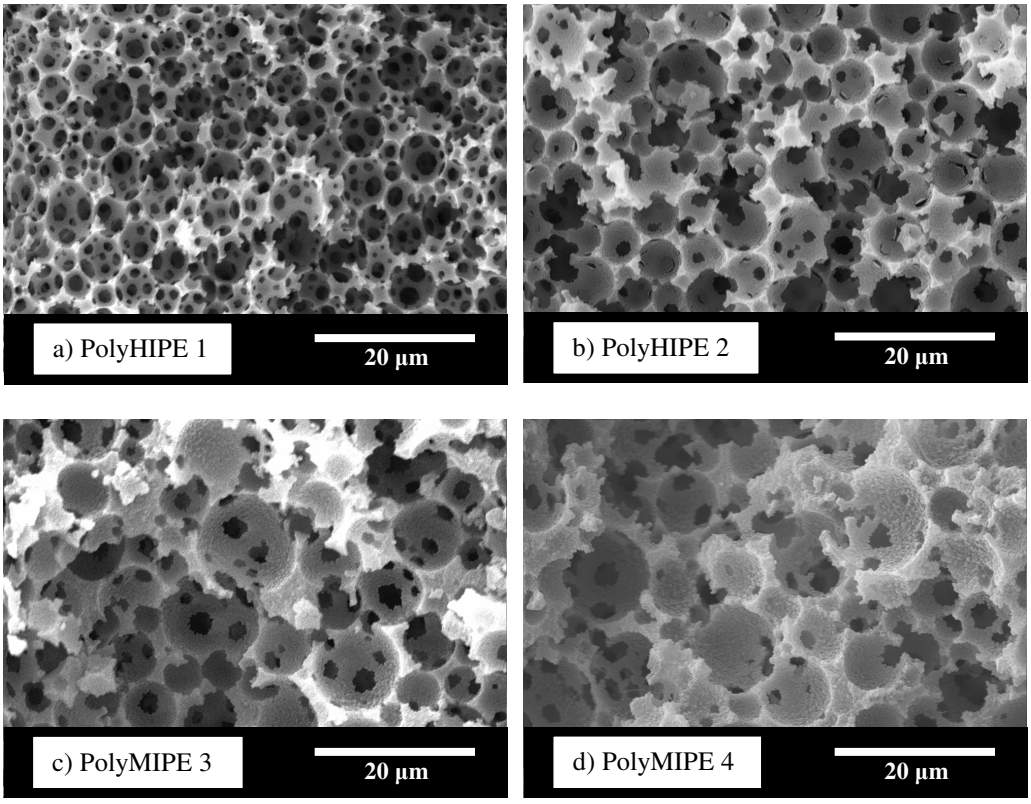


Figure 6-2a to d: SEM images of polyHIPEs to polyMIPEs 1 to 4

Representative SEM images of the Set 1 samples are shown in Figure 6-2a – d. The average pore diameters and pore throat diameters determined using SEM image analysis are summarised in Table 6-2. Figure 6-2a shows the characteristic open interconnected structure of a polyHIPE, it is clear that each pore of polyHIPE **1** is connected to the neighbouring pores by numerous pore throats. Similarly, polyHIPE **2** has an open porous structure with a considerable amount of interconnecting pore throats (Figure 6-2b). PolyMIPEs **3** and **4** (Figure 6-2and Figure 6-2d) have slightly larger pores than polyHIPEs **1** and **2**. There is evidence of a reduction in the number of interconnecting pore throats; however the average pore throat sizes are notably larger than those of polyHIPE **1**. The polyMIPEs and polyLIPE of Set 2 also have an open porous structure.

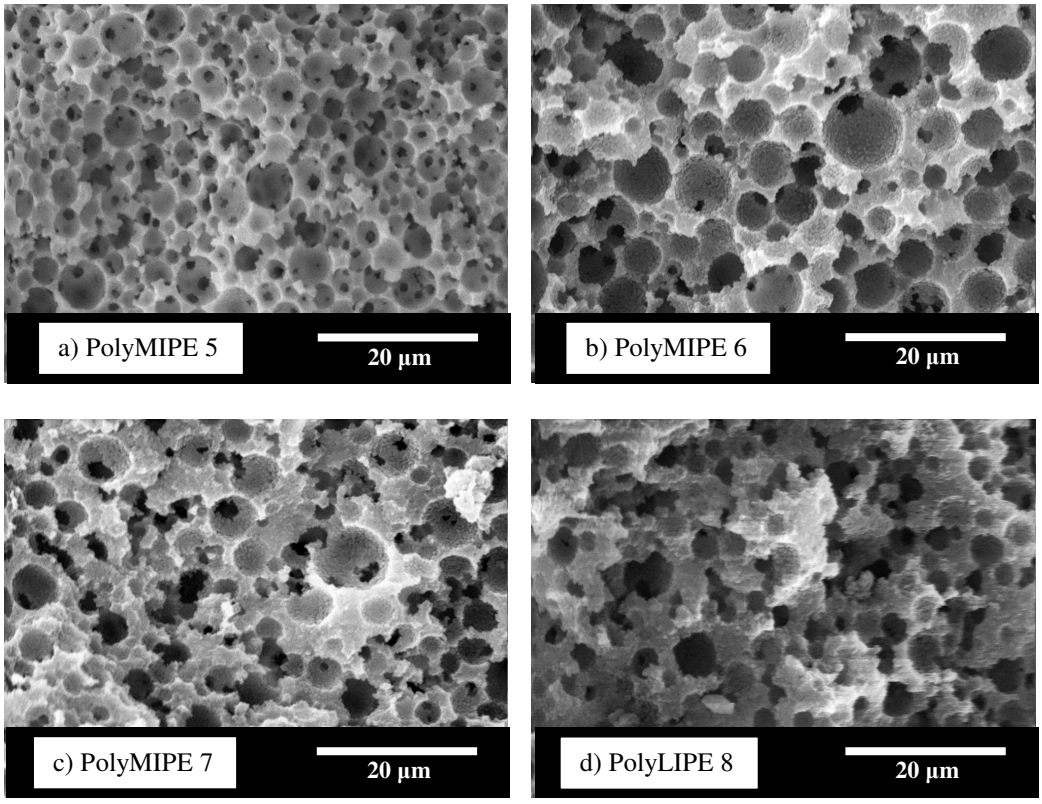


Figure 6-3a to d: SEM images of polyMIPEs to polyLIPEs 5 to 8

Figures 6-3a – d show SEM images of the Set 2 samples. The average pore diameters and pore throat diameters determined using SEM image analysis are summarised in Table 6-2. Although polyMIPEs **4** and **5** were both synthesised from emulsion templates having an internal phase volume of 60% their average pore diameter does differ significantly. An average pore of polyMIPE **5** is approximately half the size of an average pore of polyMIPE **4**. The reduction in pore size is the result of the decrease droplet size of MIPE **5** compared to MIPE **4**, which is caused by the increased effectiveness of the surfactant mixture of Hypermer 2296 and Hypermer B246sf (MIPE **5**) to stabilise emulsions containing 60 vol.-% internal phase compared to Hypermer 2296 alone (MIPE **4**). A significant decrease of the number of interconnecting pore throats can be observed in the SEM images of polyMIPEs **6**

– **7** and polyLIPE **8**. The SEM images of polyMIPE **7** (Figure 6-3c) and more notably of polyLIPE **8** (Figure 6-3d), show the absence of a typical open porous structure; however pore throats can still be identified.

Young's modulus as function of the porosity of the macroporous polymers is shown in Figure 6-4. As expected, the Young's modulus increases with decreasing porosity and, therefore, with increasing foam density of the porous polymers. PolyLIPE **8** with the highest foam density had the highest compression modulus. It is worth noting that the Young's moduli of polyMIPE **4** and **5**, both having the same porosity, are identical within the errors. Although the structural differences between polyMIPE **4** and **5** do not influence the Young's modulus, the crush strength of polyMIPE **5** is significantly higher than that of polyMIPE **4** (Table 6-2); this is due to polyMIPE **5**'s dramatically reduced pore size. As expected, with decreasing porosity the crush strength also increases from polyHIPE **2** to polyLIPE **8** (Table 6-2).

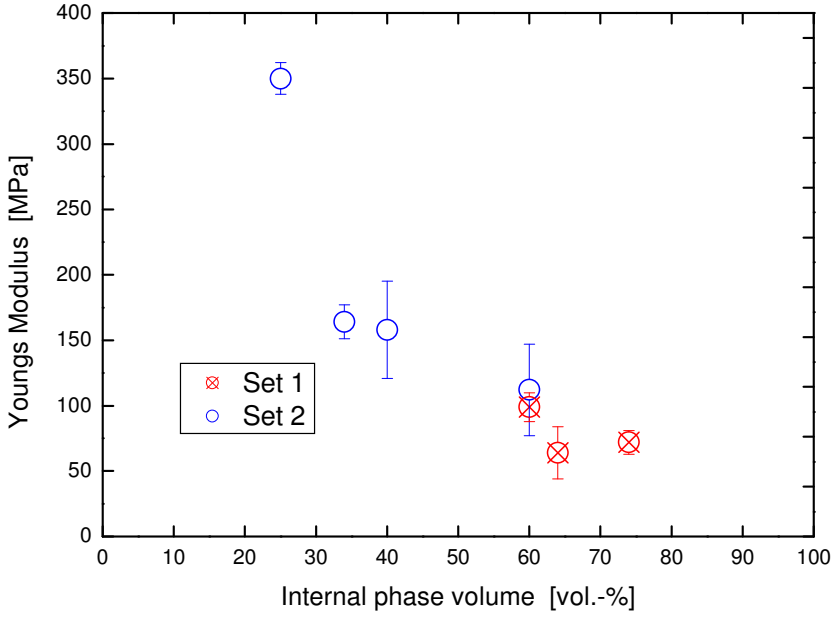


Figure 6-4: Mechanical test results - variation of the mechanical properties with internal phase volume of emulsions

Table 6-2: Summary of the measured properties of the polymer foams

	Sample	Porosity [%]	Foam Density [kg m^{-3}]	Young's Modulus [MPa]	Crush Strength [MPa]	Pore size [µm]	Pore throat diameter [µm]		Mercury Permeability [mD]	Gas Permeability [mD]
							From SEM analysis	From Hg (flow limiting)		
Set 1	1	89.1 ± 0.2	130 ± 4	-	-	4.7 ± 1.4	1.0 ± 0.5	-	-	-
	2	82.3 ± 0.8	223 ± 3	72 ± 9	3.6 ± 0.3	4.9 ± 1.9	1.5 ± 0.5	-	-	460 ± 41
	3	76.8 ± 0.2	270 ± 4	64 ± 20	4.7 ± 0.6	6.6 ± 1.2	1.8 ± 0.6	1.3 ± 0.1	70 ± 2.1	98.8 ± 2.4
	4	73.5 ± 0.1	317 ± 2	99 ± 11	5.4 ± 0.3	5.8 ± 1.1	1.7 ± 0.8	0.6 ± 0.1	24 ± 1.4	52.1 ± 1.0
Set 2	5	72.8 ± 0.1	314 ± 1	112 ± 35	8.4 ± 0.9	3.1 ± 1.2	0.9 ± 0.5	0.5 ± 0.1	27 ± 1.6	37.9 ± 1.7
	6	62.8 ± 0.1	421 ± 1	158 ± 37	13.0 ± 1.0	3.1 ± 1.2	1.7 ± 0.5	0.7 ± 0.1	15 ± 1.3	39.0 ± 0.6
	7	61.2 ± 0.1	446 ± 2	164 ± 13	14.0 ± 2.0	4.3 ± 1.7	1.4 ± 0.3	0.8 ± 0.1	9.0 ± 1.5	27.2 ± 0.3
	8	49.6 ± 0.1	565 ± 3	350 ± 12	19.0 ± 2.0	3.4 ± 1.3	1.1 ± 0.3	0.9 ± 0.1	7.0 ± 1.2	26.7 ± 0.3

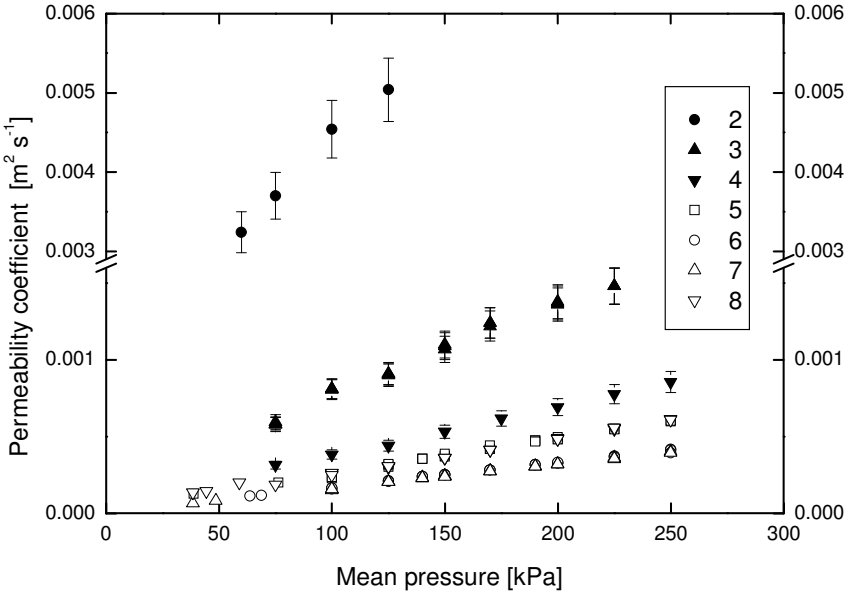


Figure 6-5: Gas permeability analysis: variation of the permeability coefficient with mean pressure for Set 1 and Set 2 samples

The gas permeability coefficient was calculated from the experimental measurements of the rate of pressure rise, (dp_2/dt) at various applied mean pressures p_m. However, it was not possible to determine the gas permeability of polyHIPE **1**; it failed in the apparatus due to its very low shear strength. Figure 6-5 shows the gas permeability coefficient as function of pressure. The viscous permeability values k were calculated from the slope of the individual curves and are summarised in Table 6-2. The permeability coefficients K as well as the slope of the permeability coefficient vs. pressure curve of polyHIPE **2** are much higher than those of all other samples. It is, therefore, no surprise that the viscous permeability of polyHIPE **2** is approximately one order of magnitude higher than those of the other samples. This indicates that polyHIPE **2** not only possesses the highest porosity

but also the highest degree of pore interconnectivity. In general, the viscous permeability shows a strong dependence on the porosity; the gas permeability decreases with decreasing porosity. However, there is sudden drop in gas permeability of polyMIPE **5** compared to polyMIPE **4**. Although the porosities of both samples are identical, it seems that the pores of polyMIPE **5** are less interconnected than those of polyMIPE **4**. Again surprisingly even polyLIPE **8**, whose emulsion template had the lowest internal phase volume and which, therefore, has the lowest porosity, was also permeable to gas. This proves that even a polyLIPE can possess sufficient numbers of pores, which are interconnected from one end of the sample to the other, and therefore gas and liquid flow is possible.

Mercury intrusion experiments were carried out on polyMIPEs **3** and **4** from Set 1 and all samples in Set 2. No flow of mercury through polyMIPE **3** was observed until the applied nitrogen pressure reached 0.3 MPa (Figure 6-6). This corresponds to a diameter of 1.28 μm and is indicative of the flow limiting (i.e. smallest) pore throat diameter of a series of interconnected pores with the largest pore throat diameters.

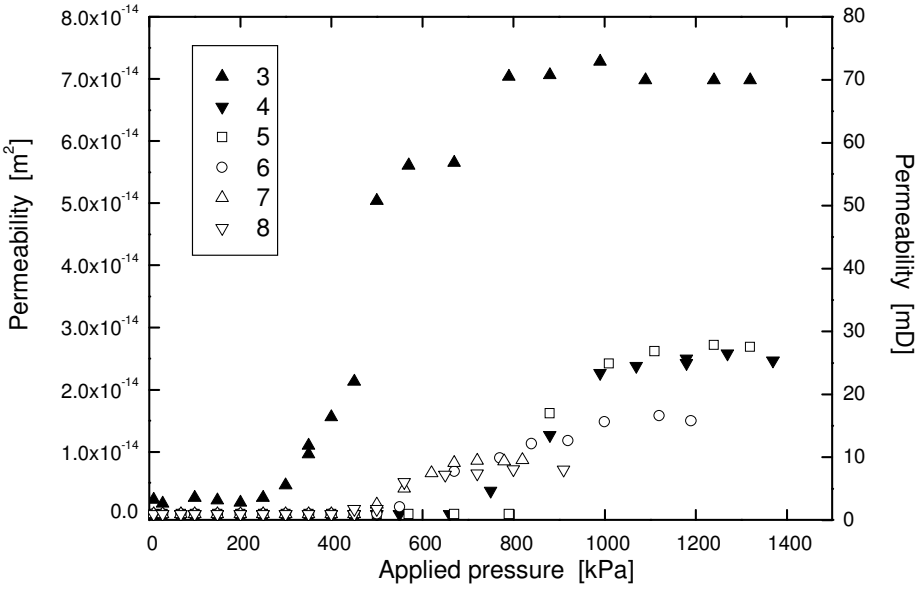


Figure 6-6: Mercury permeability distribution analysis of Samples 3to 8: permeability as a function of applied pressure for Set 1 and Set 2 samples

The flow limiting pore throat diameters are summarised in Table 6-2. Initially, the flow limiting pore throat diameter decreases with decreasing porosity; polyMIPE **5** possesses the smallest flow limiting pore throat diameter. However, from this point onwards the flow limiting pore throat diameter increases with decreasing porosity. This is surprising especially since the average pore throat diameters obtained from the analysis of the SEM images are identical within the error independent of the porosity of the porous polymers (Figure 6-7 and Table 6-2).

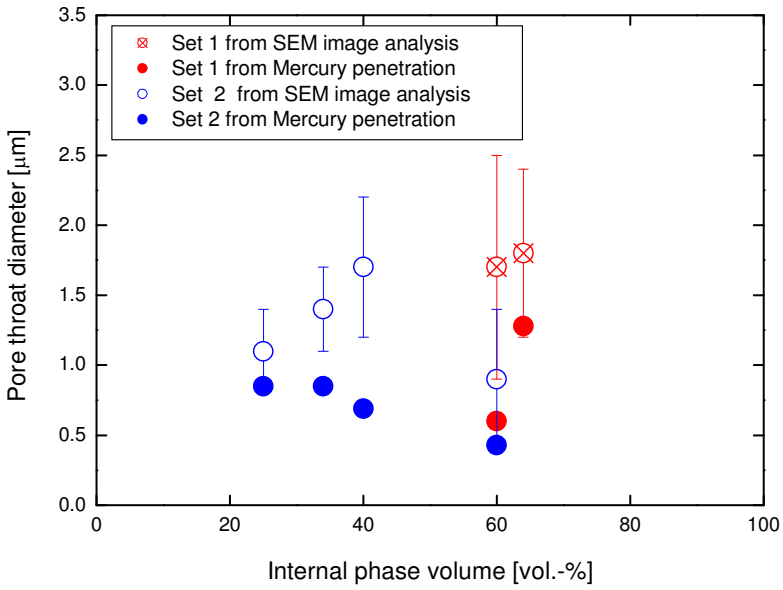


Figure 6-7: Comparison of the pore throat diameter determined from SEM analysis and mercury intrusion for the flow limiting pore throat diameter

The large scatter of the average pore throat diameters reflects the broad pore throat size distribution. This clearly shows that although the average pore throat size follows the before mentioned trend, the range of individual pore throat sizes and, therefore, the smallest pore throat size within a particular samples varies dramatically between the samples. It is worth noting that it is not, however, possible to identify a series of interconnecting pores from SEM images. Mercury intrusion measurements of the pore throat diameters are useful when flow properties are of interest since the throat diameters that control fluid flow are determined. The mercury permeability distributions are shown in Figure 6-6 and the average permeability of the macroporous polymers are summarised in Table 6-2. As expected, polyMIPE **3** has overall the highest mercury permeability and the permeability decreases

generally with decreasing porosity of the macroporous polymers. This indicates that although the pressure, which needs to be applied to generate flow through the sample, is determined by the flow limiting pore throat diameter, the overall permeability is strongly dependent on the porosity of the individual macroporous polymer. This is the reason why polyLIPE **8** and not polyMIPE **5**, which possesses the smallest flow limiting pore throat size, exhibits the lowest mercury permeability. However, it is surprising that polyLIPE **8**, which was made from an emulsion template containing as little as 25 vol.-% internal phase and whose pore structure is seemingly close celled (Figure 6-3d), is still permeable.

Mercury intrusion measurements of the pore throat diameters are useful when flow properties are of interest since the throat diameters that control fluid flow i.e. the smallest pore throats are determined.

The permeability distributions of polyMIPEs 3 – 7 and polyLIPE 8 have been graphically presented with the pore size distributions obtained from mercury porosimetry in to Figure 6-8 to Figure 6-13.

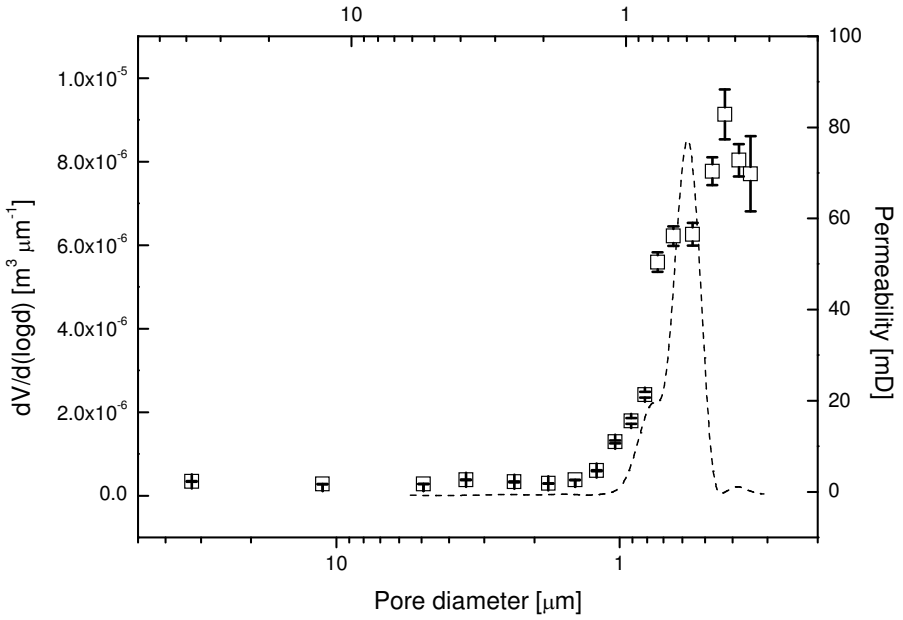


Figure 6-8: Permeability distribution (square points) and pore size distribution (dotted line) of polyMIPE 3

There are two significant peaks in the pore size distribution for polyMIPE 3 (Figure 6-8). The first corresponds to pore throats with a diameter of 0.9 µm, it is evident that the pore throats are interconnecting through the material since the penetration of these pore throats results in the initiation of fluid flow. The maximum or total permeability is reached when pore throats with a diameter of 0.5 µm are penetrated.

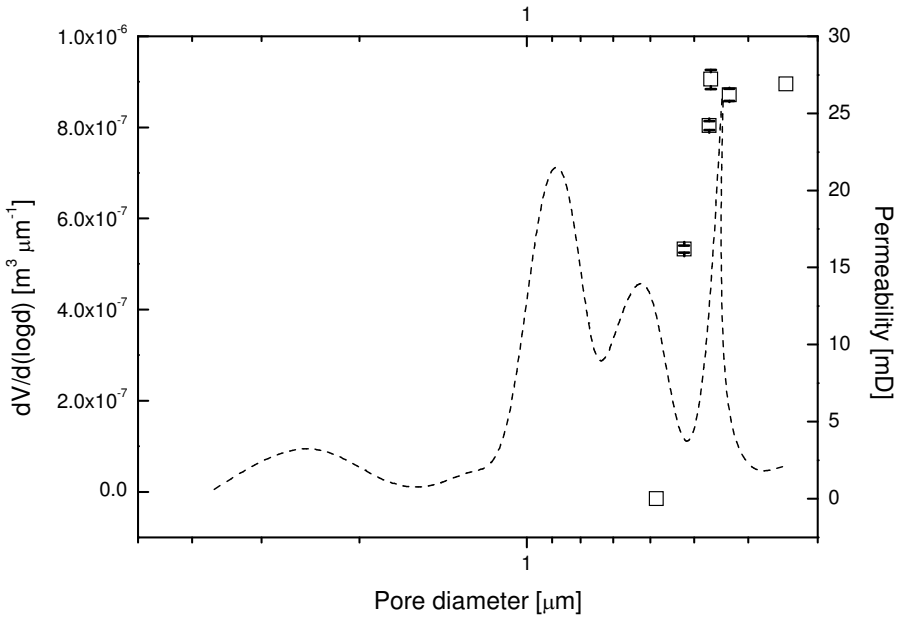


Figure 6-9: Permeability distribution (square points) and pore size distribution (dotted line) of polyMIPE 4

The pore size distribution of polyMIPE 4 is shown in Figure 6-9. The small peak at 3 µm could correspond an initial filling of the outer pores of the sample which are in contact with mercury. The second peak, corresponding to a pore throat diameter of 0.9 µm is indicative of a volume of mercury that is pushed through pore throats of this diameter into neighbouring pores. No flow occurs at this point showing that the pores are not completely interconnected. The flow limiting pore throat diameter is 0.6 µm as at this diameter, the onset of fluid flow is observed. The sample is fully interconnected when the maximum (total) permeability is reached after mercury penetrates pore throats of diameter 0.4.

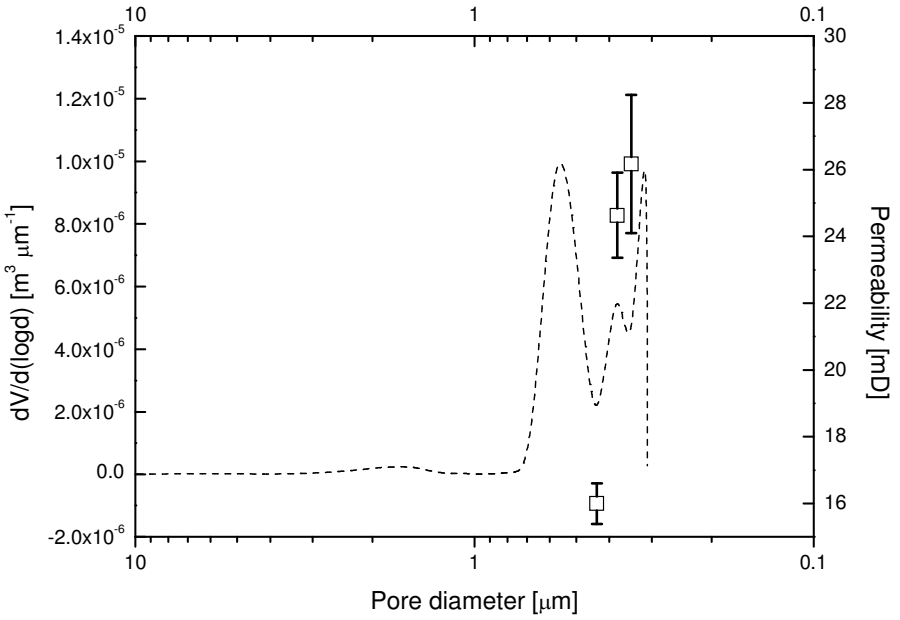


Figure 6-10: Permeability distribution (square points) and pore size distribution (dotted line) of polyMIPE 5

Figure 6-10 shows the pore size distribution of polyMIPE 5.The first peak, corresponding to a pore throat diameter of 0.6 µm shows that interconnections are formed through pores The initiation of fluid flow occurs when mercury is pushed through pore throats with a diameter of 0.3 µm and the total permeability is reached when mercury penetrates pores of 0.2 µm diameter.

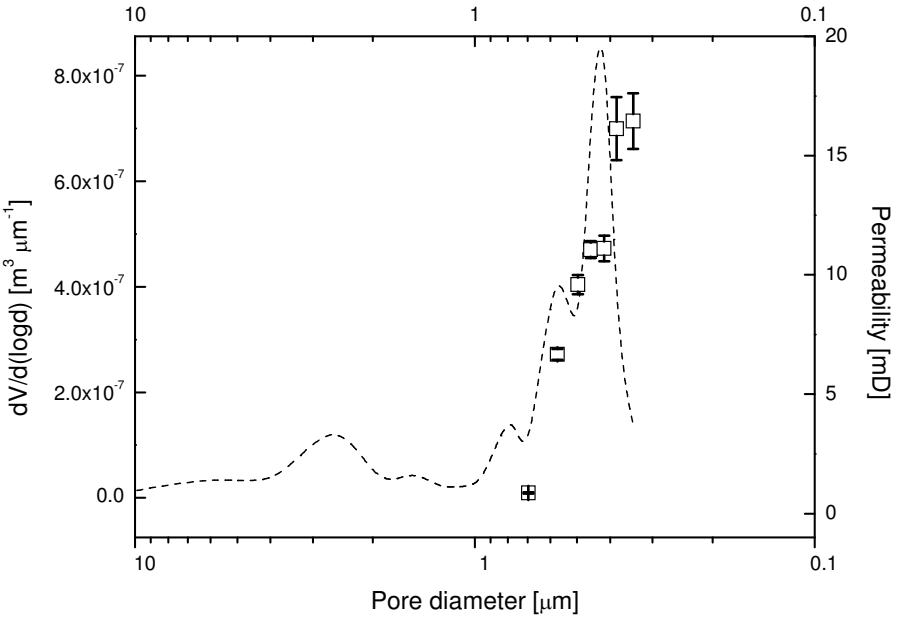


Figure 6-11: Permeability distribution (square points) and pore size distribution (dotted line) of polyMIPE 6

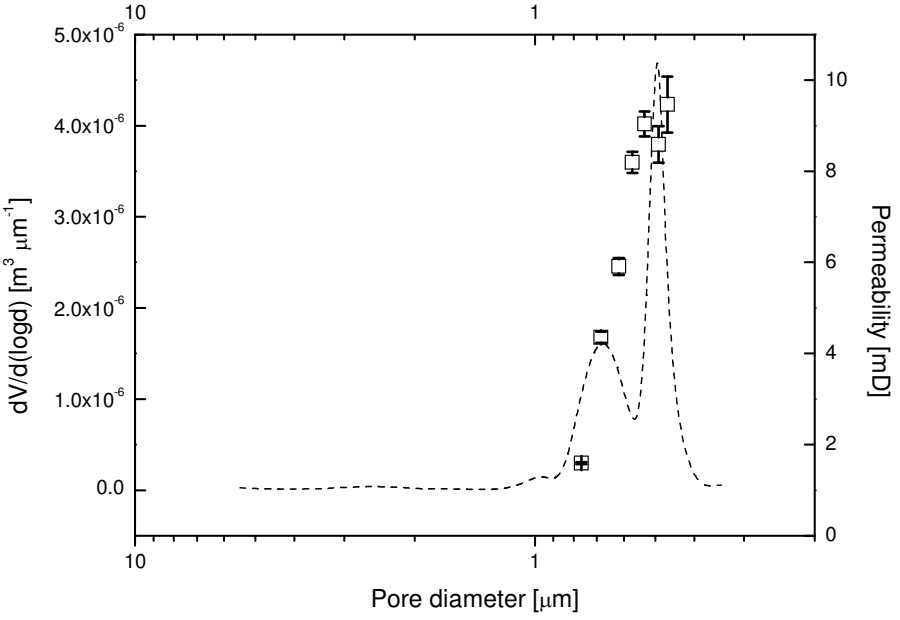


Figure 6-12: Permeability distribution (square points) and pore size distribution (dotted line) of polyMIPE 7

The pore size distribution of polyMIPE 6 (Figure 6-11) shows that initial fluid flow occurs through pore throats with a diameter of 0.8 µm. When pore throats of 0.5 µm are penetrated, more interconnected pores are filled and the total permeability is reached when the sample is fully connected through pore throats with a diameter of 0.35 µm. Figure 6-12 shows that pore throats of 0.7 µm diameter are interconnected and penetration of the these pores throats results in the initiation of fluid flow for polyMIPE 7. The total permeability is reached when pore throats of 0.5 µm diameter are penetrated.

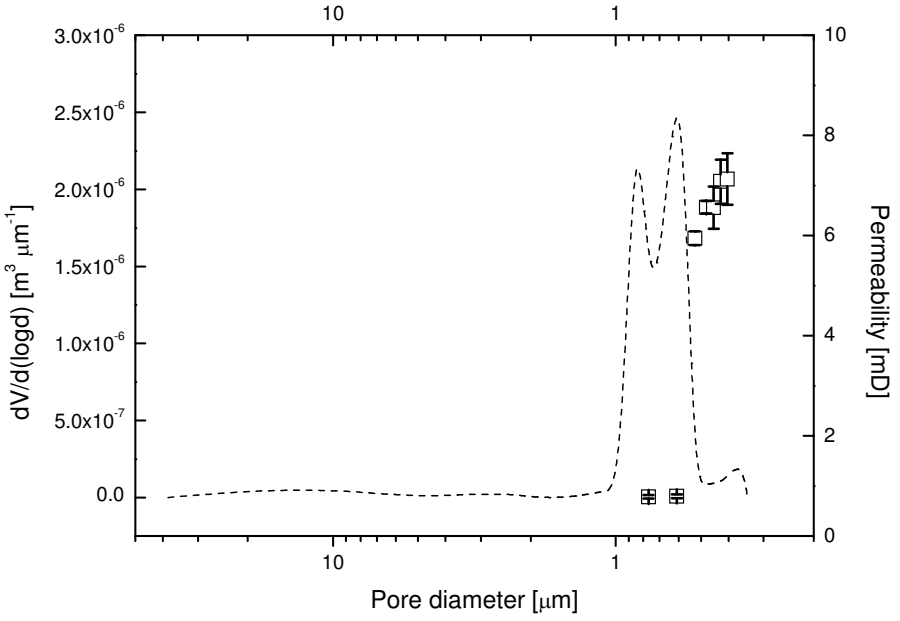


Figure 6-13: Permeability distribution (square points) and pore size distribution (dotted line) of polyLIPE 8

The pore size distribution of polyLIPE 8 in Figure 6-13 shows two significant peaks at 0.8 and 0.6 µm. Mercury flow is initiated and reaches the total permeability when pore throats of 0.6 µm are penetrated.

The gas and mercury permeability measurements showed that as the internal phase volume of the emulsion template was reduced, the permeability of the resultant polymer foam was also reduced. However, surprisingly, even polymer foams produced from a low internal phase emulsion template (25 vol.-%) were permeable with a gas permeability of 26.7 ± 0.3 mD indicating that contrary to popular belief, polyLIPEs are in fact also open porous polymer foams. This investigation shows evidence that reduction of the internal phase level of the emulsion templates from HIPEs to MIPEs (medium internal phase emulsions) and LIPEs (low internal phase emulsions) can still be used to form an interconnected porous structure as long as the droplets are in contact with each other (Cameron *et al.*, 1996, Menner *et al.*, 2006, Menner & Bismarck, 2006 and Normatov & Silverstein, 2007).

6.5 Summary of the integrated methods and their application to porous polymer foams

Two sets of polymer foams were prepared by the polymerisation of emulsion templates. The emulsion templates for 'Set 1' foams were stabilised using the surfactant Hypermer 2296 and samples were prepared with internal phase volumes ranging from 84 vol.-% to 60 vol.-%. Emulsions with internal volume fractions below 60 vol.-%, which acted as templates for the polymer foams of 'Set 2', could only be stabilised using a mixture of the surfactants Hypermer 2296 and B246sf. Set 2 polymer foams were prepared by the polymerisation of emulsion templates with internal phase volumes ranging from 60 vol.-% to 25 vol.-%. As the internal phase volume of the templates was reduced, the resultant polymer foams still maintained an open porous structure with interconnecting pores throats, although it was

noted that the frequency of the pore throats interconnecting pores decreased. As expected, the mechanical properties were improved as the foam density was increased and the polyLIPE sample produced from a 25 vol.-% internal phase emulsion had the highest Young's modulus of 350 MPa and crush strength of 19 MPa. Analysis of SEM images showed little variation in the pore throat diameters, but the results were not consistent with measurements taken using mercury intrusion. Further flow measurements using gas in a pressure rise technique show that the permeability of the polymer foams decreases as the internal phase volume of the emulsion templates is decreased. This is consistent with the measurements of permeability using mercury where the 25 vol.-% foam was found to have a permeability of 7.0 ± 1.2 mD. The combination of the pore size distribution with the permeability distribution shows the sizes of the pore throats that interconnected the porous samples as well as the flow limiting pore throat diameter. The results of this study have shown that it is possible to produce open porous polymer foams from emulsion templates with a reduced internal phase volume down to 25 vol.-%. The resultant polymer foams are also permeable to both nitrogen and mercury.

CHAPTER 7

CONCLUSIONS AND FURTHER WORK

In this, the final Chapter of the thesis, concluding remarks regarding the work carried out in this investigation are presented. This Chapter includes a summary of the most relevant findings and suggestions of useful further work.

This thesis describes an investigation into methods for characterisation of porous solids. Attention has been focused on properties of porous solids that are relevant to the flow of fluids through the material, namely prominently porosity, permeability, diffusivity and conductivity. To study these properties, two new **integrated methods** were developed as characterisation tools. These integrated methods consisted of a single pieces of apparatus which encompassed several characterisation techniques and can be used to measure multiple properties of porous materials.

7.1 Conclusions

7.1.1 Development of the combination methods

With a view to providing both academia and industry with the relevant tools for the measurement of flow properties, two laboratory scale pieces of apparatus were designed:

1. Integrated gas permeability and diffusivity.
2. Integrated mercury porosimetry, permeability and electrical conductivity.

Both pieces of apparatus were designed to allow for the measurement of multiple properties of porous materials, one using gas flow measurements and one using a mercury impregnation technique. The results obtained from each piece of apparatus were used to determine structural and flow properties of porous solids.

7.1.2 Integrated gas permeability and diffusivity apparatus

The apparatus was designed and constructed for the measurement of gas permeability using a gas pressure rise technique and gas diffusivity using oxygen-in-nitrogen diffusion. The following conclusions can be drawn from the investigations carried out:

- Reproducibility investigations carried out on both the prototype gas permeability apparatus and the integrated apparatus confirm that the permeability and diffusivity results obtained are reproducible.
- Measurements of the viscous permeability and slip flow of a range of Berea sandstone samples showed that the apparatus was capable of measuring permeabilities as low as 0.24 mD (2.4×10^{-16} m^2) and as high as 1050 mD (1.05×10^{-12} m^2).
- As the mean pressure decreases, it is more and more important to take account of slip on the flow. This is done by introducing a slip flow coefficient, K_0. At very low pressures, the transport mechanism changes gradually to a diffusive one with free

molecule (Knudsen) diffusion becoming the operative mechanism at the lowest pressure.

- Steady state diffusion of oxygen in nitrogen in the pores of the samples was measured under constant pressure conditions. By coupling the results of such measurements with those obtained for transient diffusion, it was possible to deduce the effective pore length (and hence the ratio of the effective pore length to sample length – the tortuosity) and also the effective porosity. The tortuosity values measured for Berea sandstone are in a similar range to those measured in the literature.

7.1.3 Integrated mercury porosity, permeability and electrical conductivity apparatus

A second method for the characterisation of porous solids was developed using a mercury impregnation technique. The apparatus was designed and constructed for the measurement of porosimetry, permeability and electrical conductivity. The following conclusions can be made from the investigations carried out:

- The total pore volume of the samples could be determined and the effective porosity calculated.
- The volume of pores of specific pore diameters were quantified by measuring the volume of mercury that penetrates the sample at specific applied pressures ("porosimerty").
- The pore size distribution can be determined from the porosimetry results.

- The variation of mercury permeability with pore size penetrated (i.e. with applied pressure) gives a useful indication of the contributions of the various pores to the overall permeability.
- At the highest penetration pressure, the mercury permeability reached a value similar to the measured viscous gas permeability.
- Measurement of the electrical conductivity of mercury in the pores of the samples gives information analogous, for diffusion, to the measurements of mercury permeability for permeability. Physically, the conduction process is similar in nature to the diffusion process. Thus, the ratio of the diffusion coefficient in the medium to its value in free space would be expected to be similar to the ratio of the conductivity of a medium saturated with a conducting liquid to the conductivity of the liquid itself. The present results confirm that this is the case for mercury conductivity for the situation when the pores are filled with mercury. More importantly, the variation of the conductivity ratio with pressure (i.e. pore size penetrated) gives an indication of the contribution of pores of various sizes to the diffusion process.

7.1.4 General conclusions

- Though the effective porosity deduced from diffusion measurements was usually less (as would be expected) than the porosity measured using the helium pycnometry method, there were a few cases where the opposite was true. This leads to doubts about the accuracy of the helium pycnometry technique.

- The permeability values obtained using gas permeability, mercury permeability and prediction from image analysis were in good agreement.
- The tortuosity values obtained from steady state and transient diffusion measurements were consistent with those values reported for Berea sandstone in the literature.
- The investigation of the permeability of porous polymer foams shows that the use of the integrated techniques can be extended to porous materials other than reservoir rocks.

7.1.5 Limitations of the current study

Finally, a number of limitations need to be considered in extending the scope of the tests for other types of porous solids:

- The dimensions of the sample cells in both of the integrated apparatus are such that the sample cores are required to be of a specific diameter and length which places limitations on the types of samples that can be tested. The sample manufacture and mounting methodology should be reconsidered to address these limitations.
- It is not possible to test samples that are not easily machinable due to the rigorous process used for sealing the samples in epoxy resin. Again, better mounting and sealing methods seem desirable.
- There are pressure limitations on the integrated mercury apparatus therefore very small pores (less than about 0.2 μm) may not be filled with mercury resulting in inaccuracies in the measurements of the total pore volume and permeability.

7.2 Recommendations for further work

The following actions are recommended for future research and improvement of the experimental methods.

Integrated gas permeability and diffusivity:

- Investigation of the effect of a pressure gradient on the diffusion coefficient using the gas diffusivity set-up is recommended. This is an important practical case and would be relatively straightforward to study using the existing apparatus. Similar measurements have been made in the case of porous graphite by Hewitt and Sharratt (1963a).
- Further study into turbulence is recommended and the development of a three term equation to include the viscous permeability, the effect of slip and turbulent effects should be addressed.
- It may be interesting to operate the integrated gaseous transport apparatus with a wider range of gases, and in particular, in the case of diffusion, with gases having large differences in molecular weight where net drift effects become more significant.
- Automation for the integrated gas apparatus. The system could be upgraded to an automatic piece of apparatus where the valves are programmed to open and close as required. It could also be possible to measure the rate of pressure rise in the vessel automatically and increase the inlet pressure on the high pressure side. This would markedly improve the rapidity of operation and would eliminate the experimental error due to measurement of the rate of pressure rise.

Integrated mercury porosimetry, permeability and electrical conductivity:

- Improvement of cell and apparatus design is recommended for further study of mercury impregnation. This would include the widening of all connecting tubes from ¼ inch internal diameter to at least 1 inch. This would aid evacuation and help maintain low pressure in the system. There is also scope for the development of a quick release sample cell and a more secure method of removing the mercury saturated sample from the system when experiments are complete. The sample cell could also include ports for the electrodes.
- X-ray microtomography investigation of the samples could also be included for visual characterisation of the pore structure in general and the effective pore lengths in particular.

REFERENCE LIST

Adzumi, H. (1937) On the flow of gases through a porous wall. *Bulletin of the Chemical Society of Japan,* 12 (6), 304.

Ali, L., Garrouch, A. & Qasem, F. (2001) Using diffusion and electrical measurements to assess tortuosity of porous media. *Industrial and Engineering Chemistry Research,* 40, 4363-6369.

Al-Quraishi, A. & Khairy, M. (2005) Pore pressure versus confining pressure and their effect on oil-water relative permeability curves. *Journal of Petroleum Science and Engineering,* 48, 120-126.

Altman, S. J., Peplinski, W. J. & Rivers, M. L. (2005) Evaluation of synchrotron X-ray computerized microtomography for the visualization of transport processes in low-porosity materials. *Journal of Contaminant Hydrology,* 78 (3), 167.

Amthor, J. E. & Kopaska-Merkel, D. C. (1988) Very high pressure mercury porosimetry as a tool in reservoir characterisation. *Carbonates and Evaporites,* 3 (1), 53.

Archie, G. E. (1942) The electrical resistivity log as an aid in determining some reservoir characteristics. *Transactions of AIME,* 146, 54.

Auzerais, F. M., Dunsmuir, J., Ferreol, B. B., Martys, N., Olson, J., Ramakrishnan, T. S., Rothman, D. H. & Schwartz, L. M. (1996) Transport in sandstone: a study based on three dimensional microtomography. *Geophys. Res. Lett.,* 23 (7), 705-708.

Baas, J. H., Hailwood, E. A., McCaffrey, W. D., Kay, M. & Jones, R. (2007) Directional petrological characterisation of deep-marine sandstones using grain fabric and permeability anisotropy: Methodologies, theory, application and suggestions for integration. *Earth-Science Reviews,* 82 (1-2), 101.

Baraka-Lokmane, S. (2002) Hydraulic versus pneumatic measurements of fractured sandstone permeability. *Journal of Petroleum Science and Engineering,* 36, 183.

Baraka-Lokmane, S., Main, I. G., Ngwenya, B. T. & Elphick, S. C. (2007) Application of complementary methods for more robust characterization of sandstone cores. *Marine and Petroleum Geology,* In Press, Corrected Proof,.

Bentz, D. P., Quenard, D. A., Kunzel, H. M., Baruchel, J., Peyrin, F., Martys, N. S. & Garboczi, E. J. (2000) Microstructure and transport properties of porous building materials. II: Three-dimensional X-ray tomographic studies. *Materials and Structures,* 33 (3), 147.

Berkowitz, B. (2002) Characterizing flow and transport in fractured geological media: A review. *Advances in Water Resources,* 25 (8-12), 861.

Biloe, S. & Mauran, S. (2003) Gas flow through highly porous graphite matrices. *Carbon,* 41, 525.

Bokhoven, C. & Hoogschagen, J. (1952) Diffusion in porous catalysts. *Journal of Chemical Physics,* 21 (1), 159-160.

Botset, H. G., Muskat, M., Reed, D. W. & Wyckoff, R. D. (1933) The measurement of the permeability of porous media for homogeneous fluids. *Review of Scientific Instruments,* 4, 394-405.

Brakel, J. V., Modry, S. & Svata, M. (1981) Mercury porosimetry: State of the art. *Powder Technology,* 29, 1.

Cameron, N. R. (2005) High internal phase emulsion templating as a route to well-defined porous polymers. *Polymer,* 46 (5), 1439.

Cameron, N. R., Sherrington, D. C., Albiston, L. & Gregory, D. P. (1996) Study of the formation of the open cellular morphology of poly(styrene/divinylbenzene) polyHIPE materials by cryo-SEM. *Colloid Polymer Science,* 274 (6), 592.

Carman, P. C. (1956) Flow of Gases Through Porous Media. In: Belfast, Butterworths Scientific Publications, pp. 69.

Carman, P. C. (1953) Fluid Flow Through a Granular Bed. *Transactions of the Institution of Chemical Engineers and the Chemical Engineer,* 15, 150.

Caruso, L., Simmons, G. & Wilkens, R. (1985) The physical properties of a set of sandstones—Part I. The samples. *International Journal of Rock Mechanics and Mining Science & Geomechanics Abstracts,* 22 (6), 381-392.

Chatzis, I., Ioannidis, M. A. & Payatakes, A. C. (1991) A mercury porosimeter for investigating capillary phenomena and microdisplacement mechanisms in capillary networks. *Journal of Colloid and Interface Science,* 143 (1), 22.

Christenson, E. M., Soofi, W., Holm, J. L., Cameron, N. R. & Mikos, A. G. (2007) Biodegradable fumarate-based polyHIPEs as tissue engineering scaffolds. *Biomacromolecules,* 8 (12), 3806.

Coker, D. A. & Torquato, S. (1996) Morphology and physical properties of Fontainebleau sandstone via a tomographic analysis. *Journal of Geophysical Research,* 101, 17497-17506.

Coles, M. E., Hazlett, R. D., Muegge, E. L., Jones, K. W., Andrews, B., Dowd, B., Siddons, P., Peskin, A., Spanne, P. & Soll, W. (1998) Developments in synchrotron X-ray microtomography with applications to flow in porous media. *SPE Reservoir Evaluation and Engineering,* 1 (4), 288-296.

Collins, R. E. (1961) *Flow of Fluids Through Porous Materials.* USA, Reinhold Publishing Corporation.

Cosentino, I. C. & Oliveira, R. (2000) Physical characterization of materials (BET, Hg porosimetry and thermal analysis). *Materials Science and Technology Center - IPEN.*

Dees, P. J., Polderman, J. & Tjan, T. G. (1980) Determination of pore diameter by permeability measurements. *Powder Technology,* 27.

Despois, J-F & Mortensen, A. (2005) Permeability of open-pore microcellular materials. *Acta Materialia,* 53, 1381.

Dietrich, P., Helmig, R., Sauter, M., Holtz, H., Kongeter, J., Teutsch, G. (2005) *Flow and Transport in Fractured Porous Media.* Berlin, Spinger.

Dullien, F. A. L. (1979) *Porous Media Fluid Transport and Pore Structure.* London, Academic Press.

Durlofsky, L. J. & Gerritsen, M. G. (2005) Modelling fluid flow in oil reservoirs. *Annual Review of Fluid Mechanics,* 37, 211-235.

Edler, K. J. & Rigby, S. P. (2002) The influence of mercury contact angle, surface tension and retraction mechanisms on the interpretation of mercury porosimetry data. *Journal of Colloid and Interface Science,* 250, 175.

Evans, R. B. & Watson, G. M. (1961) Gaseous diffusion in porous media at uniform pressure. *Journal of Chemical Physics,* 35 (6), 2076-2083.

Ferguson, L. & Schumacher, E. (1927) A convenient apparatus for measuring the diffusion of gases and vapors through membranes. *Journal of the American Chemistry Society,* 49 (2), 427.

Garboczi, E. J. (1991) Mercury Porosimetry and Effective Networks for Permeability Calculations in Porous Materials. *Powder Technology,* 67 (121).

Garcia, Y., Breena, A., Burugapallia, K., Dockeryc, P. & Pandita, A. (2007) Stereological methods to assess tissue response for tissue-engineered scaffolds. *Biomaterials,* 28 (2), 175-186.

Grosse, M-T, Birot, M., Lamotte, M. & Deleuze, H. (2007) Preparation of microcellular polysiloxane monoliths. *Journal of Polymer Science: Part A,* 46, 21.

Hawtin, P., Hewitt, G.F. and Roberts, J. (1967) Flow of gases in porous solids. Nature Vol. 215, No. 5108, pp. 1415-1416.

Hatfield, M. R. (1939) Fluid flow through porous carbon. *Industrial and Engineering Chemistry,* 31 (11), 1419.

Heaviside, J., Black, C.J.J. and Berry, J.F. (1983) Fundamentals of Relative Permeability: Experimental and Theoretical Considerations. *SPE Annual Technical Conference and Exhibition, San Francisco, California*, 12173-MS.

Heijs, A. W. J. & Lowe, C. P. (1995) Numerical evaluation of the permeability and the Kozeny constant for two types of porous media. *Physical Review E,* 51 (5), 51.

Hewitt, G. F. (1967) Further Techniques for the Study of Pore Structure by Liquid-Metal Penetration. In: Bond. R.L. (ed.) *Porous Carbon Solids.* Academic Press, pp. 203.

Hewitt, G.F. (1960) Some studies of the behavior of non wetting liquid metals in porous media with particular reference to graphite. UKAEA Report No. AERE R3283, March, 1960.

Hewitt, G. F. (1961) Physical factors governing the containment of zinc in graphite. UKAEA Report No. AERE M762, January 1961.

Hewitt, G.F. (1961) Some measurements of the gas permeability of graphite. UKAEA Report No. AERE M851,March 1961.

Hewitt, G.F. (1962) Physical factors governing the containment of zinc in graphite. *The Industrial Chemist*, pp. 609-614, December 1962.

Hewitt, G. F. (1964) Gaseous mass transfer within graphite. UKAEA Report No. AERE R4647, May 1964

Hewitt, G.F. (1966) Gaseous mass transport within graphite. Chapter II of Physics and Chemistry of Carbon, edited by P.L. Walker, published by Marcel Dekker

Hewitt, G.F. (1967) Approximate equations for the diffusion and flow of gases in porous media. UKAEA Report No. AERE R5492, August, 1967.

Hewitt, G.F. (1967) Further techniques for the study of pore structure by liquid-metal penetration. In “Porous carbon solids” (R.L. Bond, ed) chapter 5, pp. 203-224 (1967).

Hewitt, G.F. and Lacey, P.M.C. (1963) Pore diffusion and flow studies with nuclear graphite. UKAEA Report No. AERE R4366, June 1963

Hewitt, G. F. and Morgan, J. R. (1961) The diffusion of oxygen in nitrogen in the pores of graphite: Systematic investigation of a cross section of a block of pile A graphite. UKAEA Report No. AERE R3814, September , 1961

Hewitt, G.F. and Morgan, J.R. (1964) The diffusion of oxygen in nitrogen in the pores of graphite. Progress in Applied Materials Research - 5, Heywood & Co. Ltd., London, pp. 167-204.

Hewitt, G.F., Moore, M.J.C. and Sharratt, E.W. (1969) The diffusion of oxygen in nitrogen in the pores of graphite. UKAEA Report No. AERE R4536, February, 1969.

Hewitt, G.F., Moore, M.J.C. and Sharratt, E.W. (1970) The diffusion of oxygen in nitrogen in the pores of graphite. The effect of oxidation on diffusivity and permeability. Carbon, Vol. 8, pp. 21-282.

Hewitt, G.F. and Sharratt, E.W. (1962) Bismuth impregnation studies of virgin and oxidized nuclear grade graphite. UKAEA Report No. AERE R3993, June 1962.

Hewitt, G. F. and Sharratt, E. W. (1962) The diffusion of oxygen in nitrogen in the pores of graphite. Preliminary results for the effect of oxidation on diffusivity. UKAEA Report No. AERE M1080, October 1962.

Hewitt, G.F. and Sharratt, E.W. (1963a) The effect of back pressure on the counter diffusion of gases in graphite. UKAEA Report No. AERE-M1081, March 1963

Hewitt, G. F. (1960) Some Studies of the Behaviour of Non-Wetting Liquid Metals in Porous Media with Particular Reference to Graphite. *UK Atomic Energy Authority*.

Hewitt, G. F. & Lacey, P. M. C. (1963) Pore diffusion and flow studies with nuclear graphite. *UK Atomic Energy Authority*.

Hewitt, G. F. & Sharratt, E. W. (1963) Gaseous diffusion in porous media with particular reference to graphite. *Nature,* 198 (4884), 952-957.

Hewitt, G.F. and Sharratt, E.W. (1964) The effect of back pressure on the counter diffusion of gases in graphite. J. Nucl. Materials., Vol. 13, pp. 197-206.

Ishizaki, K., Komareneni, S. & Nanko, M. (1998) *Porous Materials: Process Technology and Applications.* UK, Kluwer.

Kallel, A. (2004) Gas permeability and tortuosity for packed layers of processed municipal solid wastes and incinerator residue. *Waste Management Research,* 22 (3), 186.

Katz, A. J. & Thompson, A. H. (1986) Quantitative prediction of permeability in porous rock. *Physical Review B,* 34 (11), 8179.

Klinkenberg, L. J. (1951) *Bull. Geol. Soc. Amer.,* 62, 559.

Kloubek, J. (1981) A new method for the investigation of porous structures using mercury porosimetry. *Powder Technology,* 29, 89.

Koplik, J., Lin, C. & Vermette, M. (1984) Conductivity and permeability from microgeometry. *Journal of Applied Physics,* 56 (11), 3127-3131.

Krajnc, P., Leber, N., Brown, J. F. & Cameron, N. R. (2006) Hydroxy-derivatised emulsion templated porous polymers (PolyHIPEs): Versatile supports for solid and solution phase organic synthesis. *Reactive and Functional Polymers,* 66, 81-91.

Krajnc, P., Štefanec, D., Brown, J. F. & Cameron, N. R. (2005) Arylacrylate based high internal phase emulsions as precursors for reactive monolithic polymer supports. *Journal of Polymer Science: Part A,* 43, 296-303.

Lafhaj, Z., Loosvelt, H. & Skoczylas, F. (2002) Experimental study of gas and liquid permeability of a mortar. *Cement and Concrete Research,* 32, 1363.

Le Coq, L. (2008) Influence on permeability of the structural parameters of heterogeneous porous media. *Environmental Technology*. 29 (2), 141-9.

Le Doussal, P. (1989) Permeability versus conductivity for porous media with wide distribution of pore sizes. *Physical Review B,* 39 (7), 4816-4819.

Lock, P. A., Jing, X., Zimmerman, R. W. & Schlueter, E. M. (2002) Predicting the permeability of sandstone from image analysis of pore structure. *Journal of Applied Physics,* 92 (10), 6311-6319.

Menner, A. & Bismarck, A. (2006) New evidence for the mechanism of the pore formation in polymerising High Internal Phase Emulsions or why polyHIPEs have an interconnected pore network structure. *Macromolecular Symposia,* 242, 19.

Menner, A., Powell, R. & Bismarck, A. (2006) Open porous polymer foams via inverse emulsion polymerization: Should the definition of high internal phase (ratio) emulsions be extended? *Macromolecules,* 39 (6), 2034.

Miguel, A. F. & Serrenho, A. (2007) On the experimental evaluation of permeability in porous media using a gas flow method. *Journal of Physics D Applied Physics,* 40, 6824.

Millikan, R. A. (1923) Coefficients of slip in gases and the law of reflection of molecules from surfaces of solids and liquids. *Phys. Rev.* 21, 217

Muskat, M. (1937) *The Flow of Homogeneous Fluids Through Porous Media.* 1st edition. USA, McGraw-Hill.

Normatov, J. & Silverstein, M. S. (2007) Porous interpenetrating network hybrids synthesized within high internal phase emulsions. *Polymer,* 48 (22), 6648.

Okabe, H. & Blunt, M. J. (2004) Prediction of permeability for porous media reconstructed using multiple-point statistics. *Physical Review E,* 70 (6), 066135.

Oak, M. J. (1990), Three-phase relative permeability of water-wet Berea, Pap. SPE 20183, *Soc. of Pet. Eng*., Richardson, Texas.

Ottens, M., Leene, G., Beenackers, A. A. C. M., Cameron, N. & Sherrington, D. C. (2000) PolyHIPE: A new polymeric support for heterogeneous catalytic reactions. *Industrial and Engineering Chemistry Research,* 39, 259-266.

Pape, H., Clauser, C. & Iffland, J. (2000) Variation of permeability with porosity in sandstone diagenesis interpreted with a fractal pore space model. *Pure and Applied Geophysics,* 157 (4), 603.

Radisic, M., Deen, W., Langer, R. & Vunjak-Novakovic, G. (2005) Mathematical model of oxygen distribution in engineered cardiac tissue with parallel channel array perfused with culture medium containing oxygen carriers. *American Journal of Physiology. Heart and Circulatory Physiology,* 288 (3), H1278.

Raharjo, R. D., Freeman, B. D., Paul, D. R., Sarti, G. C. & Sanders, E. S. (2007) Pure and mixed gas CH_4 and n-C_4H_{10} permeability and diffusivity in poly(dimethlysiloxane). *Journal of Membrane Science,* 306, 75.

Ribia, W., Sendenb, T. J., Sakellarioub, A., Limayec, A. & Zhang, S. (2008) Imaging honey bee brain anatomy with micro-X-ray-computed tomography. *Journal of Neuroscience Methods,* 171 (1), 93.

Satterfield, C. N. & Cadle, P. J. (1968) Diffusion in commercially manufactured pelleted catalysts. *Industrial and Engineering Chemistry Process Design and Development,* 7 (2), 256-260.

Scherer, George W., Valenza II, John J. & Simmons, Gregory. (2007) New methods to measure liquid permeability in porous materials. *Cement and Concrete Research,* 37 (3), 386-397.

Schwartza, L. M., Auzeraisa, F., Dunsmuirb, J., Martysc, N., Bentzc, D. P. & Torquatod, S. (1994) Transport and diffusion in three-dimensional composite media. *Physica A: Statistical and Theoretical Physics,* 207 (1-3), 28-36.

Siddiqui, S., Talabani, S., Saleh, S. T. & Islam, M. R. (2002) Foam flow in low-permeability Berea Sandstone cores: a laboratory investigation. *Journal of Petroleum Science and Engineering,* 36 (3-4), 133-148.

Silverstein, M. S., Tai, H. W., Sergienko, A., Lumelsky, Y. L. & Pavlovsky, S. (2005) PolyHIPE: IPNs, hybrids, nanoscale porosity, silica monoliths and ICP-based sensors. *Polymer,* 46 (17), 6682.

Sing, K.S.W. (2004) Characterisation of Porous Materials: Past, Present and Future. *Colloids and Surfaces A: Physiochemical and Engineering Aspects,* 241 (1-3), 3.

Smithwick, R. W. (1982) A General Analysis for Mercury Porosimetry. *Powder Technology,* 33, 201.

Solymar, M. & Fabriciu, I. L. (1999) Image analysis and estimation of porosity and permeability of Arnager Greensand, Upper Cretaceous, Denmark. *Physics and Chemistry of the Earth,* 24 (7), 587.

Subcommittee on Characterisation of Porous Solids. (1994) Recommendations for the characterisation of porous solids. *Pure and Applied Chemistry,* 66 (8), 1739.

Tiab, D. & Donaldson, E. C. (1996) *Petrophysics: theory and practice of measuring reservoir rock and fluid transport properties.* Houston, Gulf Publishing Co.

Valvatne, P. H. & Blunt, M. J. (2004), P Predictive pore-scale modeling of two-phase flow in mixed wet media *Water Resources Research*, 40, W07406..

Wakao, N. and Smith, J.M. (1962) Diffusion in catalyst pellets. *Chemical Engineering Sciences,* 17, 825-834.

Wakeman, R. J., Bhumgara, Z. G. & Akay, G. (1998) Ion exchange modules formed from polyhipe foam precursors. *The Chemical Engineering Journal and the Biochemical Engineering Journal,* 70 (2), 133.

Washburn, E. W. (1921) The dynamics of capillary flow. *The Physical Review,* 17, 273

Weisz, P. B. (1957) Diffusivity of porous particles I. Measurements and significance for internal reaction velocities. *Zeitschrift Fur Physikalische Chemie,* 11, 1-15.

Weisz, P. B. & Schwartz, A. B. (1962) Diffusivity of porous-oxide-gel-derived catalyst particles. *Journal of Catalysis,* 1, 399-406.

Wong, H. S., Buenfeld, N. R. & Head, M. K. (2006) Estimating transport properties of mortars using image analysis on backscattered electron images. *Cement and Concrete Research,* 36 (8), 1556-1566.

Wu, K. J., Van Dijke, M. I. J., Couples, G. D., Jiang, Z. Y., Ma, J. S., Sorbie, K. S., Crawford, J., Young, I. & Zhang, X. X. (2006) 3D stochastic modelling of heterogeneous porous media - Applications to reservoir rocks. *Transport in Porous Media,* 65 (3), 443.

Wyllie, M. R. J. & Spangler, M. B. (1952) Application of electrical resistivity measurements to problem of fluid flow in porous media. *Bulletin of the American Association of Petroleum Geologists,* 36 (2), 359-403.

Xu, P. & Yu, B. (2008) Developing a new form of permeability and Kozeny-Carman constant for homogeneous porous media by means of fractal geometry. *Advances in Water Resources,* 31 (1), 74.

Youngquist, G. R. (1970) *Diffusion and flow of gases in porous solids.* American Chemical Society, Washington, D.C.

Appendix I - Operating procedure for the prototype gas permeability apparatus

This procedure follows uses the terms and naming system as shown in Chapter 3.

Start Up

1) Ensure all valves are closed.
2) Place sample in holder and fasten lid to base with 4 screws (Use Allen key marked "GP").
3) Ensure vacuum pump and N_2 line are connected.
4) Turn on P_{in}, P1 and P2 pressure gauges (Press enter).
5) Open V2, V3 and V4.
6) Turn on vacuum pump to evacuate system.
7) Wait until P1 and P2 reads -1.0 bar.
8) Carefully turn on N_2 supply (clockwise open, regulator valve anticlockwise open).
9) Make sure $P_{in} < 10$ bar.
10) Close V2 and open V1.
11) Wait for $P_{in} = P_{1.}$
12) Note P1.

Take Measurements

13) Close V4.

14) Open V2.

15) Watch P2 closely.

16) Start stopclock when P2 = 1 bar (can be any pressure but make sure to note it).

17) Let pressure P2 rise by a given amount.

18) Note change in pressure P2 over measured time – this is the (dp_2/dt) term.

19) Close V1.

20) Open V4.

21) To take new measurements repeat from Stage 13.

Shut Down

22) Turn off vacuum pump.

23) Close N_2 supply at cylinder.

24) Open pressure release valve carefully to exhaust.

25) Open all other valves and wait until the system has return to atmospheric conditions.

26) Unscrew lid to remove sample.

27) Turn off pressure gauges (press select, select, enter).

28) Measure length and cross-sectional area of the sample.

Appendix II - Operating procedures for the integrated gas permeability and diffusivity apparatus – gas permeability

Start Up

1) The pressure gauge P2 should be chosen to suit the estimated sample permeability. If the permeability is predicted to be high (above 500 mD, use the Keller Pressure gauge, if lower, use the Pirani vacuum gauge.
2) Ensure cell is set up as illustrated in Figure A-1.

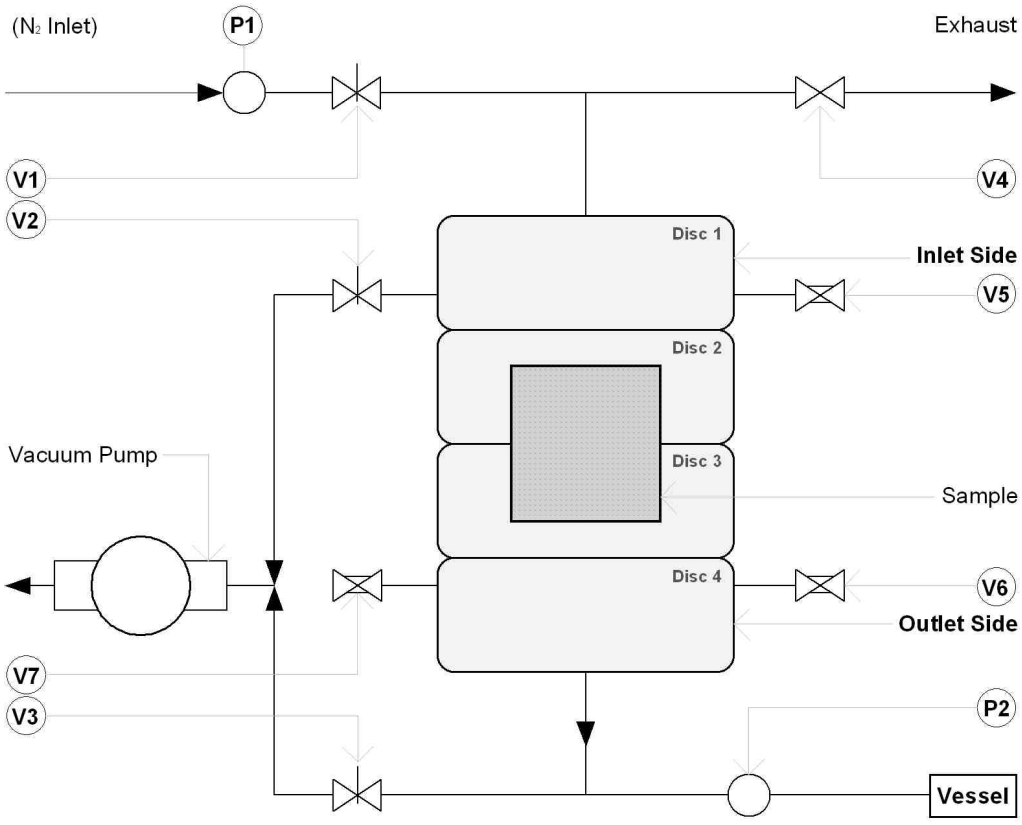


Figure A-1: Gas permeability cell set-up

Loading the cell

3) Remove the four disc-securing bolts.

4) Lift disc 1 and disc 2 from disc 3.

5) Place coated sample on top of O'ring in disc 3.

6) Replace discs 2 and 1.

7) Replace 4 bolts.

8) Ensures bolts are secured tightly at either end.

Cell evacuation (from all valves closed)

9) Switch on vacuum pump.

10) Open valves V2 and V3.

11) Monitor cell pressure using Pirani gauge (or Keller pressure gauge).

12) Adjust N_2 feed at N_2 regulator; start with a low pressure feed (0.3 bar recommended).

13) When cell pressure reaches ~ 10 Pa, measurements can commence.

14) Close V2.

15) Open V1 to admit N_2 from the N_2 cylinder feed at pressure P1.

16) Allow system to equilibrate, pressure at P2 should remain constant.

17) Close V3.

18) Note pressure at P2.

19) With stopwatch, measure the time taken for the pressure at P2 to rise by a given interval.

Resetting the cell

20) When measurement has been completed, close V1.

21) Open V2 and V3 to evacuate cell again.

22) Adjust N2 feed pressure at the N_2 cylinder regulator to a higher pressure.

23) Repeat 12 – 20 until a wide range of applied pressures have been used.

Low pressure measurements

For low pressure measurements only, repeat steps 13 – 19.

24) Ensure V2 remains open to a chosen degree to allow feed and bleed balance.

Shut Down

25) Turn off N_2 feed at the cylinder.

26) Open V1.

27) Switch off vacuum pump.

28) Open V4.

29) Measure (dp_2/dt) at p_1

30) Calculate $p_m = p_1/2$.

31) Plot each value of (dp_2/dt) at p_m.

32) Add a line of best fit.

33) Take the gradient of the curve.

34) Viscous permeability coefficient k = gradient × nitrogen viscosity.

35) Take the intercept of the curve.

36) Slip flow coefficient K_0 = intercept/v.

Appendix III - Operating procedures for the integrated gas permeability and diffusivity apparatus - gas diffusivity

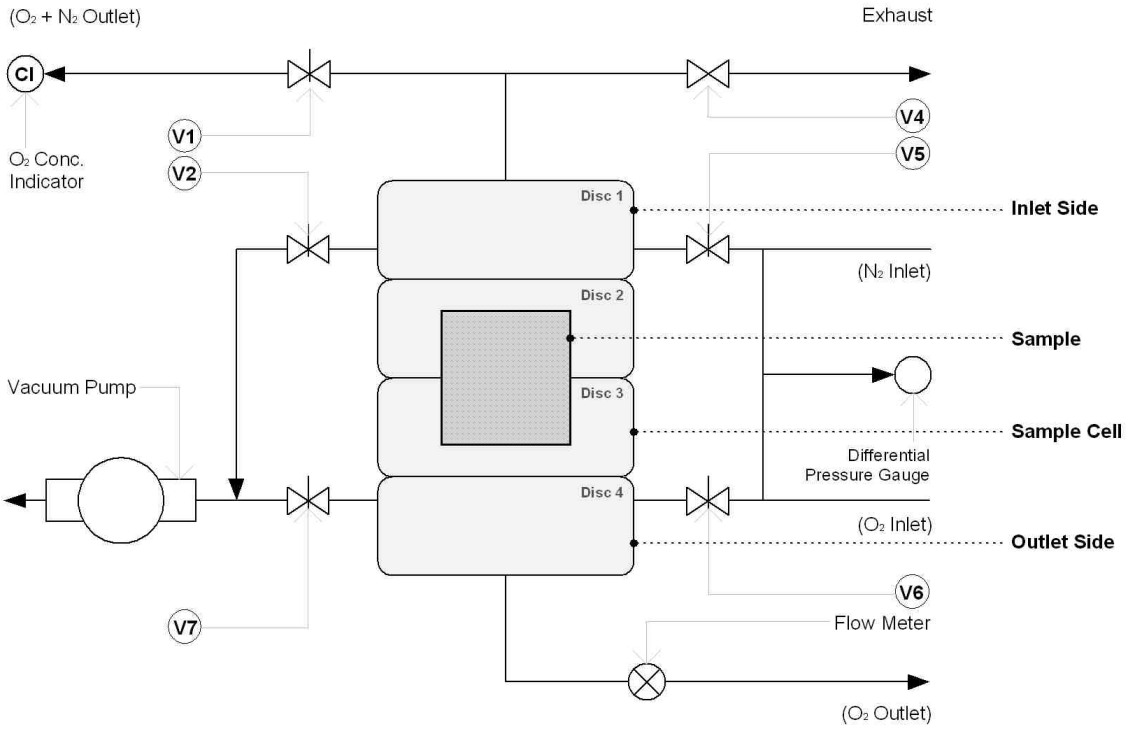


Figure A-2: Diffusivity cell set-up

Adjusting the cell from permeability to diffusivity (see Figure A-2 for illustration).

1) Connect O_2 analyser to O_2 and N_2 outlet.
2) Remove vessel and attach flow meter and O_2 outlet pipe.
3) Switch location of pump outlet and N_2 inlet.
4) Attach differential pressure gauge.

Start Up

All valves closed.

Set O_2 and N_2 pressures

5) Adjust N_2 feed at N_2 regulator to pressure p_1 and monitor on differential pressure gauge.
6) Adjust O_2 feed at O_2 regulator to pressure = p_1 (if operating zero pressure differential experiment).
7) Ensure dp = 0 on differential pressure gauge.

Evacuation

8) Open V2 and V7.
9) Turn on vacuum pump.
10) Read pressure on Pirani Gauge, when sufficiently low, turn off pump.
11) CloseV2 and V7.

Admit Nitrogen

12) Open V1.
13) Open V5.
14) Allow N_2 to penetrate the sample pores, wait for O_2 concentration in O_2 + N_2 stream < 10 ppm.

Admit Oxygen

15) When measured O_2 concentration has reached equilibrium open V6.

16) Turn on MaddClient analyser to measure O_2 concentration (set Output = ?).

17) Ensure N_2 and O_2 flowrates are equal to each other.

18) Start MaddClient analyser.

19) O_2 diffuses through the sample to the $N_2 + O_2$ outlet side.

Taking measurements

20) After x amount of time, O_2 concentration will reach an equilibrium value.

21) Concentration and time is measured using MaddClient software.

Shut Down

22) Turn off N_2 and O_2 supplies.

23) Open V2, V3 and V7.

Analysis

Steady State Diffusion

24) Open notebook file containing data collected with MaddClient software.

25) Plot concentration against time, shown in Figure A-3 below.

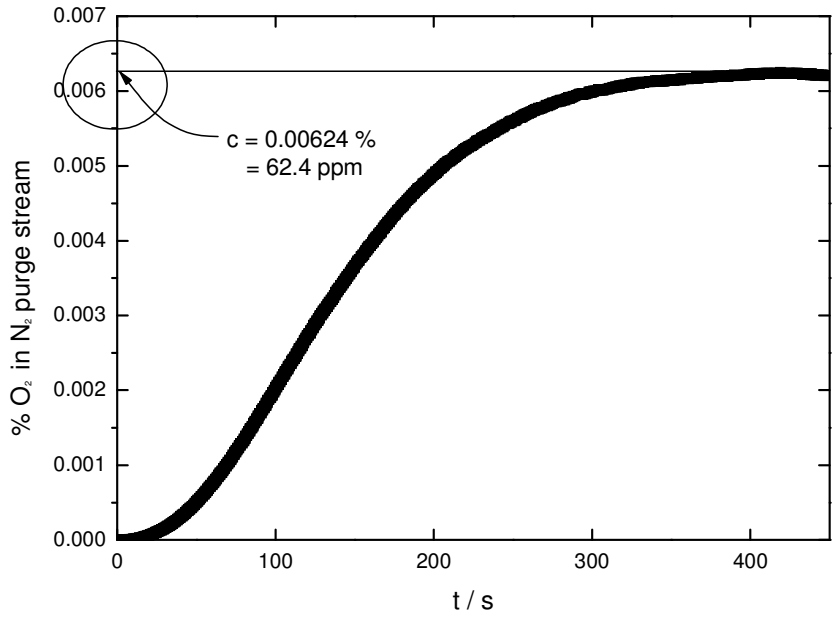


Figure A-3: Plot of oxygen concentration variation with time

26) Use Equation 2.22 to calculate the effective diffusion coefficient.

Transient Diffusion

27) Plot the O_2 concentration as a fraction of the equilibrium value reached against time, shown in Figure A-2.

28) Fit the data to theoretical data at t = t.

29) Find the corresponding value of $\left(\frac{D_{AB}t}{L_{eff}^{\ 2}}\right)$ from interpolation of values in Table A-1.

30) Equation A.3 can be solved for τ since L_{eff} is derived from X, see Appendix IV for more detail.

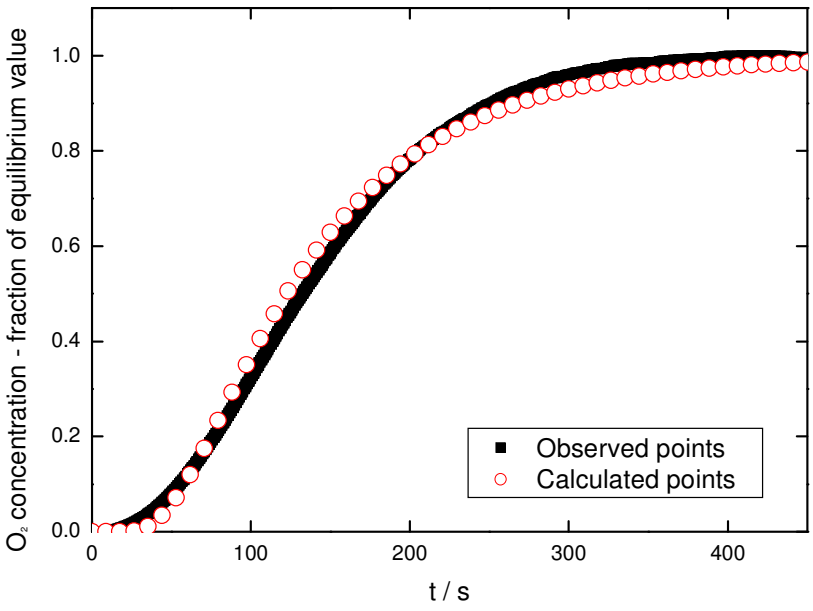


Figure A-4: Plot of theoretical data fitted to experimental transient diffusion data

Appendix IV – Calculation of transient diffusion

The rate of oxygen efflux through the pores may be expressed as *F*, a fraction of its value at infinite time and can be defined as shown in Equation A.1;

$$F = -1 + 2\sum_{n=1}^{\infty} \cos n\pi \exp\left(\frac{-D_{AB} n^2 \pi^2 t}{L_{eff}^{\ 2}}\right) \qquad \text{A.1}$$

where D_{AB} is the diffusion coefficient of gas A in gas B in free space n is the index t is the time and L_{eff} is the effective pore length. Theoretical values of F as a function of the dimensionless group $\left(\frac{D_{AB}t}{L_{eff}^{\ 2}}\right)$ can be obtained by iteratively solving Equation A.1 and are presented in the matrix of Table A-1 (values of $\left(\frac{D_{AB}t}{L_{eff}^{\ 2}}\right)$ are given in bold where for example, F = 0.35053 when $\left(\frac{D_{AB}t}{L_{eff}^{\ 2}}\right)$ = 0.11). Experimental data of the ratio of actual to final efflux rate against time is fitted to the theoretical data by the solution of $\left(\frac{D_{AB}t}{L_{eff}^{\ 2}}\right)$ at various values of *t.* The corresponding value of F is then used to determine the effective pore length using Equation A.2 and the tortuosity is directly found from the ratio Equation A.3:

$$\frac{D_{AB}}{L_{eff}^{\ 2}} = \frac{F}{t} = X \qquad \text{A.2}$$

$$\tau = \frac{L_{eff}}{L} \qquad \text{A.3}$$

Table A-1: Theoretically calculated values of F (in the matrix of the table) as a function of $\left(\frac{D_{AB}t}{L_{eff}^{\ 2}}\right)$ (in bold).

$\left(\frac{D_{AB}t}{L_{eff}^{\ 2}}\right)$	**0.00**	**0.01**	**0.02**	**0.03**	**0.04**	**0.05**	**0.06**	**0.07**	**0.08**	**0.09**	**0.10**
0.0	0.00000	0.00000	0.00003	0.00157	0.01089	0.03400	0.07142	0.11991	0.17528	0.23386	0.29290
0.1	0.29290	0.35053	0.40559	0.45741	0.50567	0.55028	0.59131	0.62888	0.66319	0.69446	0.72292
0.2	0.72292	0.74879	0.77228	0.79361	0.81295	0.83049	0.84640	0.86082	0.87389	0.88573	0.89647
0.3	0.89647	0.90619	0.91501	0.92299	0.93023	0.93023	0.93679	0.94811	0.95299	0.95740	0.96141
0.4	0.96141	0.96503	0.96832	0.97130	0.97400	0.97644	0.98066	0.98066	0.98248	0.98412	0.98562
0.5	0.98562	0.98697	0.98819	0.98930	0.99031	0.99122	0.99204	0.99279	0.99347	0.99408	0.99464
0.6	0.99464	0.99514	0.99560	0.99601	0.99639	0.99673	0.99703	0.99731	0.99757	0.99779	0.99800
0.7	0.99800	0.99819	0.99836	0.99851	0.99865	0.99878	0.99889	0.99900	0.99909	0.99918	0.99926
0.8	0.99926	0.99933	0.99939	0.99934	0.99950	0.99955	0.99959	0.99963	0.99966	0.99969	0.99972
0.9	0.99972	0.99965	0.99972	0.99965	0.99977	0.99979	0.99981	0.99983	0.99985	0.99986	0.99990
1.0	0.99990	0.99991	0.99992	0.99992	0.99993	0.99994	0.99995	0.99995	0.99995	0.99996	0.99996
1.1	0.99996	0.99997	0.99997	0.99997	0.99997	0.99998	0.99998	0.99998	0.99998	0.99998	0.99999
1.2	0.99999	0.99999	0.99999	0.99999	0.99999	0.99999	0.99999	0.99999	0.99999	0.99999	0.99999
1.3	1.00000	1.00000	1.00000	1.00000	1.00000	1.00000	1.00000	1.00000	1.00000	1.00000	1.00000

Appendix V - Operating procedure for the integrated mercury apparatus

The labels in this section refer to the image in Chapter 4.

Apparatus set up

1) Check stainless steel fittings are connected and cold trap is installed.
2) Check all connections are tight and valves are in closed position.
3) Fill cold trap with liquid N_2.
4) Turn on Pirani gauge and check pressure p = 100 Pa.
5) Turn on vacuum pump, ensuring pump exhaust is inside fume cupboard.
6) Open N_2 supply.

Evacuate

7) Open V1, V2, V3, V4.
8) Turn V10, V11 to vacuum side and open V14, V15, V16, and V17.
9) Monitor pressure using Pirani gauge at V and allow it to fall to 10^{-2} mbar.

Saturate sample

10) Turn V10 and V11 to Off position.

11) Open V8.

12) Hg should flood the system.

13) The cell is now ready for Hg porosimetry readings.

Hg Porosimetry Measurements

14) Open V14 and fill manometer tube 1 with Hg.

15) Close V14.

16) Turn V10 to N_2 position and allow system to stabilise.

17) Open V12.

18) Measure the change in height of Hg in manometer tube 1.

19) Be sure to note ΔH (cmHg) at the given pressure.

20) Turn V10 to closed position.

21) Increase flow of N_2 to and note pressure P3 and P2.

22) Turn V10 to N_2 position and repeat from 28 – 32, increasing P3 in small increments until sample is completely saturated.

23) Close V12, turn V10 to off position and reduce P3 back to 0.5 bar.

24) Sample is now ready for Hg permeability readings.

Hg Permeability Measurements

25) Turn V11 to vacuum position.

26) Carefully open V13 and allow Hg from the sample cell into manometer tube 2.

27) Close V13.

28) Slowly open V15 to allow Hg from sump into manometer tube 2 to a suitable height.

29) Close V15.

30) Open V8 and V9.

31) Turn V11 to N2 position.

32) Open V12 and V13.

33) Hg level in tube 2 should fall and in tube 1 should increase.

34) Turn V10 to N_2 position and allow system to stabilise.

35) Close V8 and V9.

Measurement 1

36) Increase flow of N_2 to P3 = 10^5 Pa.

37) Note heights in tubes 1 and 2.

38) Open V8.

39) Measure time taken for Hg height in tube 1 to fall to a given level.

40) Close V8 and note heights in tubes 1 and 2 at time t.

41) Note that when V8 is closed, heights will still vary.

Exhaust

42) Open V8 and V9.

43) Close V5 and open V6 to exhaust N_2.

44) Close V8 and V9.

45) Close V6 and open V5.

Other measurements;

46) Increase flow of N_2 to P3 = 1.5×10^5 Pa or by a suitable increment for the sample.

47) Repeat from step 36 to 45 for each measurement.

48) Ensure that readings are taken three times for each pressure.

Shut Down

49) Close V12 and open V14.

50) Open V8.

51) Hg should fall from tube 1 into Hg sump.

52) Close V14.

53) Turn V11to off position.

54) Close V5 and open V6 to reduce pressure in tube 1 to atmospheric.

55) Close V6 and open V5.

56) Open V15 and allow Hg in tube 2 to fall into sump.

57) Close V15.

58) Open V14, V13 then V12.

59) Hg from sample cell should be forced the sample from right to left into the sump.

60) Close V18.

61) Turn off N_2 supply.

62) Open V6 to exhaust system.

63) Turn off vacuum pump.

64) OpenV1, V2, V3 and V4.

Appendix VI – Graphical representations of turbulent results

Plots of *C* vs. *V(dp₂/dt)* are presented in this Section for Sample S1 – S8 (Figures A-5 – A-12).

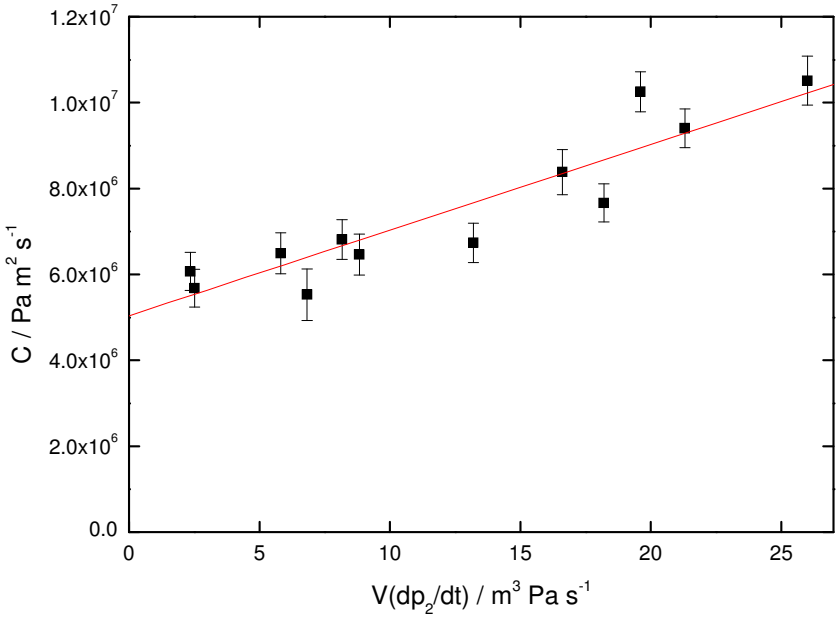


Figure A-5: *C* vs. *V(dp₂/dt)* obtained by analysis of turbulence for sandstone Sample S1

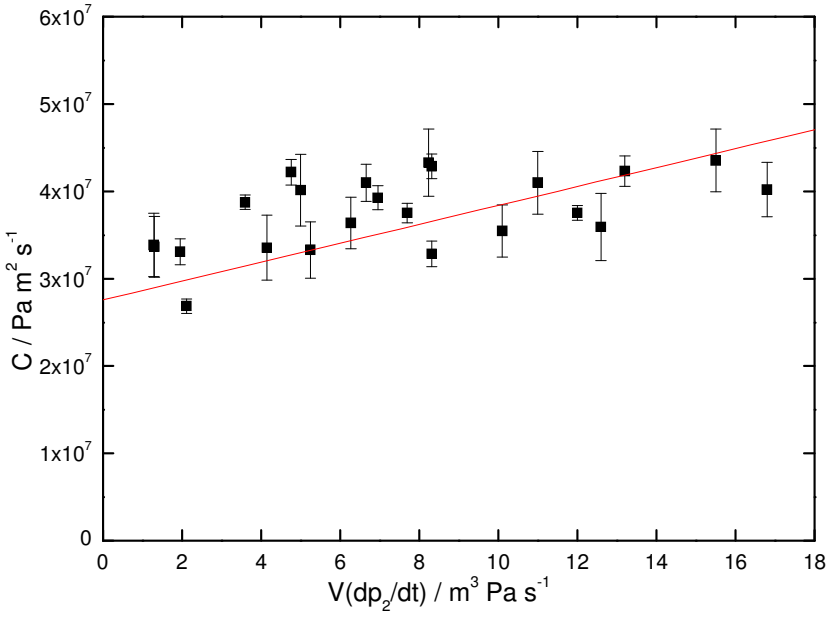


Figure A-6: *C* vs. *V(dp$_2$/dt)* obtained by analysis of turbulence for sandstone Sample S2

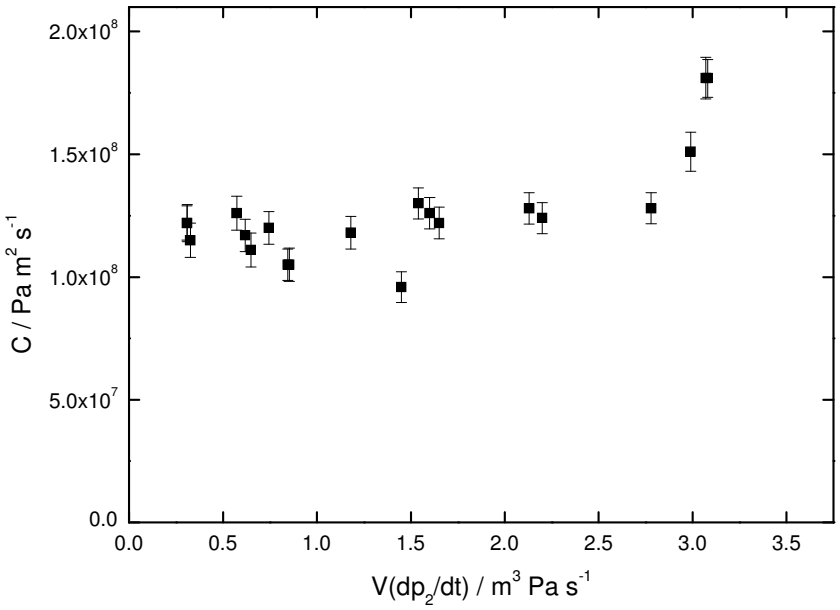


Figure A-7: *C* vs. *V(dp$_2$/dt)* obtained by analysis of turbulence for sandstone Sample S3

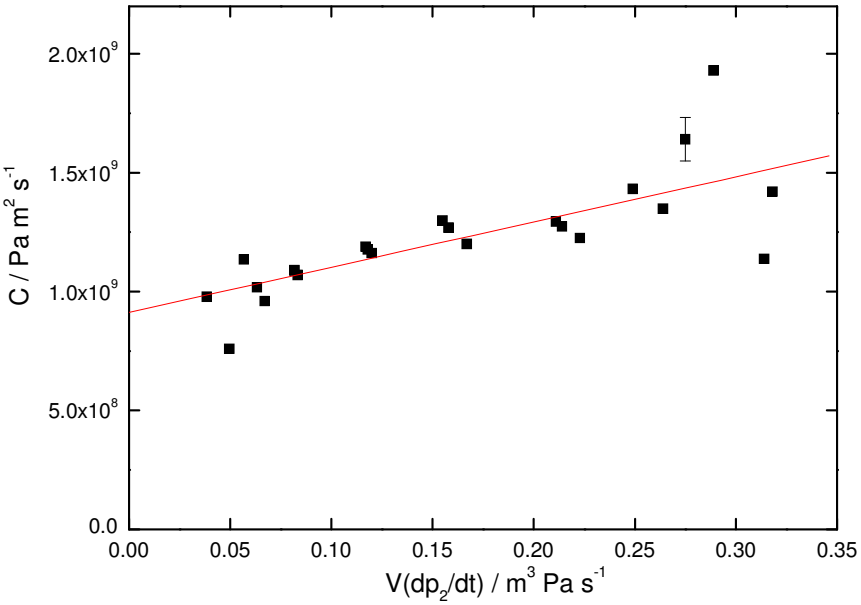


Figure A-8: *C* vs. *V(dp$_2$/dt)* obtained by analysis of turbulence for sandstone Sample S4

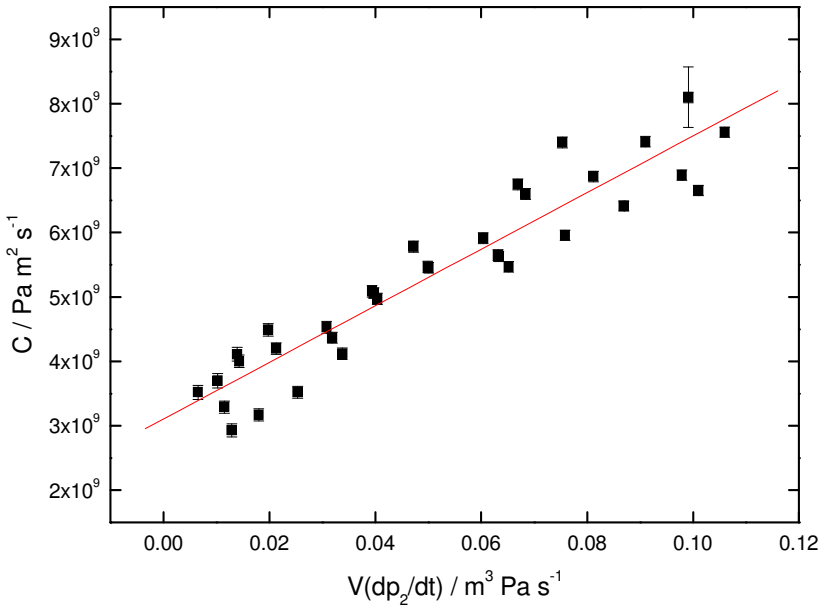


Figure A-9: *C* vs. *V(dp$_2$/dt)* obtained by analysis of turbulence for sandstone Sample S5

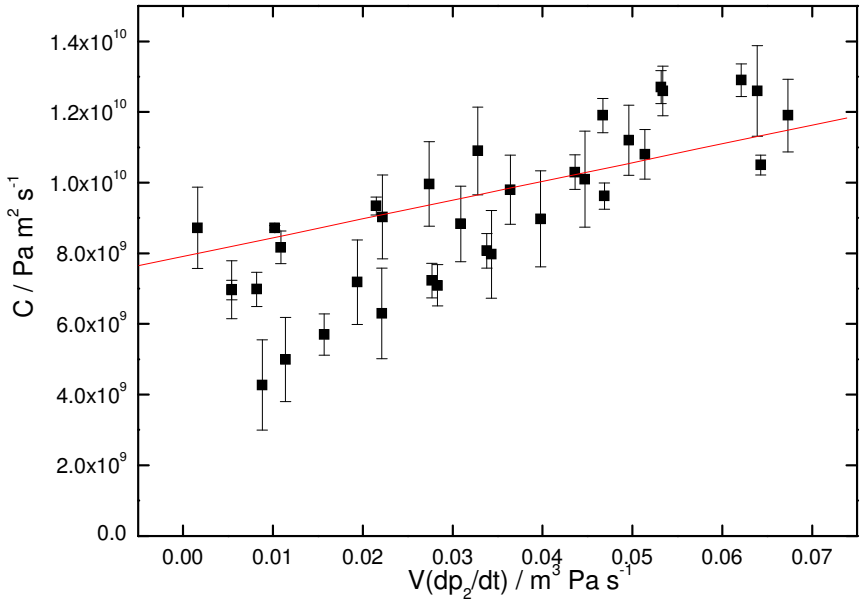


Figure A-10: *C* vs. *V(dp$_2$/dt)* obtained by analysis of turbulence for sandstone Sample S6

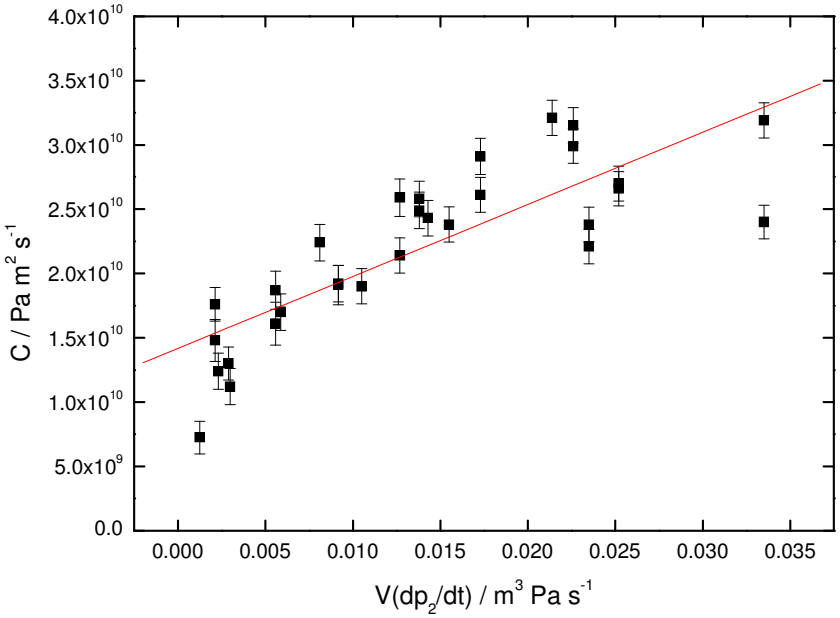


Figure A-11: *C* vs. *V(dp$_2$/dt)* obtained by analysis of turbulence for sandstone Sample S7

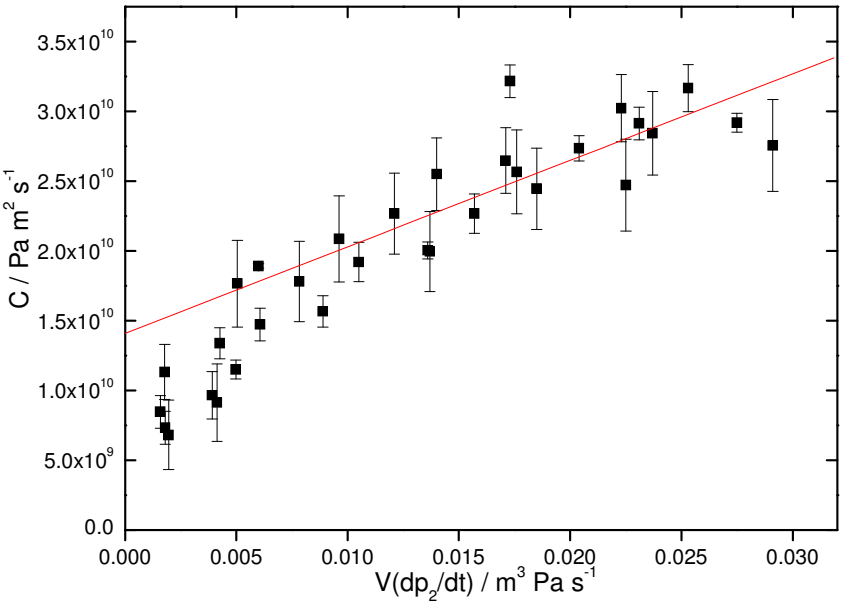


Figure A-12: *C* vs. *V(dp$_2$/dt)* obtained by analysis of turbulence for sandstone Sample S8

Appendix VII – Thin-section Images

Representative images of thin-sections of sandstone Samples S1 – S7 are presented in this *Section* from Figure A-11 – A-16.

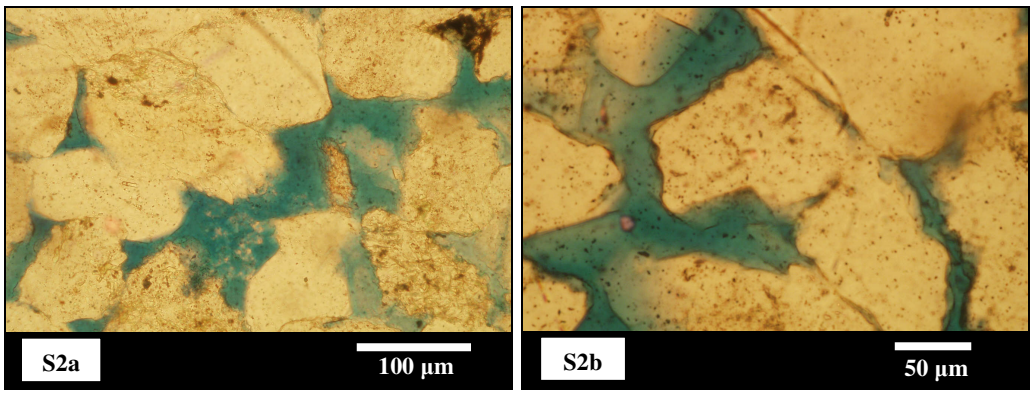


Figure A-13a and b: Microscope images of sandstone Sample S2

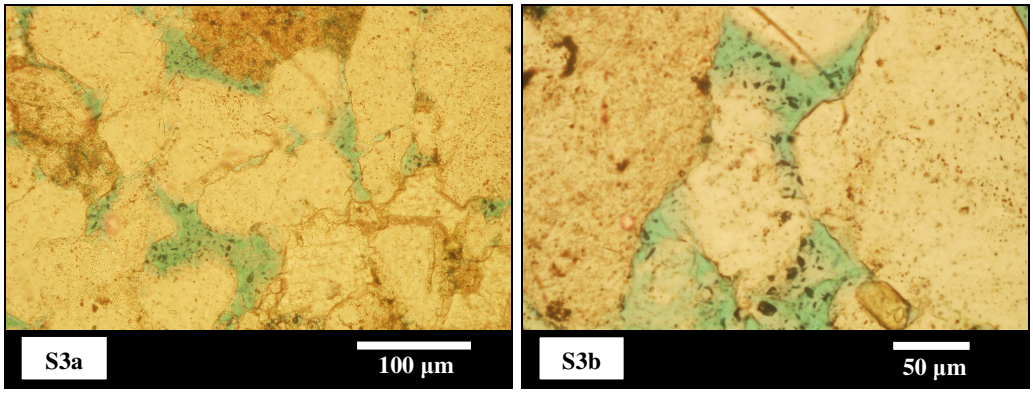


Figure A-14a and b: Microscope images of sandstone Sample S3

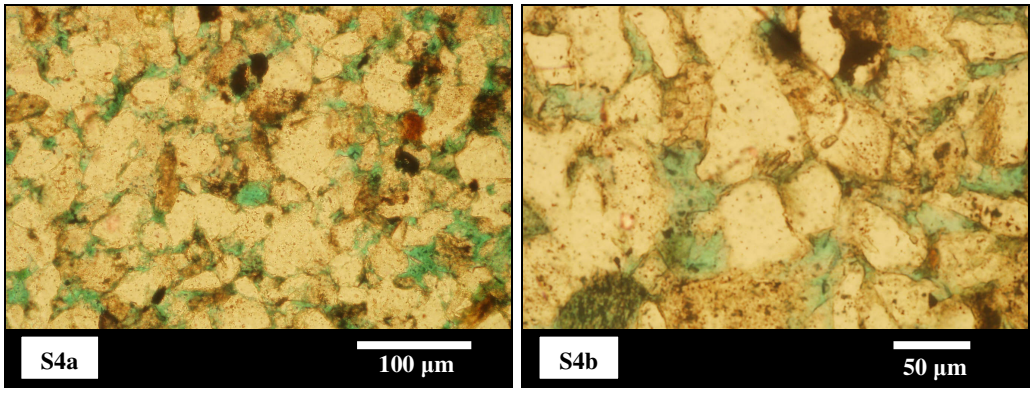


Figure A-15a and b: Microscope images of sandstone Sample S4

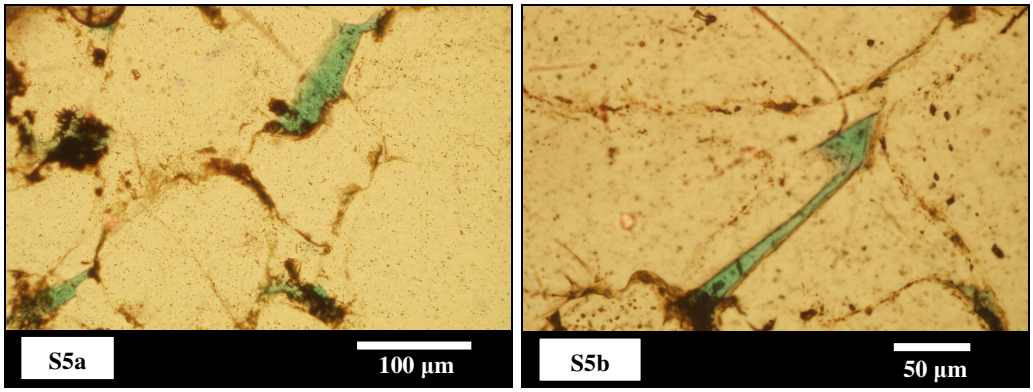


Figure A-16a and b: Microscope images of sandstone Sample S5

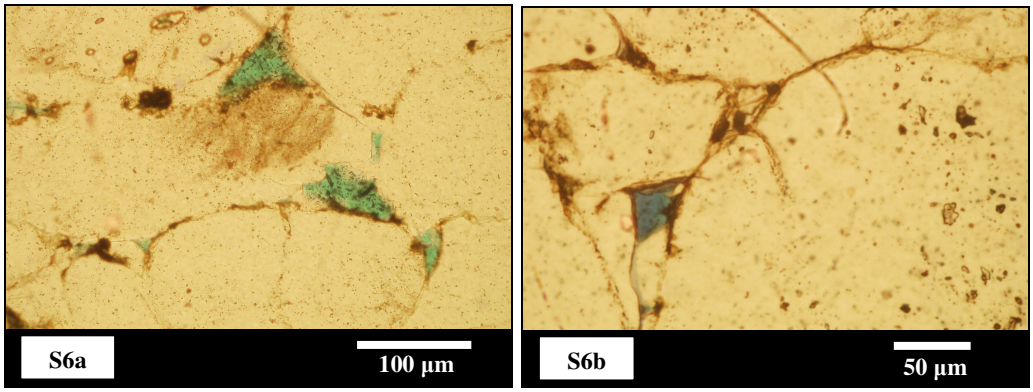


Figure A-17a and b: Microscope images of sandstone Sample S6

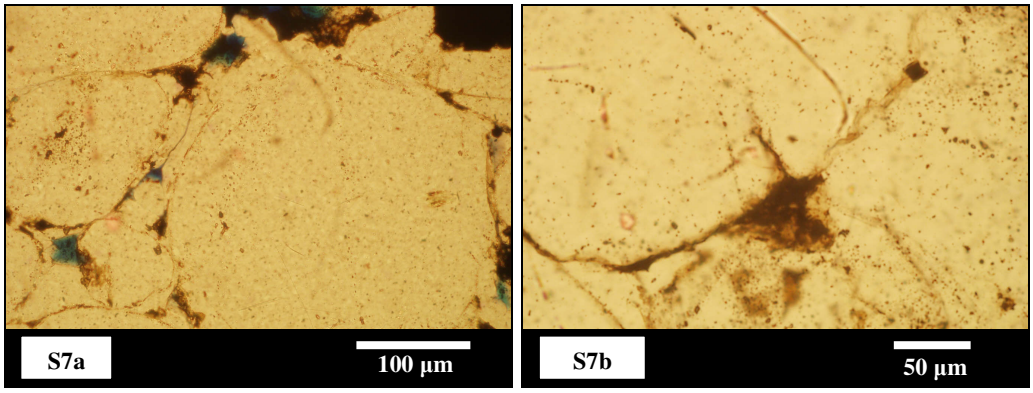


Figure A-18a a and b: - Microscope images of sandstone Sample S7